공학박사 학위논문

# Studies on oxide inclusion control for steel cleanliness in ladle furnace and continuous casting mold

청정강 생산을 위한 래들과 몰드에서의
비금속 개재물 제어에 관한 연구

**2020년 8월**

서울대학교 대학원

재료공학부

이 원 혁

# Abstract

Refining in the ladle is the last step to control endogenous inclusion in the steel production stage, so it is very important to simulate the inclusion produced during the deoxidation process. In particular, calcium is additionally added for ease of flotation, and there are many allotropes and the number of reactions involved is very large, making it very complex to understand its reaction mechnism. To simulate this, the three phase flow consisting of the molten steel – Ar gas – slag at the front end should be preceded, and the implementation of the alumina inclusion generation by primary deoxidation reaction should be implemented.

To simulate the three phase flow consisting of molten steel – Ar gas – slag, the quasi single phase model and drift flux model were used to reflect the interaction force between gas and melt. A model for slag deformation was developed and combined with the fluid flow module. The experiment was conducted through a water model, which is 1/8 of the actual ladle size, and the reliability of the model was verified by comparing the area of the plume eye formed at the top of the ladle. We developed a chemical reaction model that can solve the species transport according to the introduction of deoxidizers such as Al and Ca and simulate primary deoxidation and secondary deoxidation using the flow result calculated in the previous stage. Through calculations that combine thermodynamic theory and kinetic theory, chemical reaction results can be traced at every position inside the ladle at every time step and the process to reach equilibrium is predicted. When the amount of Ca was low and the solid calcium aluminate phases became the equilibrium phase, it was confirmed that the equilibrium was not reached during the conventional operation time because it took a very long time to reach the equilibrium.

Flow analysis in mold is important because unstable flow could trap slag and mold flux and it lead to exogenous inclusion. Fluid flow patterns within a conventional slab continuous-casting mold are closely linked to the port angle of the submerged entry nozzle (SEN). Fluid flow is unstable below a certain port angle, with large fluctuations near the port outlet as well as jet stream oscillation and repeated vortex formation and dissipation within the mold. However, such phenomena are not observed above a certain port angle, at which the flow pattern becomes stable. This behavior was investigated via both numerical simulation and water model experimentation; two different regions were identified with flow patterns varying according to the SEN port angle. In addition, a close quantitative relationship was identified between changes in the port angle and fluid velocity variations. For SEN port angles in the range 0–15°, the flow velocity in the upper circulation zone oscillated in an unstable manner. For port angles of 20° or more, the flow velocity of the same zone decreased significantly and stabilized. When the gas was injected, the unstable region elongated to 0–20°.

The present study offers insight toward developing a clearer understanding of the complex chemical reaction in the ladle furnace and flow patterns in casting molds which is deeply related to inclusion.

**Keyword :** Ladle furnace, Continuous casting mold, thermodynamics, kinetics, inclusion, flow pattern, computational fluid dynamics

**Student Number :** 2014-21456

# List of Figures

# List of Tables

# Contents

# Chapter 1. Introduction

## 1.1 Inclusion

Inclusions are chemical compounds and nonmetals that are present in steel and other alloys. It is called NMI (non metallic inclusion) because oxygen, sulfur, silicon, and nitrogen dissolved inside the molten steel react with metal to form oxide, sulfide, silicate, and nitride compounds during steel production. Among them, it is known that oxide inclusion accounts for the largest portion.

NMI can also be classified into Exogenous and Endogenous depending on the cause of formation. Exogenous NMI refers to non metallic inclusion formed due to the external containment of slag droplet entrapment, refractory material, and mold flux. Endogenous NMI stands for inclusion generated by a chemical reaction during the steelmaking process. In addition to chemical reactions in the refining process, precipitation occurs during freezing. The non-metallic particles thus formed are embedded in the matirx of final steels product. Table 1-1 shows the possible inclusion sources in the steel production process [1].

During the deoxidation process in the ladle, the rate of nucleation is determined according to the supersaturated concentration of alloy. The time for nucleations is generally on the order of 0.1 second or less [2, 3]. As shown in Fig. 1-1, the primary nucleated particles have a spherical shape, but their morphology varies depending on the oxygen concentration and process time [4].

On the other hand, in a continuous casting mold, temperature reduction due to freezing makes the reaction equilibria favor in the direction in which the oxidation reaction is promoted. In addition, since the solubilites for the solutes of solid steel and alloys are lower than in the liquid state, as the solidification

progresses, the solute is continuously ejected into the liquid phase of the solidification tip, resulting in the segregation of the solute [5] (Fig. 1-2). Accordingly, subsequent reaction of inclusion formation and growth occur during solidification.

**Table 1-1.** Possible inclusion source [1].

| | Source | Key elements |
|---|---|---|
| Furnace | Furnace slags | Ca |
| | Furnace refractories | Ca |
| | Ferroalloys | Cr, Al, Si |
| Tapping | Launder refractories | Mg, Ti, K |
| | Oxidation | FeO |
| Ladle | Deoxidation | |
| | Ladle slag | Ca, Mg |
| | Ladle refractories | Mg, Ti, K |
| Teeming | Stopper and nozzle refractories | Mg, Ti, K |
| | Oxidation | FeO |
| | Deoxidation | |
| Ingot mold | Refractories | Mg, Ti, K |
| | Deoxidation | |
| Heat treatment and rolling | Surface oxidation | FeO |
| | Surface sulfurization | FeS |
| | Inner oxidation | $SiO_2$ |
| | Hot shortness | FeS |
| Welding | Welding slags | Ca, Ti |
| | Electrode coatings | Ti, V |
| | Steel inclusions | |
| | Hot tearing | S |

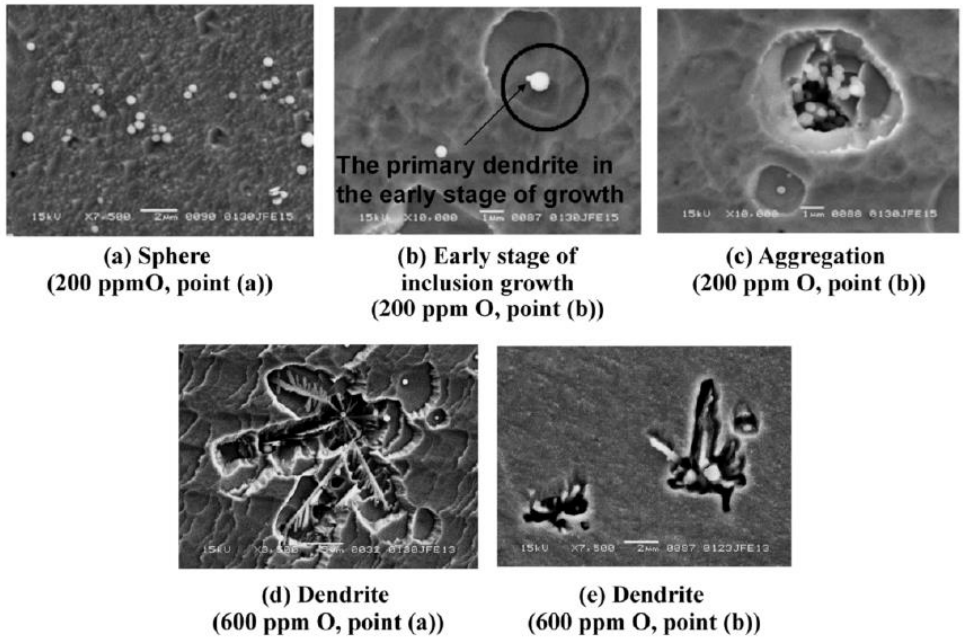


**Fig. 1-1.** Alumina inclusion morphologies at different starting oxygen levels in aluminum deoxidation [4].

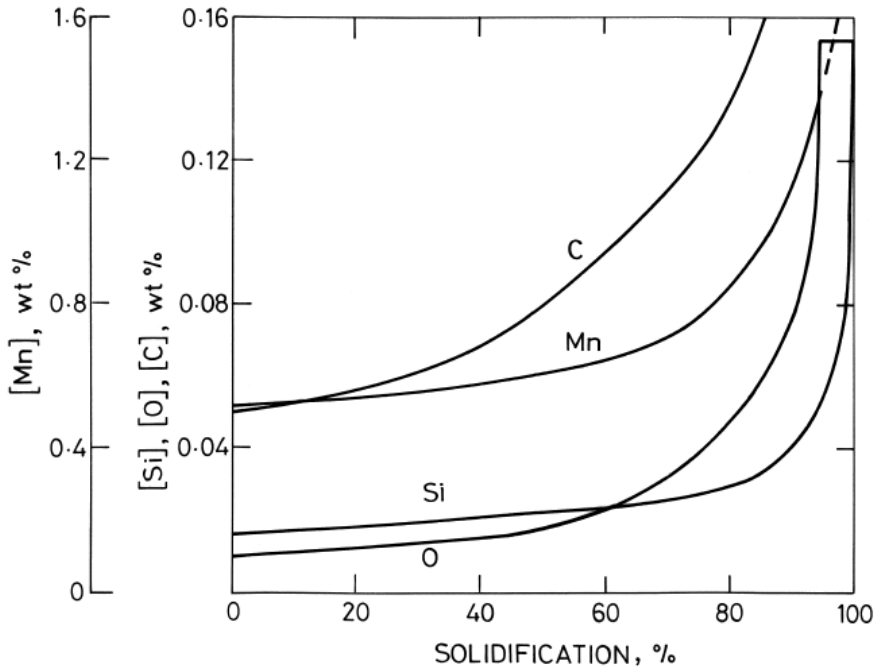


**Fig. 1-2.** Solute segregation in solidifying shell [5].

## 1.2 Quality problem related to inclusion

### 1.2.1 Nozzle clogging in submerged entry nozzle of casting mold

The refined molten steel is injected into the casting mold through a submerged entry nozzle (SEN), and slabs are continuously produced. At this time, a non-metallic inclusion such as Al2O3, which has not been removed in the refining process, is adsorbed to the SEN when introduced with molten steel, causing nozzle clogging. As a result, geometrical differences between the two nozzle outlets occur and the asymmetric flow becomes more severe. The quality of both sides of the steel produced by the asymmetric flow is not only non-uniform, but also the mixing of slag or mold flux at the upper part of the mold causes detrimental effects on the cleanliness of the steel. The vortex is formed at the interface between slag-molten steel by unstable flow as shown in Fig. 1-3, which is a major route for the creation of exogenous inclusion.

In addition, asymmetric flow causes imbalance of superheat at the upper part of the mold, which is the point where initial solidification occurs, so it can lead to non-uniform shell formation and lead to breakage when iron pressure cannot be sustained, and can be a starting point for surface crack.

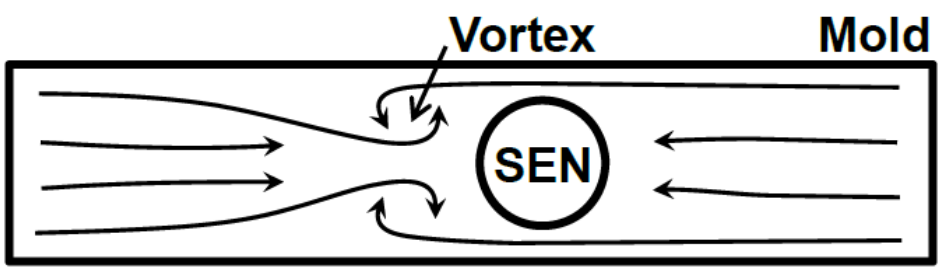


**Fig. 1-3.** Mechanism of vortex formation in the mold [6].

### 1.2.2 Failure on processing – hot and cold working and forming

When NMI is excessively present in products such as slabs or blooms made by continuous casting or when large size of non-metallic inclusions are present, fracture occurs during deformation process such as rolling to produce a plate, extruding to produce a rod, or drawing (Fig. 1-4). Furthermore, because NMI could act as a stress concentrator, it is very detrimental in deformation processing.

Generally, cleanliness assessment refers to determination of size, size distribution, number, and volume fraction of inclusion in steel. The traditional method for inspection is based on sampling. Sampled specimen is analyzed using electron probe microanalyzer (EPMA), scanning electron microscope (SEM), enegy dispersive x-ray analysis (EDX) attachment for an SEM. The traditional sampling method is available, however, it is laborious and unreliable. Because the inclusion size distribution is different in spatial way, sample cannot represent the total steel quality. Ultrasonic inspection is more practical and reliable for inspecting NMIs. In some cases, 100% immersion ultrasonic inspection must be performed to eliminate sections of bar stock where these NMIs concentrate. As severity of forging increases and steels become stronger and less ductile, the detection limits of ultrasonic examination are approached or surpassed.

(a)

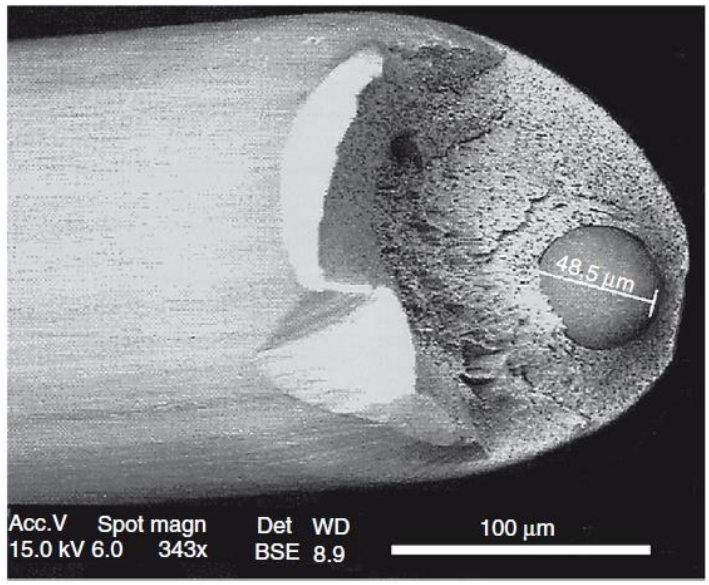


(b)

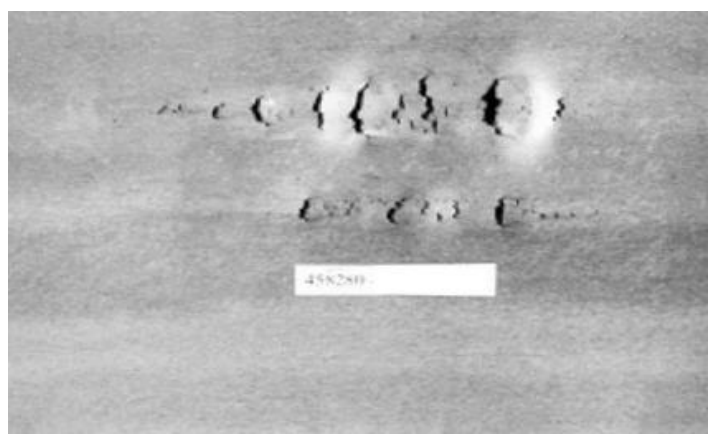

**Fig. 1-4.** Failures of deformation processing. (a) Fracture dyring cold drawing of steel wire [7]. (b) Thickness rupture of cold rolled steel foil by alumina clusters [8].

### 1.2.3 Reduction of mechanical properties of the steel

The NMI generated inside the steel induces nucleation of voids, and the growth and coalescence of voids leads to ductile fracture.The primary voids grow until a certain strain when they coalesce. The finer voids soften the ligaments and promote strain localization and the linkng of the primary void [9].

Large void worsens fatigue properties. The fatigue limit is correlated with the existence of non-propagating cracks. The fatigue limit is a threshold stress for crack propagation and it is determined by a material property related to average resistance to plastic deformation. Empirical relation was propsed by Mrakami et al. between the endurance limit and harness considering area of inclusion [10].

$$\sigma_w = 1.43\ (H_v + 120) / (\sqrt{area_s})^{1/6} \quad (1\text{-}1)$$

where $\sigma_w$ is the fatigue limit (MPa), $H_v$ is the Vickers hardness (HV) and $area_s$($\mu m^2$) is the area occupied by the inclusion. Therefore, fatigue properties of steel is deteriorated as the inclusion is present in excess amount.

## 1.3 Refining in steelmaking process

The purpose of the refining process is to remove impurities, remove or dilute excess components, and add and adjust necessary components to finally make defect-free ingots or fragments from steel materials. At the same time, no harmful substances should be incorporated during this refining. The main targets for removal are excess elements C and harmful elements P and S. Increasing the amount of O in molten iron can remove them, but at the same time, O can oxidize other components, such as Si or Mn.

For this reason, knowing the equilibrium relationship between the solute element in molten iron and O is important for understanding the steelmaking reaction and determining the conditions of the oxidative refining or the operation policy.

### 1.3.1 Primary refining in converter

In converter, oxygen gas is blown into a molten iron and the impurities are oxidized and removed (Fig. 1-5). Examples of gaseous oxygen include air, oxygen-enriched air, pure oxygen gas, and mixed gas of oxygen and other gases.

Oxidation proceeds directly with gaseous oxygen and the molten iron is stirred with this blown gas, so the refining reaction proceeds quickly and the productivity is extremely high. The temperature of molten iron rises due to the heat of oxidation generated, and refining proceeds smoothly without external heat replenishment, which is advantageous in terms of thermal energy. Moreover, the equipment is simple.

In the converter, oxygen is blown to reduce excess [C] and at the same

time, harmful impurities such as [P] are removed. At this time, [Si] or [Mn] in the molten iron is oxidized to ($SiO_2$) or (MnO). They are combined with (CaO) or (FeO) to be added as a preparation agent to form a basic solvent having good fluidity, and P2O5 oxidized by [P] is combined to be separated and removed from molten steel. The order of oxidation is determined by the affinity for oxygen. The affinity is in the relationship of Si> Mn> C> Fe. Therefore, [Si] and [Mn] are first oxidized (first phase), then oxidation of [C] is vigorous (second phase), and most of [C] are oxidized and removed, so Fe oxidation occur (3rd phase).

In the case of [P], direct oxidation by oxygen gas also occurs but since the presence of (CaO) in the solvent is required for active dephosphorization reaction. The dephosphorization reaction does not proceed while the oxidation of [Si] starts and becomes an acidic solvent, but CaO of the preparation dissolves and becomes a basic solvent, and when [O] increases and (FeO) increases, reaction becomes vigorous. Since the dephosphorization reaction is efficient at a low temperature, it is necessary to quickly create an optimum solvent in the early stage of refining where the temperature of molten iron does not rise. For this reason, in the case of molten iron with a high P content, soft blow may be performed at the beginning of blow. With soft blow, stirring is weakened and decarburization reaction is suppressed, but (FeO) is increased, and dephosphorization reaction proceeds effectively prior to decarburization reaction.

[S] in the molten iron reacts with (CaO) in the molten metal and moves to the molten metal as (CaS) and is removed. In order to advance the desulfurization reaction, (CaO) is increased and [O] is decreased, which simultaneously decreases (FeO). In order to increase (CaO), there is no method other than to increase the basicity, and desalination can hardly be desired under acidic solvents. The change

of [S] during the blow is carried out in the final stage of the blow.

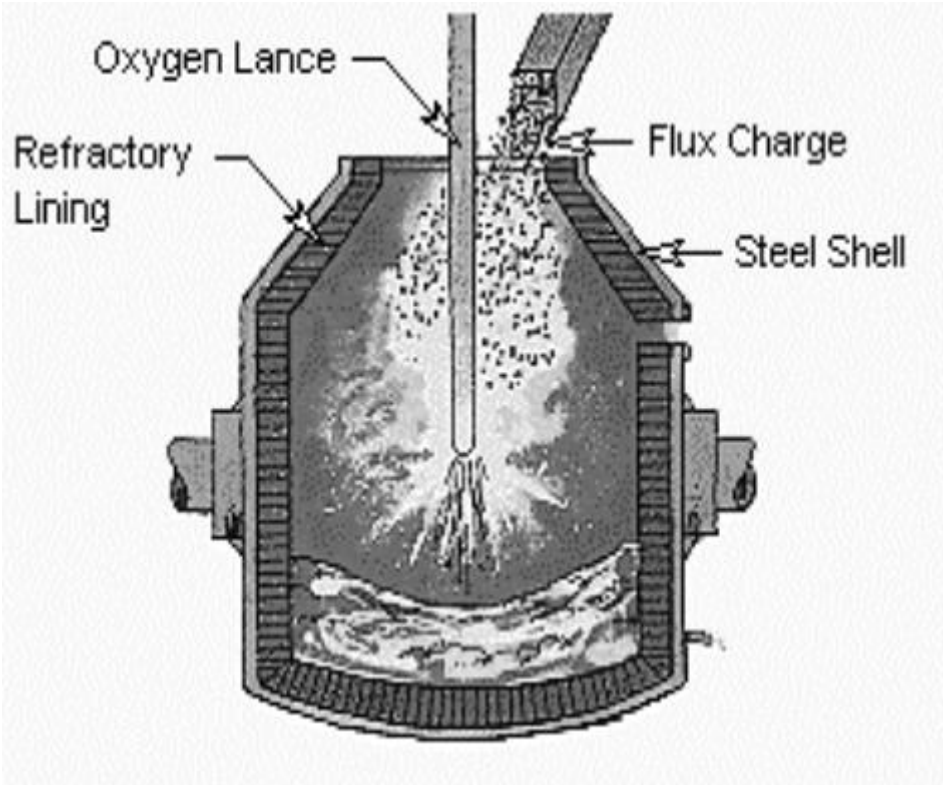


**Fig. 1-5.** Oxygen converter with blowing on the melt surface [11].

### 1.3.2 Secondary refining in ladle furnace

The following refining effect can be obtained by secondary refining in a vacuum or inert gas atmosphere of the ladle furnace (Fig.1-6).

(1) Purification by facilitating floating separation of inclusions suspended in molten steel

(2) Purification by removal of impurities in the refining effect of reduced pressure or dilution

(3) Uniformity of molten steel components

Due to quality improvement and stabilization, molten steel is refined by these means. The main subjects of the completion treatment are decarburization and deoxidation, and gas components such as hydrogen, which have not been sufficiently removed in the previous process. Additional desulfurization is also conducted. If bubbling of inert gas such as Ar is performed to molten steel inside the ladle furnace, the molten steel is stirred, and inclusions suspended in the molten steel are aggregated and separated. Stirring also contributes to the homogenization of the alloy added when exiting, and it is also possible to adjust the temperature by equalizing the molten steel temperature or adding a coolant. The LF method is widely used as a finishing process for molten steel for continuous casting, which has a narrow temperature range for casting and is required to avoid bringing in non-metallic inclusions.

**Deoxidation reaction**

In the primary refining, decarburization and dephosphorization occur, and the content of [O] increases until the target [C] and [P] reach equilibrium. Other solutes Si, Mn, and Cr are also oxidized until equilibrium with [O].

When the molten steel having a high [O%] is solidified as it is, [O%] in equilibrium with the solute decreases as it cools, so an oxidation reaction occurs as much as the difference, resulting in an oxidation product. As the temperature decreases, the equilibrium oxygen concentration decreases and bubbles are generated as much as the difference in equilibrium oxygen concentration. The bubbles generated at this time remain inside the ingot. In addition, the excess dissolved oxygen makes it difficult to precisely match the target component of alloying element because of the oxidation of the alloying element. It is also disadvantageous from an economic point of view.

In order to cope with these problems, it is necessary to deoxidize the target component value of the steel to [O%] or less of the equilibrium value at the solidification temperature.

**Deoxidation by slag**

The relationship between [O] in molten steel and (FeO) in slag satisfies the following relationship, and the Gibbs energy change and equilibrium constant accompanying reaction are as follows.

$$(FeO) = Fe(l) + [O] \tag{1-2}$$

$$\triangle G^{\circ} = 27630 - 11.65T \tag{1-3}$$

$$K = \frac{a_O}{a_{(FeO)}} = \frac{f_O[O\%]}{\gamma_{(FeO)} N_{FeO}} \tag{1-4}$$

*F* is the fugacity of oxygen, [O%] is weight percent of oxygen, $\gamma$ is the activity coefficient, and $N$ is the mole number. Accordingly, an increase in activity of FeO must be suppressed in order to maintain a driving force for deoxidizing. The activity coefficient is dominated by the basicity of slag, etc. But since this basicity

has an appropriate value due to desulfurization, a low activity of FeO is most important.The equilibrium constant is lower as the temperature is lower, which is advantageous for deoxidation, but the low temperature has a limit because it deteriorates the fluidity of the slag. In order to promote diffusion deoxidation advantageously, it is advantageous to reduce N(FeO) and at the same time adjust viscosity to increase reactivity and increase the contact surface to stir.

**Forced chemical deoxidation**

Diffusion deoxidation by slag is an ideal deoxidation method that does not contaminate molten steel as a reaction product, but there is a limit to the amount of deoxidation, and diffusion deoxidation alone cannot reduce the desired [O] target concentration. In addition, it is difficult to maintain the reducing potential of slag in an oxidizing atmosphere, so there are many steelmaking methods in which diffusion deoxidation cannot be used. Therefore, by adding an element with an affinity for oxygen larger than Fe or ferro-alloy bearing the element, oxygen is directly taken away by chemical reaction of molten steel. This method is a chemical deoxidation method, and in some cases, it is also called a forced deoxidation method. The accompanying reaction equation and equilibrium constant are as follows.

$$nO + mX = X_mO_n \quad (1\text{-}5)$$

$$K = \frac{a_{XmOn}}{f_O^n f_X^m [\%X]} \quad (1\text{-}6)$$

When $X_mO_n$ produced as a reaction in molten steel is pure, the activity of the product becomes 1 and K varies according to a certain temperature value.

As X used as a deoxidizer, affinity with O must be stronger than Fe, and the following conditions must be satisfied.

(1) As [X], it must be rapidly introduced into molten steel and the reaction should be fast.

(2) The deoxidation product $X_mO_n$ should have little or no solubility in molten steel.

(3) $X_mO_n$ should be easily separated from the molten steel.

(4) Even if the surplus [X] remaining after the reaction remains in the molten steel, the steel quality should not be damaged.

(5) There should be no operational hazards (no explosive reactions) and no problems with rash or other environmental contamination.

(6) The price should be cheap and the amount used should be small.

The intensity of deoxidation is in the order of Zr, Al, Ti, Si, C, V, Cr, and Mn. This means a higher oxygen potential value and is located below in the Ellingham diagram shown in Fig. 1-7.

The formed deoxidation product is suspended in molten steel. This deoxidation product has a lower density than molten steel, so it floats in accordance with Stokes' law of spheroidal floating in liquid phase.

$$V_t = \frac{2gr^2}{9\mu}(\rho_m - \rho_{inclusion}) \quad (1\text{-}7)$$

where $V_t$ is terminal velocity (m/s), $\mu$ is viscosity(kg/m·s), r (m) is radius of the reaction product (inclusion) and $\rho$ is the density (kg/m$^3$). In order to facilitate and quickly remove inclusion, the size of inclusion should be large, the density should be low, and the viscosity of molten steel should be low. When the inclusions are formed, at least in the case of a gas or a liquid, when they come into contact with

each other, the diameters of the spheres expand. In general, the stronger the deoxidizer, the higher the melting point of the oxide, and the easier it is to become a solid at the molten steel temperature.

Although the deoxidizing power is strong, if the deoxidation reaction product is difficult to separate into molten steel, it becomes a steel that has many non-metallic inclusions and is not clean. The resulting oxide aggregates with each other to increase the particle size, and can easily be separated by floating to the surface of the bath. Deoxidation by C produces a gaseous product, so the escape is complete and does not contaminate the steel. However, vacuum treatment is required in this case.

The deoxidizing agents used in the atmosphere are Al, Si, and Mn. Al is a metal phase, and Si and Mn are added in the form of ferro-alloy. In some cases, only specific deoxidizers may be used in consideration of the effect of $X_mO_n$ as an inclusion that is not removed and mixed with residual deoxidizing elements, but in actual steelmaking, deoxidation is performed in a state in which several deoxidizing elements coexist. Also, it is used intentionally in combination. The deoxidation performed with this plurality of deoxidation elements is called complex deoxidation or cooperative deoxidation. The reason for performing such cooperative deoxidation is for the following two reasons.

(1) A strong deoxidizing effect is obtained by using each deoxidizing agent in a single deoxidizing form.
(2) The reaction product of the complex deoxidation tends to be more liquid than the deoxidation product alone, and is easily separated by floating.

Two deoxidation components of X and X' act simultaneously to become two deoxidation products of XmOn and X'mO'n. When a bond such as XmOn·X'mO'n occurs, activity of XmOn become small by binding force. Accordingly, even when Mn having a weak deoxidizing power is added, the deoxidizing effect of Al or Si can be improved.

In the complex deoxidation, a deoxidizing agent may be added at the same time as when it is added separately over time. In addition, ferro-alloy in which various deoxidizing elements are blended has been developed in recent years as a complex deoxidizing agent, with the goal of deoxidizing effect and low melting point of the product. In addition to Si-Mn, Fe-Si-Mn, Fe-Si-Mn-Al, Ca-Si-Mn, and the like are included in the combination.

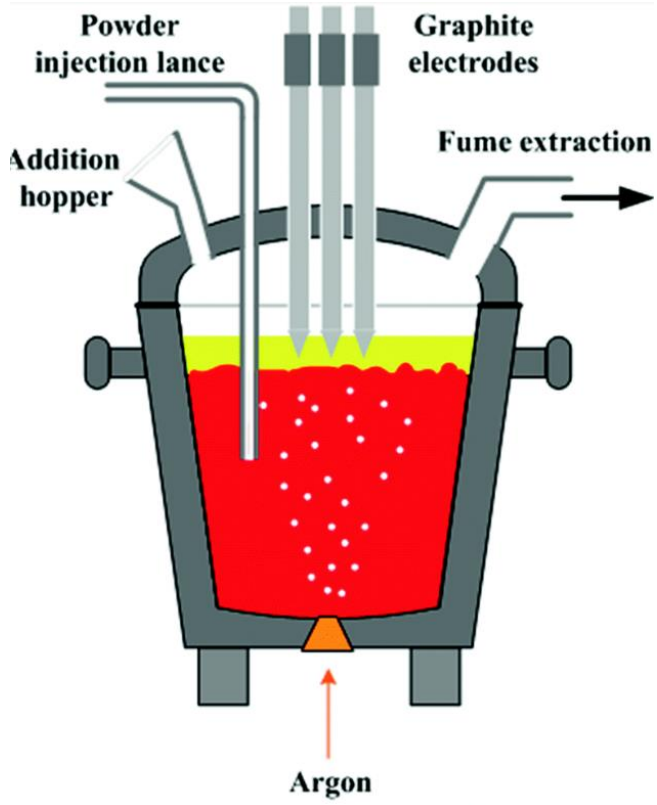


**Fig. 1-6.** Schematic of the Ladle furnace for secondary refining [12].

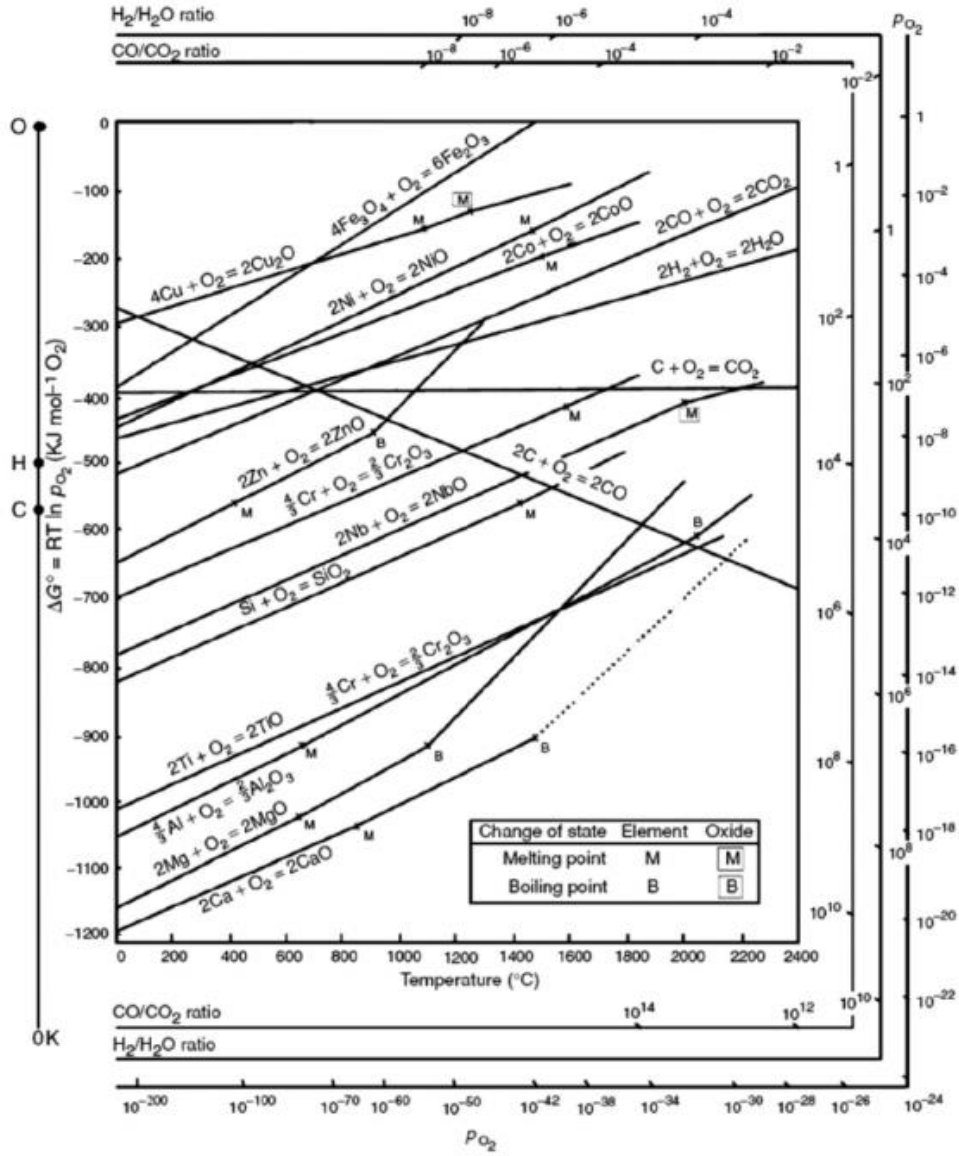


**Fig. 1-7.** Ellingham diagram for the oxygen potential based on there standard Gibbs free energy of formation over temperature [13].

## 1.4 Previous studies for the non metallic inclusion

### 1.4.1 Ladle furnace

In the ladle furnace, a wide variety of chemical reactions, such as deoxidation, desulfurization, alloying, and inclusion shape control, take place for refining. There have been many studies of deoxidation for clean steel production for decades. In the early stages of the study, studies on mixing time and flow pattern according to the bottom gas plug design were actively conducted through experiments using a water model. Optimized gas plugs were studied by measuring the mixing time according to the number of plugs, radial location, and plug configuration [14-22]. Through the concentration measurement using the sensor, a general formula for the time required for the bulk concentration to reach 95% of the equilibrium concentration was presented [16-18]. Many works used water experiment to study the velocity distribution, gas fraction profiles, bubble penetration length, rising velocity [23-27]. Recently, Li et al established water-oil-air system to predict the bubble distribution in the plume zone considering bubble breakage and collision [28].

Three methods have been proposed to simulate gas-liquid two-phase flow. In early works, plume zone was treated as a mixed single phase. It is quasi single phase model. Based on the empirical data obtained from water experiments, it was possible to obtain high-precision results with very little calculation by pre-setting spatial gas distribution and effects on the continuous phase [29-36]. As the computational capability increases, numerical simulation using the Eulerian multiphase model (E-E model) and Eulerian-Lagrangian model (E-L model) for multiphase flow analysis has been generalized. In the case of the E-L model, the

continuous phase is solved as an Eulerian concept, and the gas phase is solved by a particle tracking method using a discrete phase model [37-40]. The E-E model [41-45] is a method of solving multiple sets of equations for each phase to more accurately simulate the interaction forces between phases. The E-L model is known to be the most accurate method because it is very complicated to consider the interaction between individual particles and the calculation accuracy decreases when more than a certain volume fraction exists in the continuous phase. [46]

LOU et al. used population balance model to predict inclusion growth by collision [47]. And thermodynamics was combined with fluid dynamics to simulate desulfurization [48-49]. Although a lot of studies related to complex inclusion have been conducted, it is focused on explaining the evolution mechanism limited to thermodynamics, and research on kinetics is very rare. No studies have been published on global modeling that can simulate fluid flow and complex inclusion reactions.

### 1.4.2 Continuous casting mold

Unstable molten steel fluid flows significantly affect the quality of steel produced via conventional slab continuous casting [50]. Thomas et al. suggested via computational modeling that subsurface hooks, which are meniscus defects, could be formed by unbalanced superheat distributions with large top-surface level fluctuations [51]. Their influence on the behavior of mold inclusions and slag entrainment induced from the flow fluctuations of the surface area are linked to internal defects, such as blisters, and surface defects, such as slivers [52].

Many studies on the factors influencing flow patterns have been reported. Gupta et al. used a water model to investigate jet swirling in the mold and

confirmed the presence of asymmetric flow [53]. Ramos-Banderas et al. concluded that vertical jet movements originated from residual Reynolds stress, and that the jet fluctuations occurred continuously [54]. Huang et al. used numerical simulations to calculate the melt flow and average temperatures within the mold of a continuous caster with variables such as the depth of the submerged entry nozzle (SEN) and casting speed [55]. Zhang et al. applied similarities related to the Froude number to connect transport phenomena in a caster to those in a water model [56]. During processing, argon gas is injected to prevent nozzle clogging; the changes in flow due to gas injection have been investigated both experimentally and numerically [57-59]. However, a generally accepted destabilization mechanism has not yet been proposed. While reports have discussed flow stability criteria in the upper recirculation zone as functions of the SEN port angle [60-64], the relatively small data set hinders the identification of a definite SEN port angle trend, as well as the clear definition of the corresponding flow pattern changes. Recently, many studies have used the large eddy simulation (LES) turbulence model to analyze more realistic unsteady flow in casters [65-71]. However, the calculation cost of LES is so high that only short time ranges could be analyzed. Therefore, predictions of flow pattern periodicity are limited. Accordingly, the behaviors of unstable flow fields in molds are not yet well understood.

## 1.5 Goals of the research

In present study, we conducted a study on inclusion control in ladle furnace and continuous casting mold. First, in order to calculate the fluid flow in the ladle furnace, a numerical model was created using a quasi single phase model, and the model was validated through a water model experiment. Using a verified flow model, a reaction model was constructed to simulate mass transfer and chemical reactions, and furthermore, a numerical model for the creation of complex inclusions was developed.

In the next step, we use a water model and numerical simulation to investigate fluid flow stability in the upper circulation zone of the continuous casting mold. Because unstable flow causes not only slag entrapment but also inclusion deep penetration into slab, we propose flow stability criteria as functions of the SEN port angle and correlate the port angle with flow patterns. The formation of unstable flow patterns is quantitatively explained via their relationships with transient changes, and the origin of the fluctuation behavior is suggested.

# Chapter 2. Research method

## 2.1 Water model experiment

### 2.1.1 Water model for ladle furnace

A cylindrical acrylic ladle with dimensions of 48 cm interior diameter and 50 cm height is used for the experiments. Nitrogen is injected into the ladle through a 6 mm diameter nozzle located at the center of the bottom of the ladle. The gas flow rate is changed from 0.5 liter / min to 10 liter / min using a mass flow controller. As shown in Fig. 2-1, the ladle is opened under 1atm and the temperature is kept at 25 °C. The water height is 40 cm. Paraffin oil is selected as the slag. The physical properties of each liquid are given in Table 2-1. To analyze the effects of slag height, experiments were performed at various thicknesses of oil heights.

To distinguish the paraffin oil from water, a small amount of black dye is added to the oil. The area of the plume eye is measured by images from video recording and analysis of the area of water at the ladle surface through pixel counting (Fig. 2-2). The oil area is converted to black and water area to white using MATLAB. Average values of 30 images, each image per second, are used for the area of each condition.

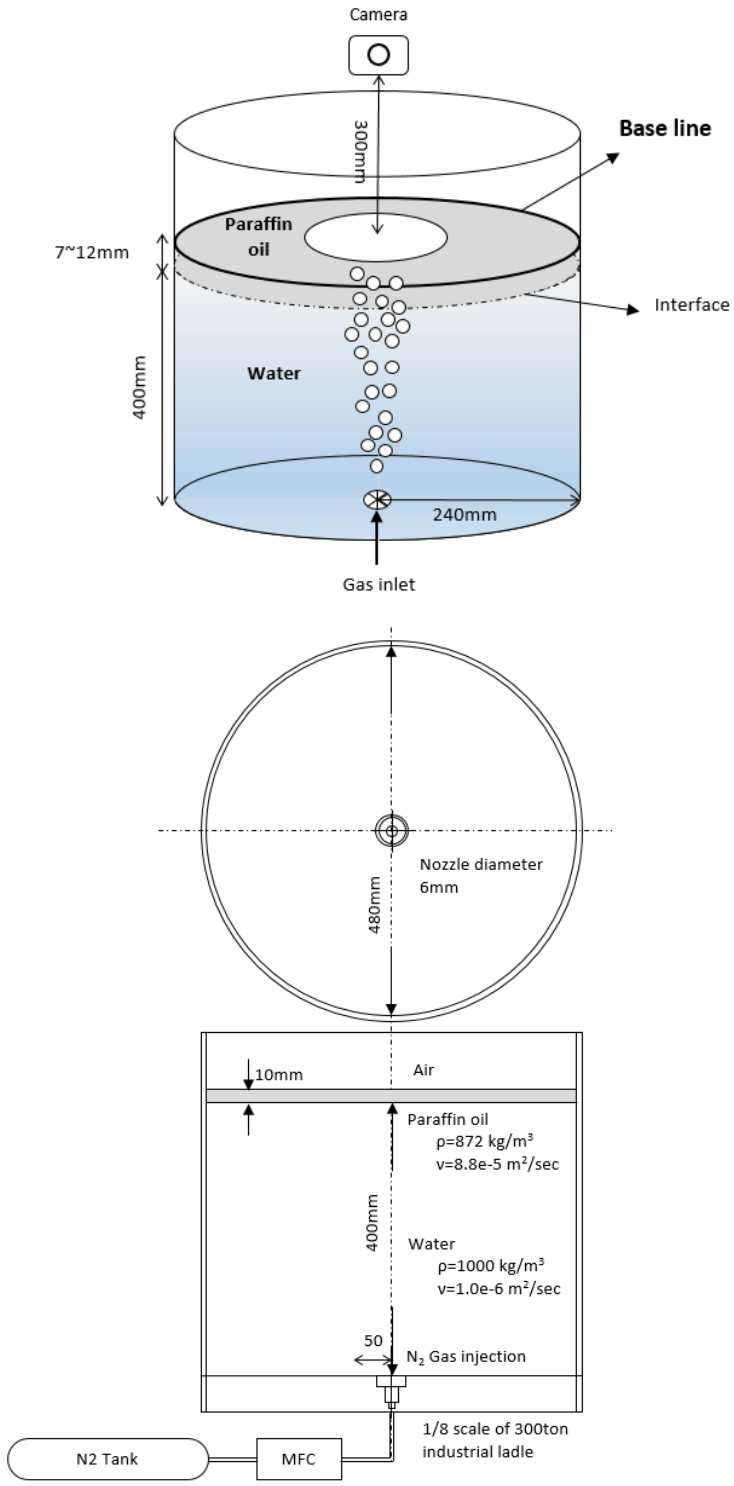


**Fig. 2-1.** Schematic of the water model experimental equipment for ladle.

**Table 2-1.** Geometric variables and material properties for water model.

| Vessel Radius | Water height | Nozzle location | Nozzle diameter | Gas flow |
|---|---|---|---|---|
| 240 mm | 400 mm | center | 6mm | 0.5~10 slm |

| Material | Kinematic-Vis ($m^2/sec$) | Density ($kg/m^3$) | $\nu_{slag}/\nu_{melt}$ |
|---|---|---|---|
| Water (25℃) | $1 \times 10^{-6}$ | 1,000 | - |
| Liq-Paraffin (40℃) | $9.14 \times 10^{-5}$ | 872 | 91.4 |
| $N_2$ (25℃) | - | 1.14 | - |

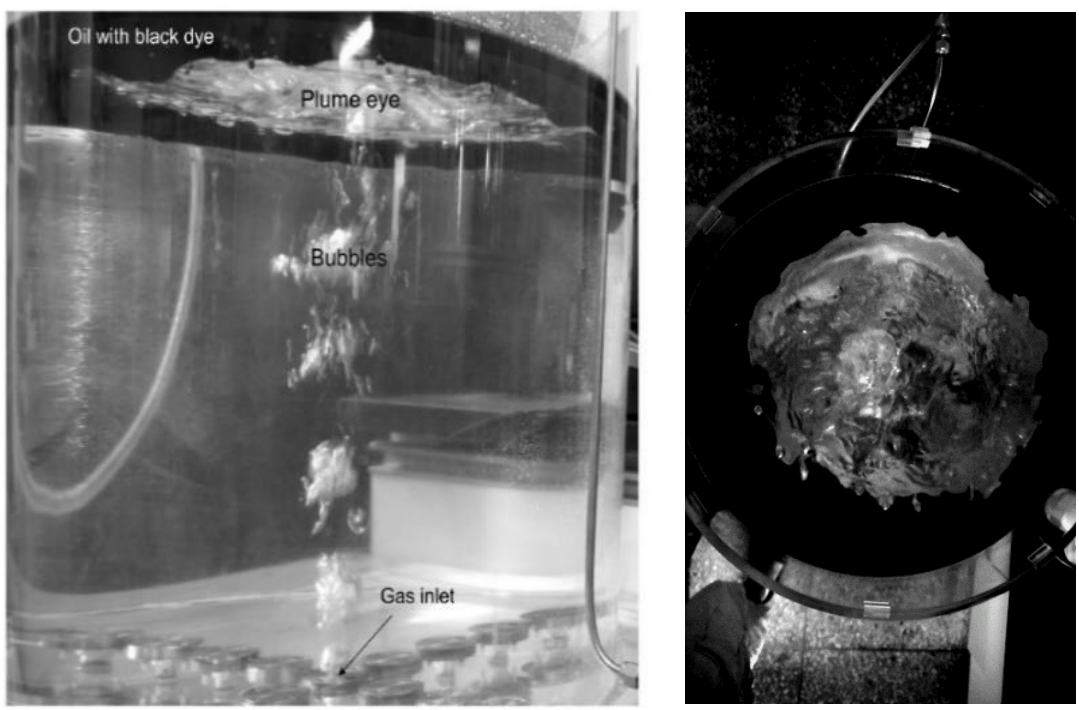


**Fig. 2-2.** Measurement of plume eye area by images from video recording.

### 2.1.2 Water model for continuous casting mold

We performed 0.5-scale water model experiments to investigate the relationship between the SEN angle and flow pattern variations in the upper recirculation zone. As shown in Fig. 2-3, the water model equipment was composed of three consecutive chambers. Each chamber was made from acrylic plates and had dimensions of 650 mm × 125 mm × 1500 mm. The first, second, and third chambers were used to observe flow within the mold, maintain the mold surface level, and store water, respectively. A 715 mm × 420 mm × 310 mm tundish was used to maintain a constant flow rate. The water in the tundish flowed down through a circular tube, then passed through the SEN for injection into the mold. Water draining from the bottom was pumped up and fed back to tundish. The flow rate regulated through the front inlet gate valve and rear gate valve and measured by mass flow meter in Fig. 1. Mass flow rate was maintained 68.94 kg/min (corresponding volume flow rate is 0.069 $m^3$/min). For gas injection experiment, the nitrogen gas was injected through the gas nozzle while water injected through tundish inlet (Fig. 2-3). Gas flow rate was 2 L/min.

Particle image velocimetry (PIV) measurements were performed using a laser and a high-resolution charge-coupled device (CCD) camera. The upper circulating flow near the wall was recorded at 100 frames/sec for 400 s. The measurement point, indicated in Fig. 1, was located at (25 mm, 62.5 mm, and 1225 mm). Velocity can be measured by tracking the movement of particles in the fluid.

Velocity was calculated with PIVlab which is time resolved digital particle image velocimetry tool for Matlab [72]. The SEN port angle, which corresponds to the slope of the fluid outlet relative to the bottom surface of the nozzle, was varied from 0 to 35° in 5° increments.

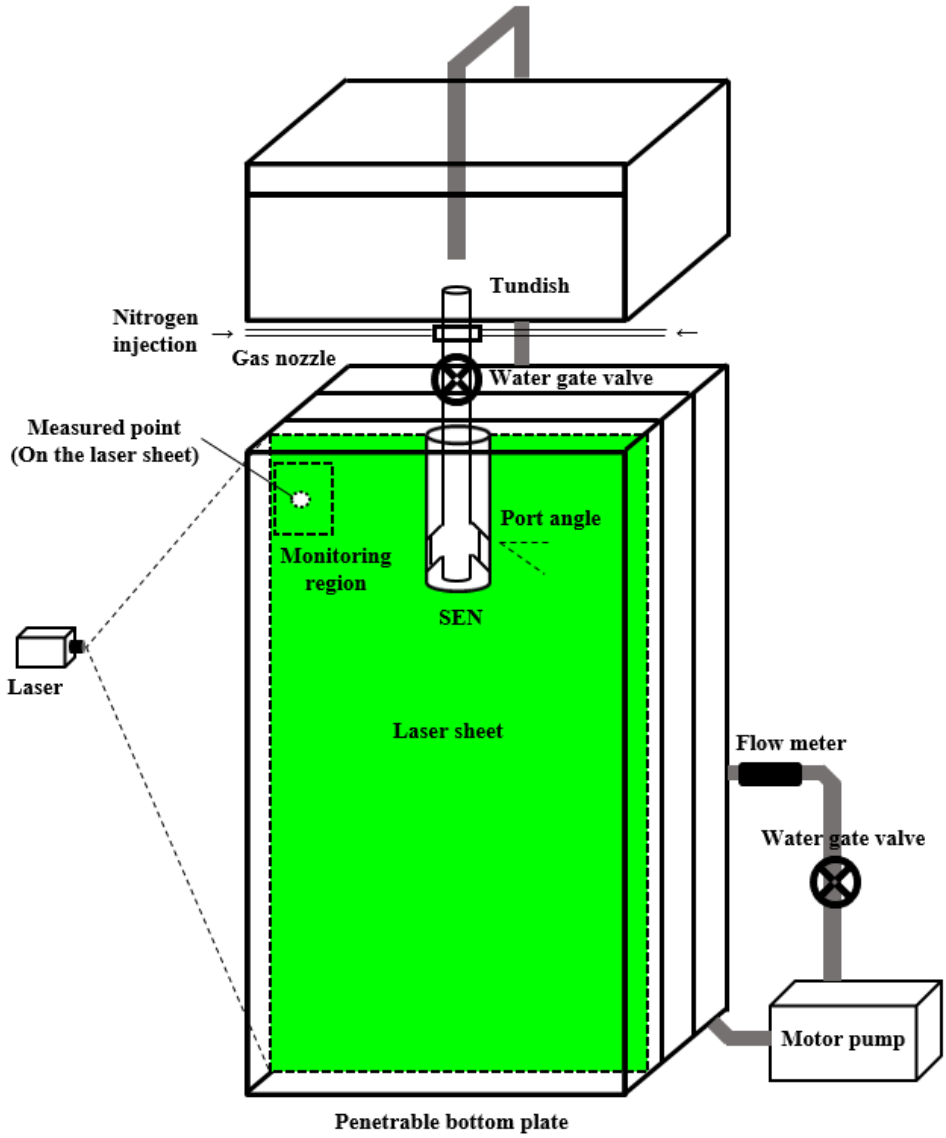


**Fig. 2-3.** Schematic of the water model experimental equipment.

## 2.2 Computational fluid dynamics simulation

### 2.2.1 Finite volume method

In the continuum simulation, the governing equation is different depending on the type of physical variable to be analyzed, and even the same governing equation can be discretized in different ways. The discretization method is mainly divided into three types, the finite difference method, the finite element method, and the finite volume method. These three methods differ in the method of deriving the matrix necessary to obtain an approximate solution.

The finite difference method derives the discretization equation directly using the talyer-series expansion of the differential term of the governing equation. Because it is relatively easy to apply, it is very effective for academic research or simply to find an answer. However, as the shape of the target object becomes more complex, it is difficult to define the rate of change in the direction of each coordinate axis, so it has a disadvantage that it is not easy to generalize.

The finite element method multiplies the governing partial differential equation by a weight function and then integrates it into the element or volume. Galerkin weighted residuals are commonly used. It is known as the most commonly used method for stress analysis. In addition to stress analysis, fluid flow analysis has the advantage that it can be applied to complex shapes compared to finite difference methods, and that the flow field can easily respond to complex boundary shapes. However, a convergence problem may occur due to a large velocity gradient near the wall, such as a large Reynolds number [73].

In the finite finite difference method or the finite element method, the number of unknowns to be determined is specified at a node located on each edge,

side, or face of the element, whereas in the finite volume method, degrees of freedom are specified at grid points inside the finite volume. The finite volume method is distinguished from the finite element method in that it takes an integral for each finite volume and constructs an approximate solution by constructing a correlation with physical quantities at adjacent grid points in the finite volume (Fig. 2-4). Accordingly, the complete conservation of quantities such as mass, momentum, and energy obtained as a result of the calculation is strictly satisfied for a certain control volume group and for the entire computational domain. The finite volume method is still known as the most powerful method for analyzing flow because it can solve the complex shape realization problem in the finite difference method mentioned above and the high Reynolds convergence problem of the finite element method.

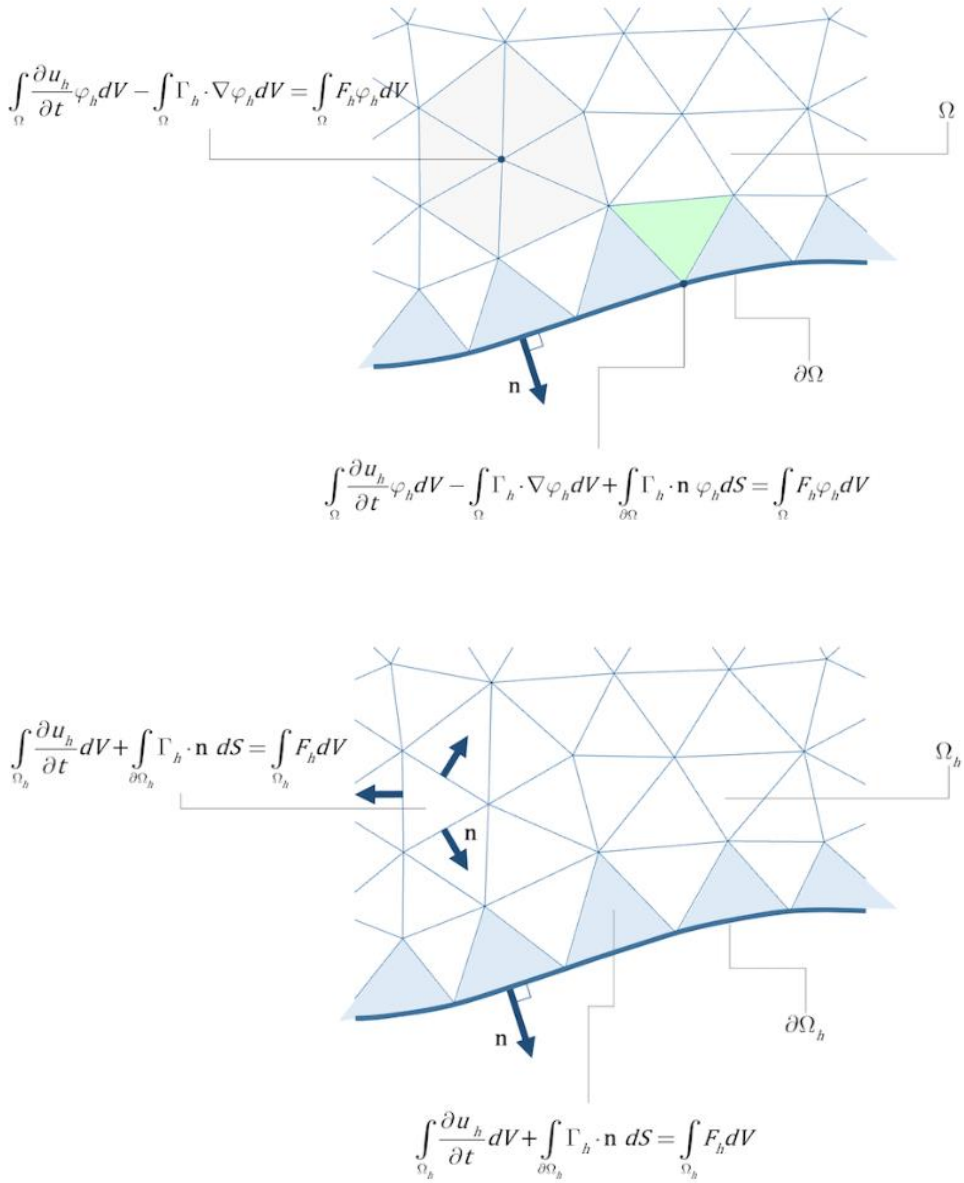


**Fig. 2-4.** Formulation of governing equation. (a) Finite element method (b) Finite volume method [74].

### 2.2.2 Fluid flow

**Mass conservation**

Conservation of mass requires that the time rate of change of mass in a control volume be balanced by the net mass flow into the same control volume (outflow - inflow). This can be expressed as:

$$\frac{\partial \rho}{\partial t} + \nabla \bullet (\rho \vec{V}) = 0 \qquad (2\text{-}1)$$

The first term on the left hand side is the time rate of change of the density (mass per unit volume). The second term describes the net mass flow across the control volume's boundaries and is called the convective term [75].

**Momentum conservation**

Newton's second law states that the time rate of change of the momentum of a fluid element is equal to the sum of the forces on the element. The x-component of the momentum equation is found by setting the rate of change of x-momentum of the fluid particle equal to the total force in the x-direction on the element due to surface stresses plus the rate of increase of x-momentum due to sources:

$$\frac{\partial (\rho u)}{\partial t} + \nabla \bullet (\rho \vec{V} u) = \frac{\partial (-p + \tau_{xx})}{\partial x} + \frac{\partial \tau_{yx}}{\partial y} + \frac{\partial \tau_{zx}}{\partial z} + S_{Mx} \qquad (2\text{-}2)$$

Similar equations can be written for the y- and z-components of the momentum equation:

$$\frac{\partial (\rho v)}{\partial t} + \nabla \bullet (\rho \vec{V} v) = \frac{\partial \tau_{xy}}{\partial x} + \frac{\partial (-p + \tau_{yy})}{\partial y} + \frac{\partial \tau_{zy}}{\partial z} + S_{My} \qquad (2\text{-}3)$$

$$\frac{\partial(\rho w)}{\partial t}+\nabla\bullet(\rho\vec{V}w)=\frac{\partial\tau_{xz}}{\partial x}+\frac{\partial\tau_{yz}}{\partial y}+\frac{\partial(-p+\tau_{zz})}{\partial z}+S_{Mz} \qquad (2\text{-}4)$$

In these equations, *p* is the static pressure and $t_{ij}$ is the viscous stress tensor [75].

**Navier-Stokes equations**

The momentum equations, given above, contain as unknowns the viscous stress components $t_{ij}$, therefore a model must be provided to define the viscous stresses.

In Newtonian flows, the viscous stresses are proportional to the deformation rates of the fluid element. The nine viscous stress components (of which six are independent for isotropic fluids) can be related to velocity gradients to produce the following shear stress terms:

$$\tau_{xx}=2\mu\frac{\partial u}{\partial x}-\frac{2}{3}u(\nabla\bullet\vec{V}) \qquad (2\text{-}5)$$

$$\tau_{yy}=2\mu\frac{\partial v}{\partial y}-\frac{2}{3}u(\nabla\bullet\vec{V}) \qquad (2\text{-}6)$$

$$\tau_{zz}=2\mu\frac{\partial w}{\partial z}-\frac{2}{3}u(\nabla\bullet\vec{V}) \qquad (2\text{-}7)$$

$$\tau_{xy}=\tau_{yx}=\mu\left(\frac{\partial u}{\partial y}+\frac{\partial v}{\partial x}\right) \qquad (2\text{-}8)$$

$$\tau_{xz}=\tau_{zx}=\mu\left(\frac{\partial u}{\partial z}+\frac{\partial w}{\partial x}\right) \qquad (2\text{-}9)$$

$$\tau_{yz}=\tau_{zy}=\mu\left(\frac{\partial v}{\partial z}+\frac{\partial w}{\partial y}\right) \qquad (2\text{-}10)$$

Substitution of the above shear stress terms into the momentum equations yields the Navier-Stokes equations:

$$\frac{\partial(\rho u)}{\partial t}+\nabla\bullet(\rho\vec{V}u)=-\frac{\partial p}{\partial x}+\frac{\partial}{\partial x}\left[2\mu\frac{\partial u}{\partial x}-\frac{2}{3}\mu(\nabla\bullet\vec{V})\right]+\frac{\partial}{\partial y}\left[\mu\left(\frac{\partial u}{\partial y}+\frac{\partial v}{\partial x}\right)\right]+\frac{\partial}{\partial z}\left[\mu\left(\frac{\partial u}{\partial z}+\frac{\partial w}{\partial x}\right)\right]+S_{Mx} \tag{2-11}$$

$$\frac{\partial(\rho v)}{\partial t}+\nabla\bullet(\rho\vec{V}v)=-\frac{\partial p}{\partial y}+\frac{\partial}{\partial x}\left[\mu\left(\frac{\partial u}{\partial y}+\frac{\partial v}{\partial x}\right)\right]+\frac{\partial}{\partial y}\left[2\mu\frac{\partial v}{\partial x}-\frac{2}{3}\mu(\nabla\bullet\vec{V})\right]+\frac{\partial}{\partial z}\left[\mu\left(\frac{\partial v}{\partial z}+\frac{\partial w}{\partial y}\right)\right]+S_{My} \tag{2-12}$$

$$\frac{\partial(\rho v)}{\partial t}+\nabla\bullet(\rho\vec{V}w)=-\frac{\partial p}{\partial z}+\frac{\partial}{\partial x}\left[\mu\left(\frac{\partial u}{\partial y}+\frac{\partial v}{\partial x}\right)\right]+\frac{\partial}{\partial y}\left[\mu\left(\frac{\partial v}{\partial z}+\frac{\partial w}{\partial x}\right)\right]+\frac{\partial}{\partial z}\left[2\mu\frac{\partial w}{\partial y}-\frac{2}{3}\mu(\nabla\bullet\vec{V})\right]+S_{Mz} \tag{2-13}$$

By rearranging these equations and moving the smaller contributions of the viscous stress terms to the momentum source term, we can rewrite the Navier-Stokes equations in a more useful form:

$$\frac{\partial(\rho u)}{\partial t}+\nabla\bullet(\rho\vec{V}u)=-\frac{\partial p}{\partial x}+\nabla\bullet(\mu\nabla u)+S_{Mx} \tag{2-14}$$

$$\frac{\partial(\rho v)}{\partial t}+\nabla\bullet(\rho\vec{V}v)=-\frac{\partial p}{\partial y}+\nabla\bullet(\mu\nabla v)+S_{My} \tag{2-15}$$

$$\frac{\partial(\rho w)}{\partial t}+\nabla\bullet(\rho\vec{V}w)=-\frac{\partial p}{\partial z}+\nabla\bullet(\mu\nabla w)+S_{Mz} \tag{2-16}$$

[75]

### 2.2.3 Turbulence model

**Theory introduction**

For more than a century the preferred approach in the treatment of

turbulent flows is to predict macroscopic statistics using the RANS formalism. Introduced by Reynolds in 1895, it involves a simple decomposition of the instantaneous fields in mean values and fluctuations via an averaging operation. The issue of turbulence modeling arises from the need to represent turbulent or Reynolds stresses, which are additional unknowns introduced by averaging the Navier-Stokes equations. The proportionality parameter is called the turbulent or eddy viscosity, and is expressed phenomenologically or obtained from transport equations. Unlike its laminar counter-part, the turbulent viscosity is not a property of the fluid but rather a characteristic of the flow.

Within the framework of RANS modeling, various models differ in the way the turbulent viscosity is calculated. These models are typically categorized by the number of additional transport equations to be solved. Almost all the models in this simulation involve solutions of two extra transport equations. One is for the turbulent kinetic energy, *k*, and the other are for the rate of dissipation, e, or the specific rate of dissipation, w.

Based upon the way the near-wall viscous sublayer is handled, these models are further classified into high-Reynolds-number and low-Reynolds-number models. Here the qualifier Reynolds-number refers to the local turbulent Reynolds number:

$$\mathrm{Re}_t = \frac{k^2}{\nu\varepsilon} \tag{2-17}$$

It will be shown that $\mathrm{Re}_t$ is proportional to the ratio of the eddy viscosity to molecular viscosity, *v*. High Reynolds models are designed for regions where the eddy viscosity is much larger than the molecular viscosity and, therefore, cannot be extended into the near-wall sublayers where viscous effects are dominating. The

standard wall-function model is used to bridge the gap between the high-Reynolds-number regions and the walls or to connect conditions at some distance from the wall with those at the wall. Low-Reynolds-number models are designed to be used in the turbulent core regions and the near-wall viscous sublayers [75].

**Standard k-e model**

We use the standard k-e model for turbulence calculation. In the model, the turbulent viscosity is expressed as:

$$\nu_t = \frac{C_\mu k^2}{\varepsilon} \tag{2-18}$$

The transport equations for *k* and e are,

$$\frac{\partial}{\partial t}(\rho k) + \frac{\partial}{\partial x_j}(\rho u_j k) = \rho P - \rho\varepsilon + \frac{\partial}{\partial x_j}\left[\left(\mu + \frac{\mu_i}{\sigma_k}\right)\frac{\partial k}{\partial x_j}\right] \tag{2-19}$$

$$\frac{\partial}{\partial t}(\rho\varepsilon) + \frac{\partial}{\partial x_j}(\rho u_j \varepsilon) = C_{\varepsilon_1}\frac{\rho P\varepsilon}{k} - C_{\varepsilon_2}\frac{\rho P\varepsilon^2}{k} + \frac{\partial}{\partial x_j}\left[\left(\mu + \frac{\mu_i}{\sigma_\varepsilon}\right)\frac{\partial \varepsilon}{\partial x_j}\right] \tag{2-20}$$

With the production term *P* defined as:

$$P = \nu_t\left(\frac{\partial u_i}{\partial x_j} + \frac{\partial u_j}{\partial x_i} + \frac{2}{3}\frac{\partial u_m}{\partial x_m}\delta_{ij}\right)\frac{\partial u_i}{\partial x_j} - \frac{2}{3}k\frac{\partial u_m}{\partial x_m} \tag{2-21}$$

The five constants used in this model are:

| $C_\mu$ | $C_{\varepsilon 1}$ | $C_{\varepsilon 2}$ | $\sigma_k$ | $\sigma_\varepsilon$ |
|---|---|---|---|---|
| 0.09 | 1.44 | 1.92 | 1.0 | 1.3 |

The standard *k*-e model is a high Reynolds model and is not intended to be used in the near-wall regions where viscous effects dominate the effects of turbulence. Instead, wall functions are used in cells adjacent to walls. Adjacent to a wall the non-dimensional wall parallel velocity is obtained from

$$u^+ = y^+ \qquad u^+ \le {y_v}^+ \tag{2-22}$$

$$u^+ = \frac{1}{\kappa}\ln\left(Ey^+\right) \qquad y^+ \le {y_v}^+ \tag{2-23}$$

Where:

$$y^+ = y\frac{u_\tau}{\nu} \qquad u^+ = \frac{u}{u_\tau} \qquad u_\tau = {C_\mu}^{1/4}k^{1/2}$$

$$k = 0.4 \qquad E = 9.0 \quad \text{for smooth walls}$$

Here ${y_v}^+$ is the viscous sublayer thickness obtained from the intersection of equation (2-38) and equation (2-39). The production and dissipation terms appearing in the turbulent kinetic energy transport equation are computed for near wall cells using:

$$\rho P = \tau_w \frac{\partial u}{\partial y} = \rho {u_\tau}^2 \frac{\partial u}{\partial y} = \rho u_\tau \frac{u}{u^+}\frac{u}{y} \tag{2-24}$$

$$\bar{\varepsilon} = \frac{{u_\tau}^3 u^+}{y} = \frac{u_\tau u^+ u_\tau {C_\mu}^2 k}{y} \tag{2-25}$$

### 2.2.4 Mass transfer

When a deoxidizer such as aluminum or calcium is added in a certain region, the species gradually moves along the fluid flow. Deoxidation reactants including dissolved oxygen, a simple oxidation product such as $Al_2O_3$, and calcium aluminates such as $(CaO)\cdot(Al_2O_3)_6$, $(CaO)\cdot(Al_2O_3)_2$ , $(CaO)\cdot(Al_2O_3)$ , slag , CaO also move along the fluid flow. The governing formula for simulating their transport is as follows [76].

$$\frac{\partial}{\partial t}(\rho Y_i) + \nabla \cdot (\rho Y_i) = -\nabla \cdot J_i + R_i + S_i \tag{2-26}$$

$Y_i$ is local mass fraction of each species. $J_i$ is the diffusion flux of species. $R_i$ is the net rate of production of species by chemical reaction. $S_i$ is the rate of creation or removal by non-reactional source, for example, inclusion removal due to slag layer attachment. An equation of this form will be solved for *N*-1 species where *N* is the total number of fluid phase chemical species present in the system. Since the mass fraction of the species must sum to unity, the $N^{th}$ mass fraction is determined as one minus the sum of the *N*-1 solved mass fractions.

In turbulent flows, mass diffusion flux is defined as

$$J_i = -(\rho D_i + \rho D_t)\nabla Y_i \tag{2-27}$$

where $D_i$ is the mass diffusion coefficient for species in the mixture and $D_t$ is the turbulent diffusivity. $R_i$ are assumed to be controlled by the turbulent mixing, ignoring the effect of chemistry timescale, which avoids expensive Arrhenius chemical kinetic calculations. This approach could be used when the chemistry timescales of interest are known to be fast relative to the turbulence timescales throughout the domain. Since the reaction rate of dissolved oxygen and Al is very fast, reaction rate based on turbulence parameter could be used. Therefore, reaction

rate is defined as follows:

$$R_i = -4\rho\varepsilon/k \min([\%i],[\%j]) \quad (2\text{-}28)$$

where $\rho$ is the density of fluid (kg/m$^3$), $\varepsilon$ is the turbulent kinetic energy dissipation (m$^2$/s$^3$), $k$ is the turbulent kinetic energy (m$^2$/s$^2$). The chemical reaction continues until the smaller quality fraction of reactant is consumed into the equilibrium concentration. The extent of reaction is determined by the smallest quality fraction of the reactants.

### 2.2.5 Discrete phase model

The discrete phase model (DPM) based on the Euler-Lagrange approach was used to calculate the influence of the secondary phase (gas) on the primary phase (water) in the continuous casting mold. The two-way coupling method was used to reflect the bi-directional interaction between two phases. The force balance and dimensionless number equations are

$$\frac{\mathrm{d}\vec{v}_p}{\mathrm{dt}} = F_D(\vec{v}\text{-}\vec{v}_p) + \frac{(\rho_P-\rho)}{F_D} + \frac{\rho}{2\rho_P}(\vec{v}_p\nabla\vec{v} - \frac{\mathrm{d}\vec{v}_p}{\mathrm{dt}}) + \frac{\rho}{\rho_P}\vec{v}_p\nabla\vec{v} \quad (2\text{-}29)$$

$$F_D = \frac{18\mu}{\rho_P {d_P}^2}\frac{C_D Re}{24} \quad (2\text{-}30)$$

$$\mathrm{Re} = \frac{\rho d_P \mid \vec{v}-\vec{v}_p \mid}{\mu} \quad (2\text{-}31)$$

$$C_D = a_1 + \frac{a_2}{Re} + \frac{a_3}{Re^2} \quad (2\text{-}32)$$

where $\vec{v}_p$ is the particle velocity, $\rho_P$ is the particle density, and $d_P$ is the particle diameter (bubble size). We set constant particle diameter to 1 mm [77, 78].

The terms on the right-hand side of Eq. 2-29 are the drag, buoyancy, and virtual mass forces, as well as the force arising from the pressure gradient. Re is the

relative Reynolds number. $C_D$ is the drag coefficient and $a_1$, $a_2$, and $a_3$ are constants associated with Re [79].

# Chapter 3. Inclusion control in ladle furnace

## 3.1 Three phase flow

### 3.1.1 Interphase force between gas and liquid

To verify the model through comparison with water model experiment, a domain of 1/8 scale of the actual ladle was used. The geometry and mesh of a 1/8 scale water model for analyzing a three-phase flow consisting of Molten steel (water)-Ar gas (N2 gas)-slag (paraffin oil) is shown in Fig. 3-1. A total of 210,000 grids were used for calculation by dividing 50 in the radial direction, 50 in the azimuthal direction, and 100 in the height direction using a cylindrical grid. 96 grids from the bottom to the height were used for molten steel regions, and 4 grids from 97 to 100 were used for slag regions.

Iguchi et al.'s empirical equation was used to determine the plume shape of the gas injected from the bottom of the ladle [80]. The radial distance of the plume according to the height is as follows.

$$b_\alpha = b_\alpha(z_0)(z/z_0)^n$$

$$b_\alpha(z_0) = 0.26(G^2/g)^{0.2}(z/z_0)^n$$

$$z_0 = 0.77 d_{in}(\rho_l/\rho_g)^{0.28}\mathrm{Fr}'^{0.89(\rho_l/\rho_g)^{-0.16}}$$

$$\mathrm{Fr}' = \frac{\rho_g Q^2}{\rho_l g {d_{in}}^5}$$

$$r_p = 1.7 b_\alpha \quad (3\text{-}1)$$

Where $b_\alpha$ is the radial distance of the plume at the center line (m). Q is the gas flow rate ($m^3$/sec), $\rho_l$ and $\rho_g$ are the density of the melt and gas (kg/m3). g is the gravity acceleration (m/$sec^2$) $d_{in}$ is the diameter of nozzle(m) and $r_p$ is the radius of gas plume.

The definition of gas fraction α is as follows.

$$\alpha = \frac{V_g}{V_{plume}} \tag{3-2}$$

$V_g$ and $V_{plume}$ is the volume of gas and plume, and $V_g$ can be calculated as follows considering the effective pressure $P_{eff}$ and slip velocity $u_{slip}$ considering iron static pressure.

$$V_g = \frac{\mathrm{Q}}{(u_{slip} + u_{melt})P_{eff}}$$

$$P_{eff} = \frac{101325+\rho_l gh}{101325} \tag{3-3}$$

h is the height of the liquid (m), a value of 0.3 m/s was used for the water, and 0.5 m/s for the steel melt [81]. Since the gas injected from the bottom causes forced convection of the liquid by buoyancy, it is very important to reflect its influence. The drift flux model proposed by Graham et al. was used to calculate the force of the gas on the liquid [82]. The momentum source of gas per unit volume on liquid is as follows.

$$\mathrm{S} = \alpha(1-\alpha)g(\rho_l - \rho_{gas}) \tag{3-4}$$

Eq. 3-4 was applied to the source term of the momentum equation mentioned in Section 2.2.

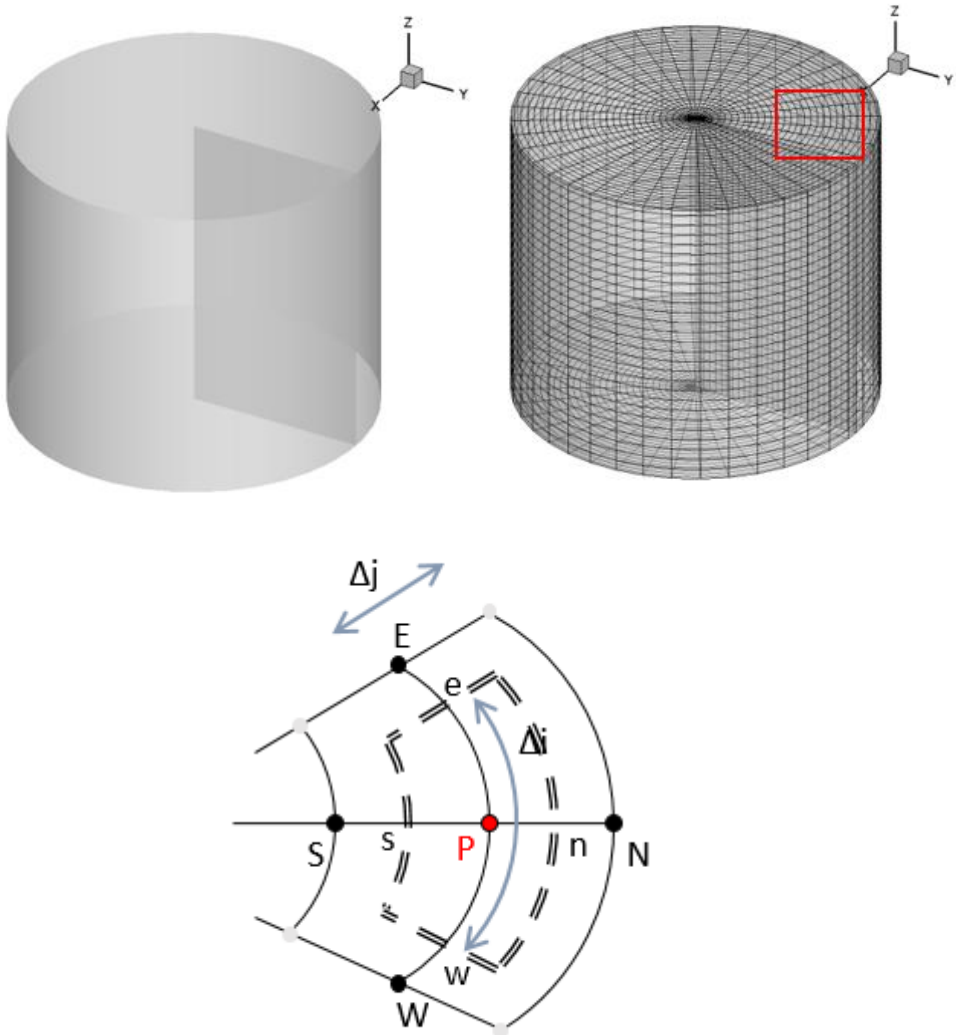


**Fig. 3-1.** Domain and cylindrical grid for numerical calculation.

### 3.1.2 Slag deformation

The convection of water generated by gas injection causes deformation of slag. It is very important to consider slag deformation because the slag acts as a wall to hinder the movement of nearby fluids. The process of slag deformation is shown in Fig. 3-2. The kinetic energy of the water derived from the gas pushes the oil floating on the water and generates spout. As the gas rise induces water in the plume region, a region is created that rises higher than the surface of the initial oil at the top of the plume region. As a result, the surface of the water can be expressed as a convex area and this area is called plume eye. The height at which water can push oil in the plume area is expressed as follows.

$$P_m = \rho_s * g * h \tag{3-5}$$

$P_m$ is the pressure of water, $\rho_s$ is the density of oil, g is gravity, and h is the height at which oil can be pushed up with water pressure.

However, as a result of actual observation, the size of the plume eye is much wider than the spout, which means that kinetic energy acts in the horizontal direction in addition to the rising pressure of water acting on the bottom of the oil. The relationship between kinetic energy and potential energy of water and oil can be expressed as follows.

$$\frac{1}{2}\rho_m v_m^2 + \rho_m g\Delta h = \frac{1}{2}\rho_s v_s^2 + \rho_s g\Delta h \tag{3-6}$$

The left side of Eq. 3-6 represents the energy sum for water (melt), and the right side represents the energy sum for oil (slag). As shown in Fig. 3-2(b), if the thickness of the initial oil is $h_0$ and the base line is the surface of the initial oil, $\Delta h$ in the potential energy term on the left side becomes 0 at the interface. The velocity of the right-hand side also becomes 0 at the interface, so we can simplify

the expression as follows.

$$v_m = \sqrt{\frac{2\rho_s g \Delta h}{\rho_m}} \tag{3-7}$$

Eq.3-7 represents the speed of water required for the expansion of the plume eye. As the size of the plume eye increases, the thickness of the oil increases. Therefore, the increase in oil thickness according to the volume of water in place of the oil region Δh can be expressed as follows.

$$\Delta h = \frac{V_{slag}}{(V_{slag} - V_{eye})} * h_0 - h_0 = h_{all} - h_0 \tag{3-8}$$

When the diameter of the plume eye becomes equal to the diameter of the ladle, the increased oil thickness Δh becomes infinite, and the velocity $v_m$ required for the plume eye to expand also requires an infinite velocity. Fig. 3-3 shows the velocity values required for the plume eye. When the velocity value calculated by solving the mass conservation equation, momentum equation, and turbulence model mentioned in section 2.2 becomes larger than the velocity value required for slag expansion, a series of changing the material properties of the previously set cell to the value of water. A steady state flow result reflecting slag deformation could be obtatined by repeated calculation.

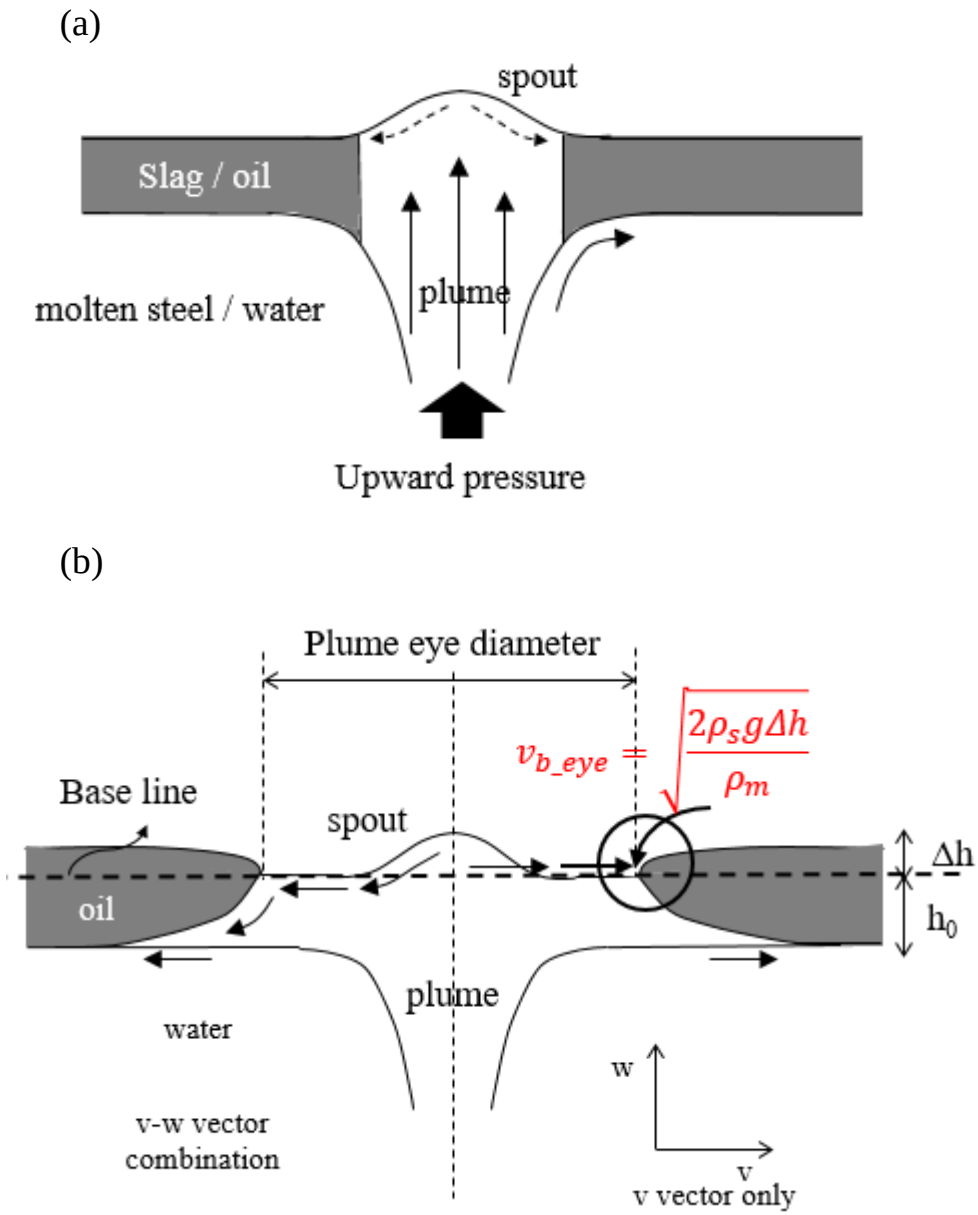


**Fig. 3-2.** Slag deformation by convective flow. (a) plume eye open (b) plume eye expansion.

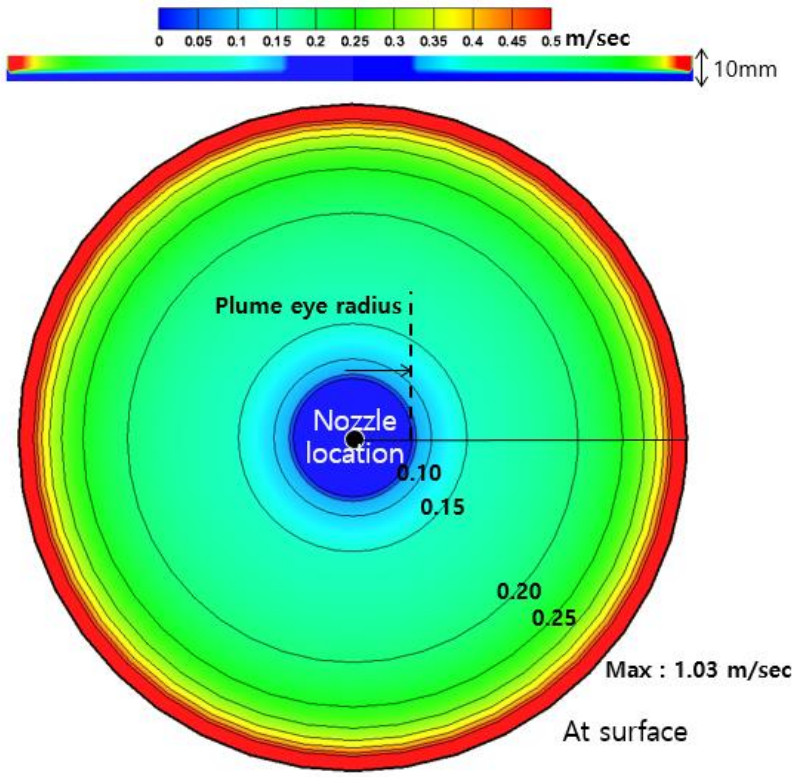


**Fig. 3-3.** Value of velocity needed for plume eye expansion

### 3.1.3 Results and discussion

Fig. 3-4 is the flow result of the simulation when 1, 4, and 7 L/min of gas are injected. Water is forced to convection by the buoyancy force of the gas input from the lower part. From the upper part of the ladle, the upward soaring flow occurs, forming a clockwise and counterclockwise circulation flow to the right and left, respectively. As the gas input amount increases, the velocity of the circulating fluid gradually increases. In the actual ladle, since elements such as Al and Ca injected for the purpose of deoxidation are transported along these flows, the faster the fluid velocity is formed, the longer the circulation length per unit time, and more active mixing can be expected.

As shown in Fig. 3-4(a), when there is no slag, only the absolute difference in velocity at the same position exists, and the flow pattern according to the gas flow rate is the same. However, when slag is present, the slag acts as a wall, interfering with the flow of fluid, and the flow pattern varies depending on the degree of deformation of the slag. As the gas flow rate increases, the degree of plume eye expansion increases, and accordingly, the slag at the top is gradually pushed, so the position of the circulation point shifts from the ladle center to the side wall. The presence or absence of slag greatly affects the absolute value of the velocity formed at the same location. When slag is present, momentum loss occurs at the interface between the fluid and slag, so even if the same flow rate gas is applied, the velocity magnitude decrease remarkably.

In most studies using the E-E model, the free surface of the melt is assumed to be flat and the fluid flow is calculated without the influence of slag.Therefore, the flow pattern is obtained only as shown in Figure 3-4(a). It leads to a large error to predict mixing time of species and homogenization. In addition,

since shifting of the circulation point cannot be considered, a large error in a location where a chemical reaction occurs. This study has significance in overcoming these difficulties.

(a)

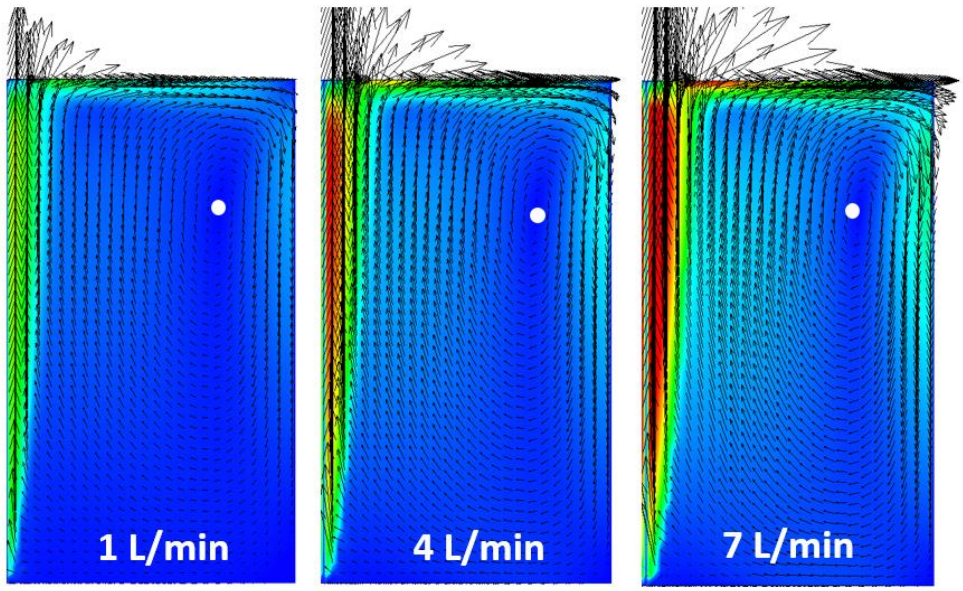


(b)

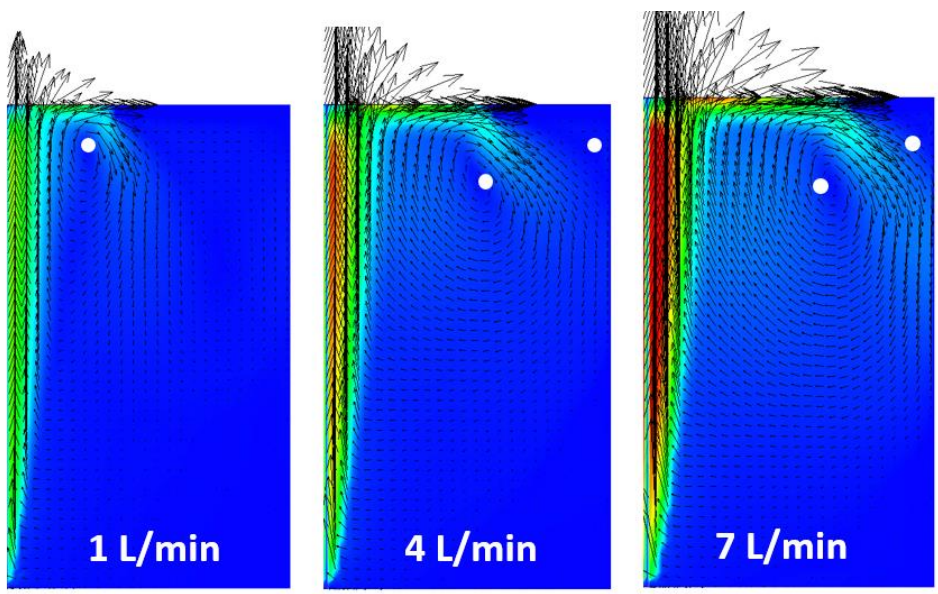


**Fig. 3-4.** Flow result of the water model. (a) no slag condition (b) with 1.2cm slag condition.

To verify the reliability of the model, the experimental results and simulation results for the plume eye area of the water model were compared. Result is shown in Figure 3-5. It was confirmed that the measured value and the prediction value through simulation were matched very well. Accordingly we applied current fluid flow mold to the real scale 300ton ladle. A reaction model was developed based on fluid molten steel-Ar gas-slag three phase flow result.

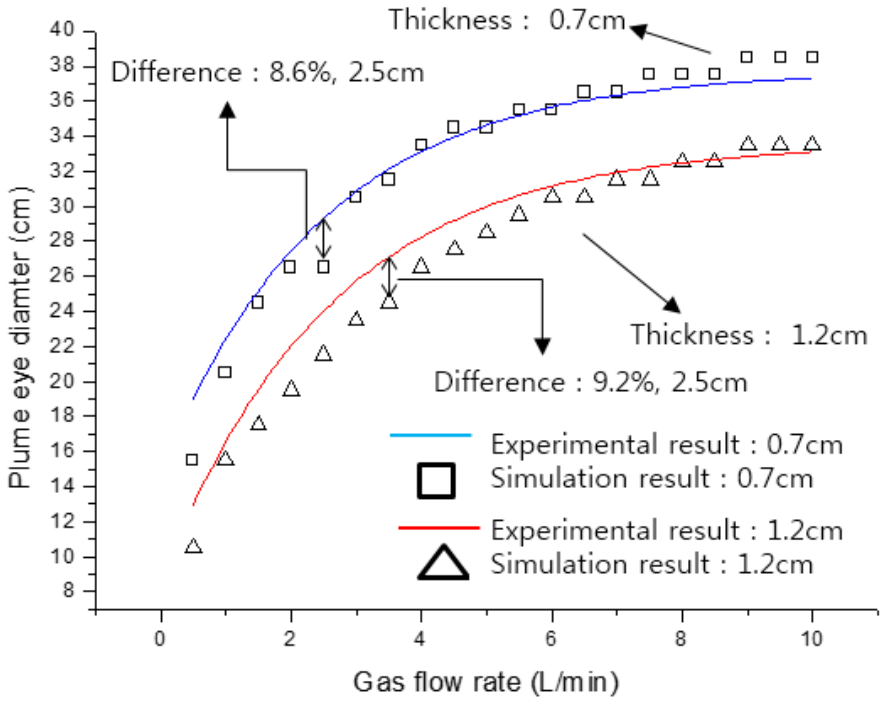


**Fig. 3-5.** Simulation and measured result of plume eye diameter.

## 3.2 Chemical reaction: Alumina inclusion generation

### 3.2.1 Thermodynamics of Al-O reaction

In the steel smelting process, the reaction has been calculated based on Wagner formalism [83], which considers the interaction between the materials forming the reaction. Al deoxidation process is a reaction in which two substances Al and O dissolved in molten steel meet to form pure solid Al2O3. The general formula for deoxidation is as follows.

$$n[A] + m[B] = A_nB_m \tag{3-9}$$

$$\Delta G = G_{final} - G_{initial} = \Delta G^0 + \mathrm{RT}\ln\frac{a_{A_nB_m}}{a_A^n a_B^m} \tag{3-10}$$

$\frac{a_{A_nB_m}}{a_A^n a_B^m}$ is the equilibrium constant K and is determined by the ratio of the activity of the reactant and product at fixed temperature. If the product is a pure solid and the reactants in the molten steel follow Henry's law, then K can be rewritten as

$$\mathrm{K} = \frac{1}{a_A^n a_B^m} = \frac{1}{(X_A^n f_A^n)\cdot(X_B^m f_B^m)}$$

$$f_A = exp\left(\varepsilon_A^B * X_B + \varepsilon_A^A * X_A\right)$$

$$f_B = exp\left(\varepsilon_B^A * X_A + \varepsilon_B^B * X_B\right) \tag{3-11}$$

X represents the mole fraction of each substance and ε is the first order interaction coefficient. When the deoxidation reaction occurs, the interaction coefficient between the deoxidizer and oxygen generally shows a negative value, and generally, the closer the oxygen is, the smaller the value.

Wagner formalism requires four constants $(\varepsilon_A^B, \varepsilon_A^A, \varepsilon_B^A, \varepsilon_B^B)$ to calculate the equilibrium constants of the two reactions, and 9 constants when the number of elements participating in the reaction system increases by one more, If the number increases, 16 constants are needed. Wagner formalism is based on the premise that

two dissolved substances behave as independent and random distribute particles [84]. However, substances with strong attractive interactions with each other, such as deoxidizers and oxygen, exist in the form of A*B Associate or A2*B Associate rather than performing independent activities in molten steel [85]. The equilibrium constant of the reaction between aluminum and oxygen is as follows.

$$K_{Al*O} = \frac{a_{Al*O}}{a_{Al}a_O} = \frac{f_{Al*O}X_{Al*O}}{(f_{Al}X_{Al})(f_O X_O)} = \frac{X_{Al*O}}{(f_{Al}X_{Al})X_O} \quad (3\text{-}12)$$

$$K_{Al2*O} = \frac{a_{Al2*O}}{a_{Al}^2 a_O} = \frac{f_{Al2*O}X_{Al2*O}}{(f_{Al}X_{Al})^2(f_O X_O)} = \frac{X_{Al2*O}}{(f_{Al}X_{Al})^2 X_O} \quad (3\text{-}13)$$

For Al2O3 formation reaction from Associate, the equilibrium constant can be expressed as follows.

$$K_{Al2O3} = \frac{1}{a_{Al*O}^2 a_O} = \frac{1}{(f_{Al*O}X_{Al*O})^2(f_O X_O)} = \frac{1}{X_{Al*O}^2 X_O} \quad (3\text{-}14)$$

$$K_{Al2O3} = \frac{1}{a_{Al2*O}a_O^2} = \frac{1}{(f_{Al2*O}X_{Al*O})(f_O X_O)^2} = \frac{1}{X_O^2 X_{Al2*O}} \quad (3\text{-}15)$$

In-Ho Jung et al. [85] proposed to calculate the fugacity required for each reaction as follows.

$$\ln f_{Al} = \varepsilon_{Al}^{Al} X_{Al} \quad (3\text{-}16)$$

$$f_O = f_{Al*O} = f_{Al2*O} = 1 \quad (3\text{-}17)$$

Unlike the interaction coefficient calculated based on the Wagner formalism, the formation of an Associate is assumed from the dissolved state of the two

substances, so it is different from the known Wagner based interaction coefficient. However, knowing the self-interaction coefficient of the material to be added as a deoxidizer and the mole fraction of each material makes it easy to calculate a fairly complex reaction system.

### 3.2.2 Direction and quantity of Al-O reaction

When the free energy of 2[Al] and 3[O] is $G_{initial}$ and the free energy of Al2O3 is $G_{final}$, in order for a spontaneous reaction to occur, $G_{initial} > G_{final}$. If Al2O3 is formed by the reaction of 2Al and 3O as a forward reaction, ΔG in the forward reaction should always have a negative value. Assuming that the two materials are in chemical equilibrium, the following relation is satisfied.

$$\exp\left(\frac{-\Delta G^0}{RT}\right) = \frac{a_{Product}}{a_{Reactant}^n a_{Base}^m} \quad (3\text{-}18)$$

When a positive reaction occurs, consumption of two reactants occurs, and when a reverse reaction occurs, decomposition of the product occurs. If this is expressed as an inequality sign, it is as follows.

$$\text{(forward reaction)} \quad \exp\left(\frac{-\Delta G^0}{RT}\right) > \frac{a_{Product}}{a_{Reactant}^n a_{Base}^m} \quad (3\text{-}19)$$

$$\text{(backward reaction)} \quad \exp\left(\frac{-\Delta G^0}{RT}\right) < \frac{a_{Product}}{a_{Reactant}^n a_{Base}^m} \quad (3\text{-}20)$$

When the reaction occurs, the reactants and products are consumed according to a unique stoichiometric ratio and continue to react until equilibrium is reached. The free energy of the system can be obtained through Eq. 3-21, 22 and the formation

of pure substance 1mole of deoxidation element Gibbs free energy ($G^0$) and the Gibbs energy change accompanying the reaction are summarized in Table 3-1.

$$G = \sum n_i g_i^0 + RT \sum n_i \ln X_i + RT \sum n_i \ln f_i \quad (3\text{-}21)$$

$$X_i = n_i/(n_{Fe} + n_M + n_O + n_{M*O} + n_{M2*O}) \quad (3\text{-}22)$$

The algorithm of this simulation program is shown in Fig. 3-6. The program consists of four parts. In the input part, determine the input amount, input time and input location of the alloying element, or specify the initial alloy concentration. In addition, there is a database part that calculates the pure gibbs energy and henrian constant of reaction elements, the number of element bonds required to form a stable compound, the interaction coefficient of elements, and the ΔG required to form a compound. There are reaction parts that treat and update the concentration information related to consumption and production, and output parts that display residual reactants and monitoring the species.

Particularly, in the reaction part, the species transport equation mentioned in Section 2.2 was solved to track the concentration of elements moving along the flow at all positions and all times, and the direction of the reaction was determined by comparison with the equilibrium constant. Since the reaction rate of Al and O dissolved in molten steel is very fast, it is assumed that the reaction is controlled by turbulence. At each time step, after the chemical reaction in all cells, the amount of the remaining reactants and the amount of products were updated, and transport calculation of each chemical species was carried out.

**Table 3-1.** $Al_2O_3$ reaction formula and $\Delta G$ by associate model

| Chemical Formula | Delta G (J/mol) | References |
|---|---|---|
| $2\ Al_{(l)} + 1.5\ O_{2(g)} = Al_2O_{3(s)}$ | $\Delta G_1 = G^0_{Al2O3} - 2G^0_{Al} - 1.5G^0_{O2}$ | [86-89] |
| $Al_{(l)} = [Al]$ | $\Delta G_2 = RT * -15{,}280 /T + 3.5$ | [84] |
| $O2_{(g)} = [O]$ | $\Delta G_3 = RT * -7{,}596.7/T + 1.2$ | [84] |
| $2\ [Al] + 3[O] = Al_2O_3$ | $\Delta G_4 = \Delta G_1 - 2\ \Delta G_2 - 3\Delta G_3$ | |
| $[Al] + [O] = [Al*O]$ (associate) | $\Delta G_5 = -108{,}614$ | [84] |
| $2\ [Al*O] + [O] = Al_2O_{3(s)}$ | $\Delta G_6 = \Delta G_4 - 2\ \Delta G_5$ | |
| $2\ [Al] + [O] = [Al_2*O]$ (associate) | $\Delta G_7 = -179{,}912$ | [84] |
| $[Al_2*O] + 2[O] = Al_2O_{3(s)}$ | $\Delta G_8 = \Delta G_4 - \Delta G_7$ | |

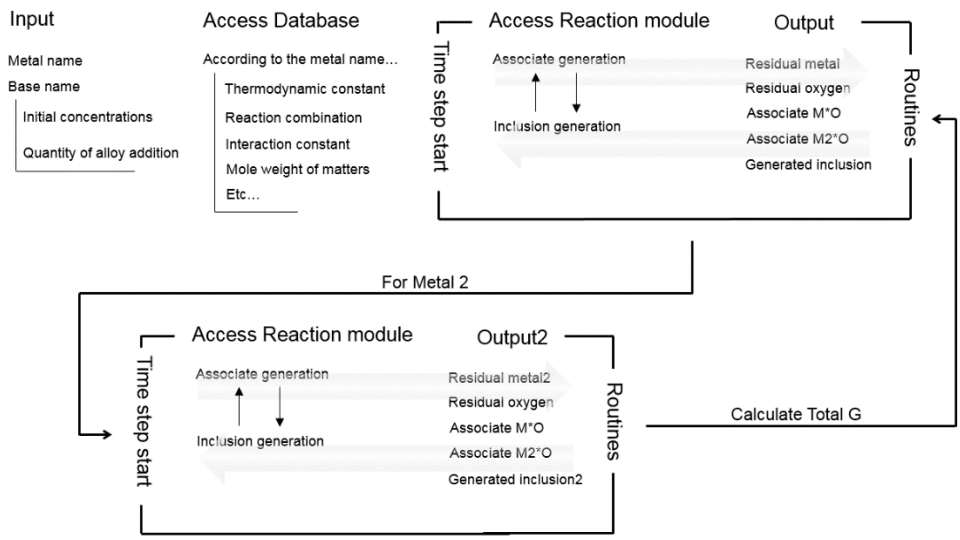


**Fig. 3-6.** Algorithm of the simple deoxidation model.

### 3.2.3 Result and discussion

To simulate a 300ton ladle of a real scale, a domain with a radial distance of 2.0m and a height of 3.5m and a cylindrical grid were used as shown in Fig. 3-7. 4 grids in the height direction of the upper part were allocated to the slag, and the initial batch was performed so that the slag could exist 10cm. The flow field of molten steel – Ar gas – slag three phase was calculated using the flow analysis model developed in Section 3.1. Table 3-2 shows the material properties used in the calculation.

The calculated flow result of molten steel inside the ladle when 30 m3/hour argon gas is injected from the bottom center nozzle is shown in Figure 3-8. The injected gas causes an upward flow of melt along the centerline, and accordingly, a symmetric circulation flow occurs on the right and left sides of the centerline. It was confirmed that the deformation of the slag was well reflected, and accordingly, the area of the plume eye would be 1.53 $m^2$, and the average speed of melt was predicted to be 0.06 m/sec.

Species transport equation was solved using the steady state flow field information and setting the initial condition value of the amount of oxygen dissolved in the molten steel to 300 ppm, designating the center of the plume eye region as the Al injection point, and adding 500 ppm of Al. The results are shown in Figure 3-9. The injected Al move along the outermost circulation flow. The dissolved oxygen inside the molten steel meets Al and immediately forms $Al_2O_3$, and the dissolved oxygen concentration decreases rapidly. As a result, the formed alumina slowly spreads to the eddy located in the center of circulation and homogenizes along the flow.

The concentrations of the product Al2O3 and reactants O and Al all differ at every time and in every location. Therefore, in order to efficiently monitor the behavior of concentration values over time, the concentration of each species is averaged over the entire cell and the values are shown in Fig. 3-10. The formula for cell average is as follows.

$$\mathrm{C} = \frac{\sum_i C_i \cdot V_i}{\sum_i V_i} \tag{3-22}$$

$\mathrm{C}$ is cell averaged concentration value (ppm), $C_i$ is the concentration of each cell (ppm), $V_i$ is the volume of each cell ($m^3$). Initially, 300 ppm of dissolved oxygen and 500 ppm of injected Al proceed at a very rapid rate immediately after the injection. But the remaining amount of reactants decreases gradually and the overall reaction slow down. This can be confirmed from the gradually decreasing slope of the graph. About 100 seconds after injection, it is predicted that the equilibrium state will be reached and 623.27 ppm of Al2O3 will be formed. The concentration of dissolved oxygen is reduced to 3.27 ppm, and 98.91% of dissolved oxygen is expected to be refined as a result of the reaction. Equilibrium concentrations were compared with the thermodynamic program Factsage 6.4 [90] to verify the reliability of the calculated results. As a result of calculation of factgae, the concentration of $Al_2O_3$ was 624.83 ppm and the concentration of Al remaining after the reaction was 167.46 ppm. The residual dissolved oxygen amount was 4.79 ppm, which showed very little error with the model results of this study.

Accordingly, the currently developed deoxidation model not only accurately

predicts equilibrium, but also predicts the process time to reach equilibrium, and monitors the amount of reactants and products over time and location. There is great significance in being able to provide important and immediate process information.

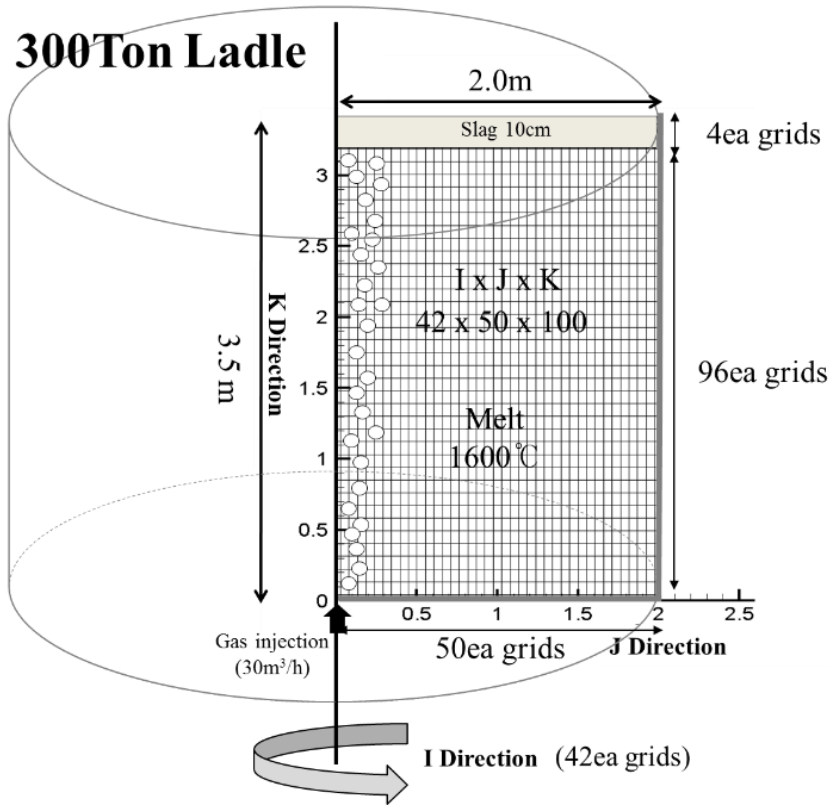


**Fig. 3-7.** Geometry and mesh for numerical simulation of 300 ton ladle.

**Table 3-2.** Material properties for numerical simulation of 300 ton ladle.

| **Elements(1580℃)** | | **Value** | **Unit** |
|---|---|---|---|
| Molten Iron (Fe) | Density | 7000 | $Kg/m^3$ |
| | Dynamic viscosity | 0.007 | Kg/m-sec |
| Injection Gas (Ar) | Density | 0.26 | $Kg/m^3$ |
| Slag (CaO 50%, $SiO_2$ 50%) [7] | Density | 2600 | $Kg/m^3$ |
| | Dynamic viscosity | 0.23 | Kg/m-sec |
| | Surface Tension | 0.45 | $Joule/m^2$ |

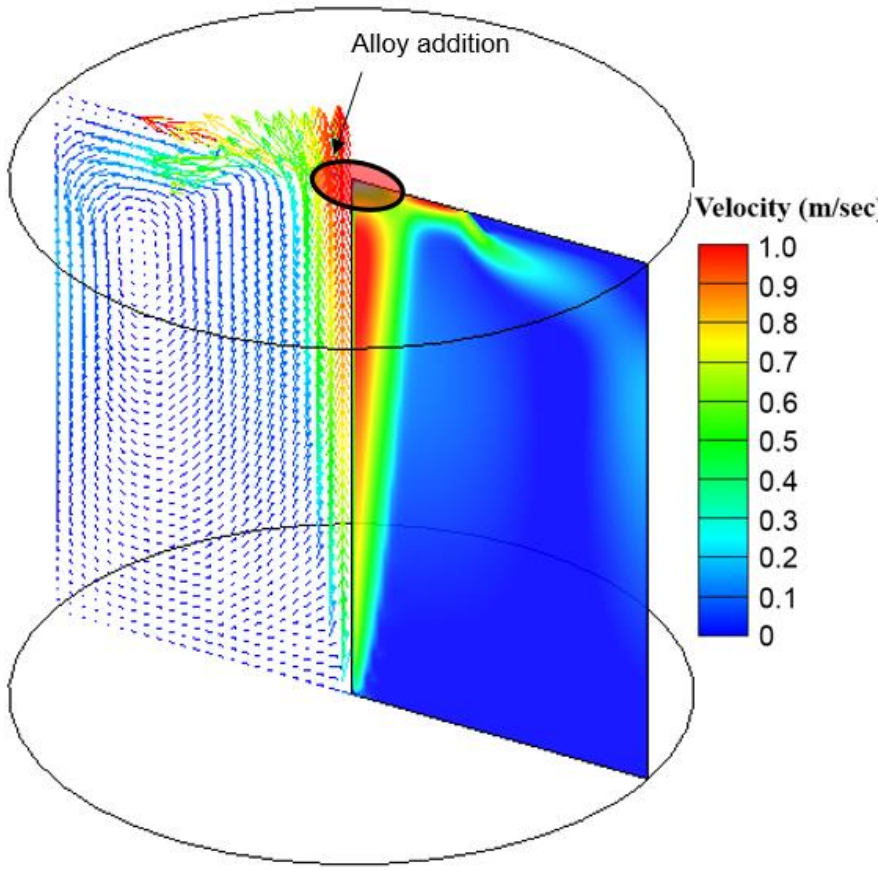


**Fig. 3-8.** Flow result of 300ton ladle. Ar gas flow rate is 500 SLM and 10cm of 50% CaO-50% $SiO_2$ slag 10cm was considered.

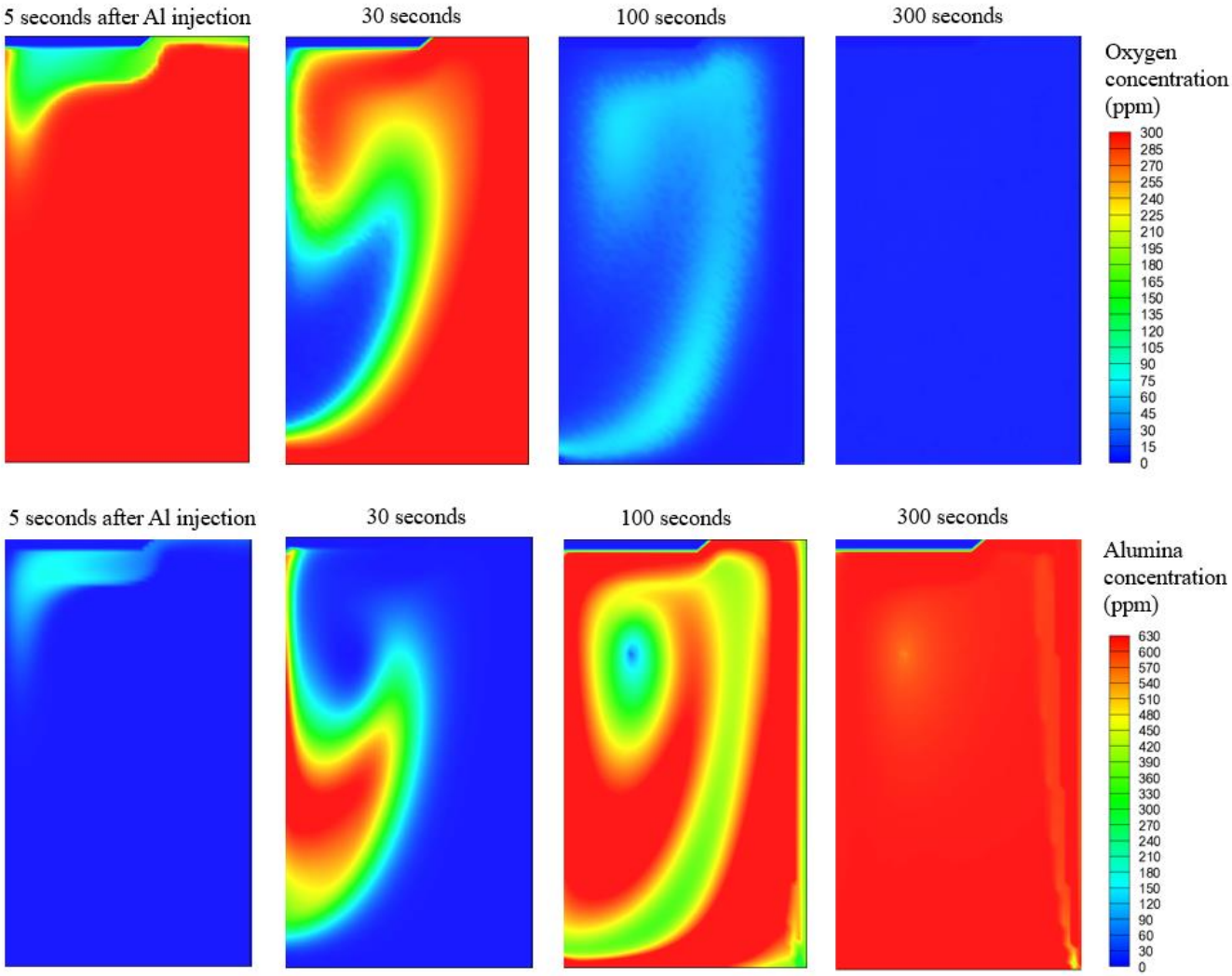


**Fig. 3-9.** Simulation result of 500 ppm [Al] - 300 ppm [O] reaction in melt.

Dissolved oxygen and alumina distribution according to the process time.

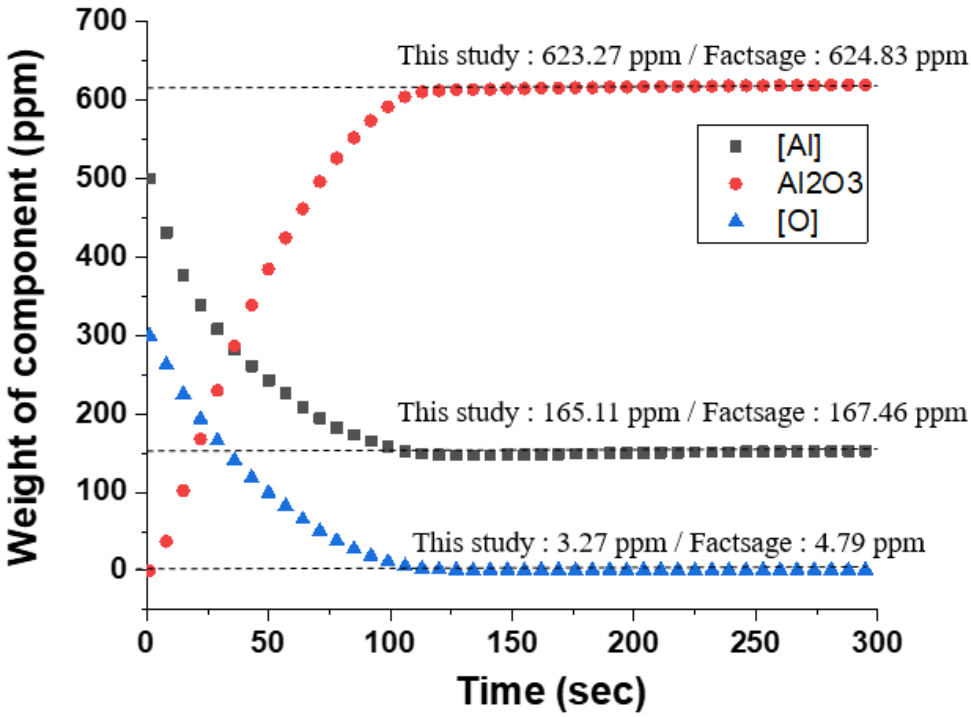


**Fig. 3-10.** 500ppm [Al] – 300ppm [O] reaction result. Cell averaged concentration of the species in deoxidation reaction.

## 3.3 Chemical reaction: Calcium aluminate inclusion generation

### 3.3.1 Thermodynamics of Ca-$Al_2O_3$ reaction

Since the dissolved oxygen was reduced enough through the primary deoxidation reaction using Al, the additional deoxdation reaction was not intended to reduce dissolved oxygen. As shown in Fig. 3-11, $Al_2O_3$ produced in the primary deoxidation reaction process forms a cluster with a net work structure, so it has a high apparent density and is not easy to separate into slag. Accordingly, the addition of Ca is aimed at promoting the formation of a spherical complex inclusion with a low melting point, thereby promoting flotation of slag. Since Ca has a higher oxygen affinity than Al, additionally injected Ca has the property of taking oxygen from Al2O3 to make oxide. Calcium aluminate, which is reaction product of Ca and $Al_2O_3$, has various allotropes. CaO, $(CaO)_3 \cdot (Al2O3)_1$, CaO·Al2O3, CaO·(Al2O3)2, $CaO \cdot (Al2O3)_6$, which have a ixed stoichiometric ratio. The formation Gibbs free energy of solid calcium aluminate is shown in Table 3-3.

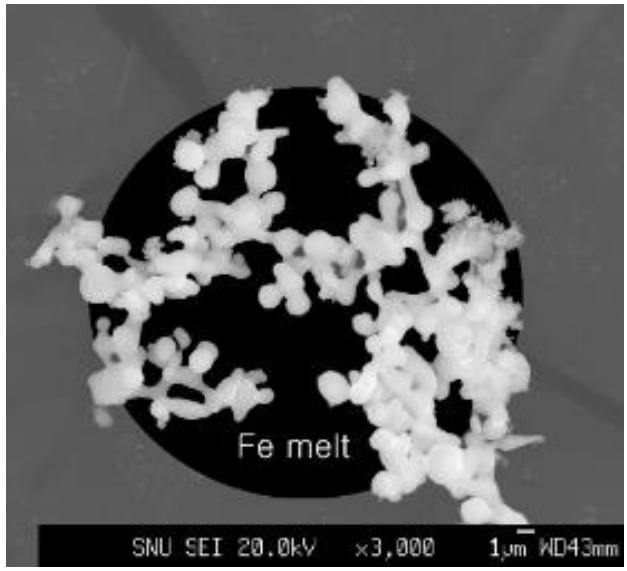


**Fig. 3-11.** Alumina cluster in molten steel [87].

**Table 3-3**. $G^0$ Values at 1580°C for Ca-Aluminate model

| $G^0$ (J/mol) | Reference |
|---|---|
| $G^0_{Ca}$= -150918.108 | [86] |
| $G^0_{Al}$= -116275.101 | [86] |
| $G^0_{Al2O3}$ = -1974008.777 | [86-88] |
| $G^0_{CaAl12O19}$ = -12726470.68 | [91, 93] |
| $G^0_{CaAl4O7}$ = -4820582.823 | [92, 93] |
| $G^0_{CaAl2O4}$ = -2827069.001 | [92, 93] |
| $G^0_{CaO}$ = -798382.2898 | [92, 93] |

In addition to solid compounds, there exist liquid slag phase in CaO-$Al_2O_3$ system. n the case of liquid slag, the stoichiometric ratio is not determined, and Gibbs energy varies depending on the composition. Accordingly, a modified quasi chemical model [94-97] was used to obtain Gibbs energy data of slag according to the composition. Modified quasi chemical model is a thermodynamic model for calculating Gibbs free energy of a liquid binary solution. Unlike the ideal solution or regular solution, it derives mixing entropy value. It calculates the Gibbs energy of the actual solution by considering the ordering between A-B pairs and its mixing entropy. CaO-Al2O3 pair formation Gibbs energy can be expressed as follows.

$$(\mathrm{CaO}-\mathrm{CaO})+(Al_2O_3-Al_2O_3)=2(\mathrm{CaO}-Al_2O_3);\ \Delta g_{CaO-Al2O3} \quad (3\text{-}23)$$

The Gibbs energy of the solution is given by

$$\mathrm{G}=n_{\mathrm{CaO}}g^0_{\mathrm{CaO}}+n_{\mathrm{Al2O3}}g^0_{\mathrm{Al2O3}}-\mathrm{T}\Delta S^{config}+(n_{CaO-Al2O3}/2)\,\Delta g_{CaO-Al2O3} \quad (3\text{-}24)$$

Where n is number of mole, $g^0$is the molar Gibbs energies of the pure componenets. Configurational entropy of mixing is

$$\Delta S^{config}=-\mathrm{R}(n_{\mathrm{CaO}}\ln X_{\mathrm{CaO}}+n_{\mathrm{Al2O3}}\ln X_{\mathrm{Al2O3}}) \quad (3\text{-}25)$$

Where X is mole fraction. CaO-$Al_2O_3$ pair formation Gibbs energy (J/mol) is experimentally given as follows.

$$\Delta g_{CaO-Al2O3} = \left(-121164 - 353674 Y_{Al2O3}^{4}\right) + \left(-27.196 - 115.060 Y_{Al2O3}^{4}\right) \quad (3\text{-}26)$$

$Y_{Al2O3}$ is coordination equivalent fraction and it's definition is as follows

$$Y_{Al2O3} = Z_{\mathrm{Al2O3}} n_{\mathrm{Al2O3}} / (Z_{\mathrm{Al2O3}} n_{\mathrm{Al2O3}} + Z_{\mathrm{CaO}} n_{\mathrm{CaO}}) \quad (3\text{-}27)$$

Where Z is coordination number. The thermodynamic calculation results are shown in Fig. 3-12. When CaO and $Al_2O_3$ make a solution, strong ordering shows a sudden decrease in entropy at the point where the mole fraction of $Al_2O_3$ is 0.4.

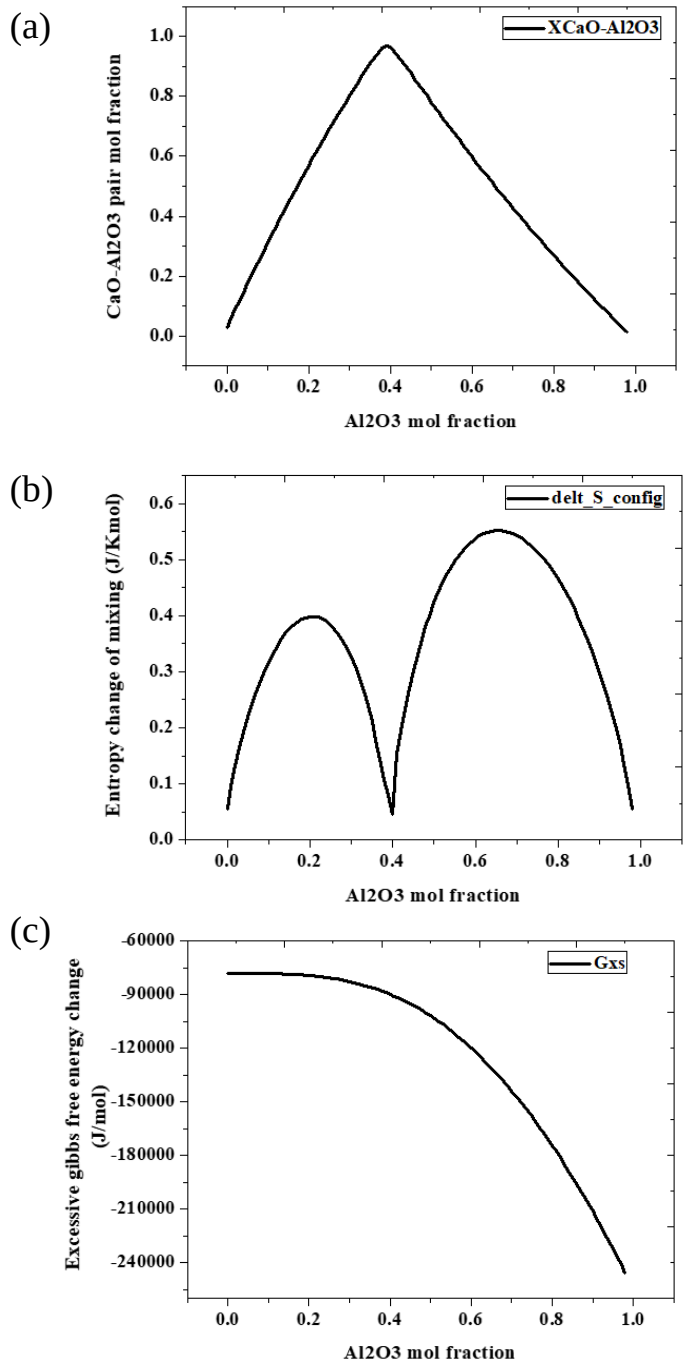


**Fig. 3-12** Thermodynamic calculation of the CaO-Al2O3 binary solution. (a) Pair mol fraction (b) Entropy change of mixing (c) Pair formation Gibbs energy change.

Summarizing the general formula to form calcium aluminate where Ca injected into Al2O3 formed through the primary deoxidation reaction meets,

$$[Ca] + (CaO)_x \cdot (Al_2O_3)_y \rightarrow (CaO)_{x'} \cdot (Al_2O_3)_{y'} \quad (3\text{-}28)$$

Using the Gibbs energy data of solid calcium aluminate in Table 3-3 and the Gibbs energy data of slag previously calculated, the Gibbs energy change of the E.q 3-28 reaction was calculated and shown in fig. 3-13. In the case of solid products, since the composition is fixed, the Gibbs energy change accompanying minxing is determined as one value when the temperature of the system is fixed. For convenience, C3A1, C1A1, C1A2, and C1A6 were named. 'C' stands for CaO and 'A' stands for Al2O3 of binary compound. In the case of liquid slag, even when the temperature was fixed, the Gibbs energy change value was dependent on the composition, so a parabolic graph was obtained according to the composition.

At the point of the solid calcium aluminate product, a two-phase region was expressed by drawing a tangent to the parabolic. In the case of C3A1, since Gibbs energy is higher than when it is present in two phases of CaO and slag, it can be confirmed that a phase cannot be formed at any composition under 1580 °C. Thermodynamic commercial code Factsage 6.4 was used to show the phase diagram of CaO-Al2O3 and compare it with the mixing Gibbs energy change curve above, confirming that the composition at the contact point creating the abnormal region is very well matched.

The number of calcium aluminate reactions must be finitely defined in order to combine flow simulation and complex calcium aluminate reactions. In the case of liquid slag, since the Gibbs energy value varies depending on the

composition, a composition that can represent the slag phase and a Gibbs energy value were selected. The slag phase that forms the equilibrium phase with C1A1 is called'SLAG1', and the slag phase that forms the equilibrium phase with CaO is called'SlAG2'. That is, a 2 point approxiation was used to express the liquid slag phase in a finite reaction equation as stable phases. The composition of ‘SLAG1’ was defined as 0.4537 Al2O3-0.5463 CaO (mole fraction), the Gibbs energy chage of that composition was -27364 J/mol. The composition of ‘SLAG2’ was defined as 0.2893 Al2O3-0.7107 CaO, and the Gibbs energy change of that composition was -21262 J /mol.

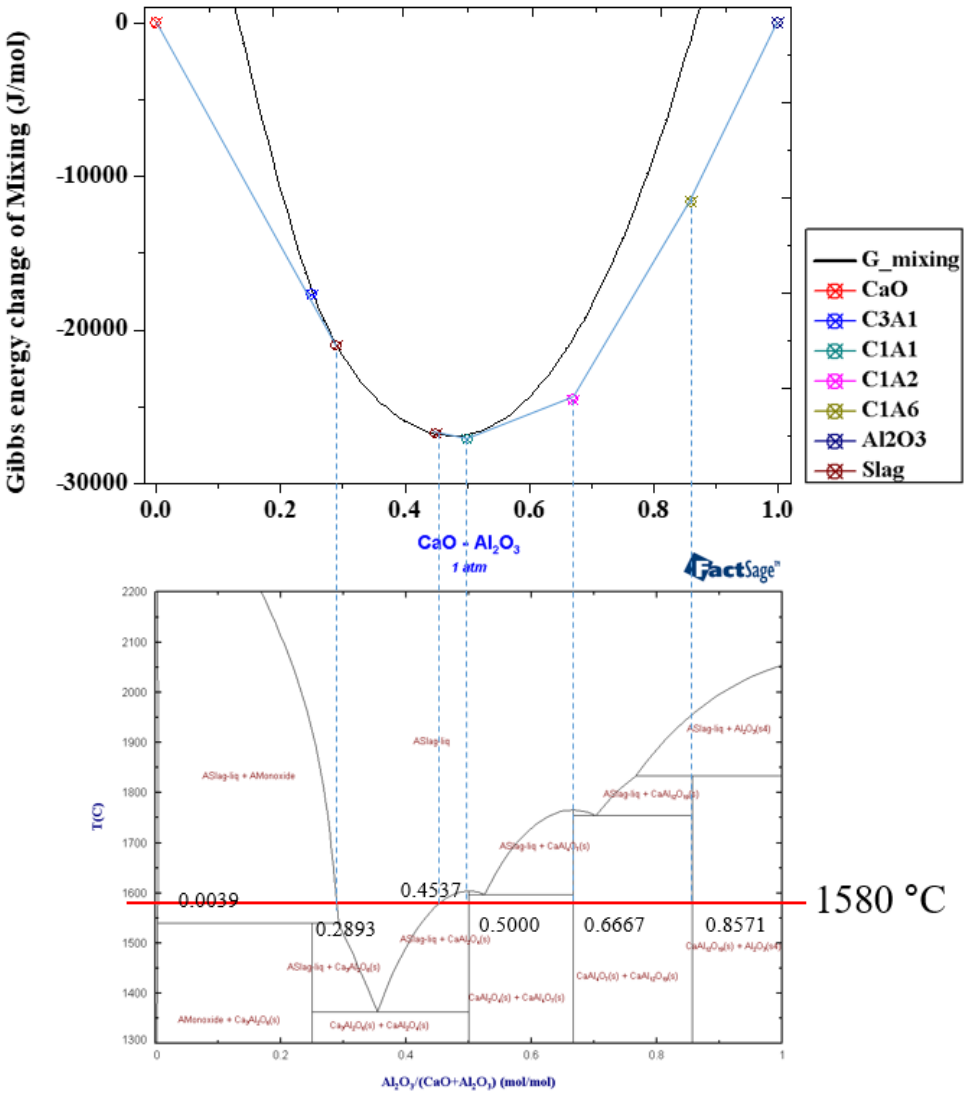


**Fig. 3-13.** Gibbs free energy chage of mixing and CaO-$Al_2O_3$ binary phase diagram.

Depending on which reactant calcium is reacted with, the reaction can be largely divided into six types, and even if the same reactants are met, a total of 21 reactions are carried out by further subdividing different products that can be generated as a result of the reaction. At this time, x1=0.4817, x2=0.2879, y = ($Al_2O_3$) / (CaO) ratio in compound = x/(1-x).

1) Ca + Al2O3 = Ca-Aluminate + Al

Ca + 19/3 $Al_2O_3$ = C1A6+ 2/3 Al

Ca + 7/3 $Al_2O_3$ = C1A2+ 2/3 Al

Ca + 4/3 $Al_2O_3$ = C1A1+ 2/3 Al

Ca + (1/3+$y_1$) $Al_2O_3$ = SLAG1+ 2/3 Al

Ca + 1/3 $Al_2O_3$ = CaO + 2/3 Al (3-29)

2) Ca + C1A6 = Ca-Aluminate + Al

Ca + 7/12 C1A6 = 19/12 C1A2 + 2/3 Al

Ca + 4/15 C1A6 = 19/15 C1A1 + 2/3 Al

Ca + (3$y_1$+1)/(-3$y_1$+18) C1A6 = 19/(-3$y_1$+18) SLAG1+ 2/3Al

Ca + (3$y_2$+1)/(-3$y_2$+18) C1A6 = 19/(-3$y_2$+18) SLAG2+ 2/3Al

Ca + 1/18 C1A6 = 19/18 CaO + 2/3 Al (3-30)

3) Ca + C1A2= Ca-Aluminate + Al

Ca + 4/3 C1A2 = 7/3 C1A1 + 2/3 Al

Ca + (3$y_1$+1)/(-3$y_1$+6) C1A2 = 7/(-3$y_1$+6) SLAG1+ 2/3 Al

$Ca + (3y_2+1)/(-3y_2+6)\ C1A2 = 7/(-3y_2+6)\ SLAG2 + 2/3\ Al$

$Ca + 1/6\ C1A2 = 7/6\ CaO + 2/3\ Al$ (3-31)

4. $Ca + C1A1 = Ca\text{-}Aluminate + Al$

$Ca + (3y_1+1)/(-3y_1+3)\ C1A1 = 4/(-3y_1+3)\ SLAG1 + 2/3\ Al$

$Ca + (3y_2+1)/(-3y_2+3)\ C1A1 = 4/(-3y_2+3)\ SLAG2 + 2/3\ Al$

$Ca + 1/3\ C1A1 = 4/3\ CaO + 2/3\ Al$ (3-32)

5) $Ca + SLAG1 = Ca\text{-}Aluminate + Al$

$Ca + (3y_2+1)/(3y_1-3y_2)\ SLAG1 = (3y_1+1)/(3y_1-3y_2)\ SLAG2 + 2/3\ Al$

$Ca + 1/3y_1\ SLAG1 = (3y_1+1)/3y_1\ CaO + 2/3\ Al$ (3-33)

6) $Ca + SLAG2 = Ca\text{-}Aluminate + Al$

$Ca + 1/3y_2\ SLAG2 = (3y_2+1)/3y_2\ CaO + 2/3\ Al$ (3-34)

After solving the species transport along the flow, the reaction quantity and the equilibrium constant of each species present in the cell are compared to determine whether the reaction will occur in the reverse or reverse reaction. Afterwards, Gibbs free energy change among the reactions that would occur in the forward direction was ordered with a large absolute value. Calculation of calcium aluminate reaction over time was repeated by updating the concentration information of the reactants and products after the reaction and solving the speices transport according to the flow again at every time steop.

### 3.3.2 Kinetics of Ca-$Al_2O_3$ reaction

In the case of primary deoxidation reaction where dissolved oxygen and added Al meet in molten steel to form Al2O3, it is a reaction between mutually dissolved solutes, so the reaction rate is very fast. However, in calcium aluminate reation, the $Al_2O_3$ formed earlier should act as a reaction site, and thus is different from the previous reaction mechanism. Levenspiel et al. proposed an unreacted core model to explain the reaction mechanism of particles in a fluid [98]. As shown in Figure 3-14, Ca (reactant A) reacts with the unreacted core (reactant B, $Al_2O_3$ or calucium aluminate) on a solid surface to form a product, and a product layer accumulates outside the core. The accompanying mechanisms are as follows.

(1) Diffusion of gaseous reactant A through the fluid film surrounding the particle to the surface of the solid.
(2) Penetration and diffusion of A through the blanket of ash to the surface of the unreacted core.
(3) Reaction of gaseous A with solid at this reaction surface.
(4) Diffusion of gaseous products through the ash back to the exterior surface of the solid.
(5) Diffusion of gaseous products through the gas film back into the main body of fluid.

Yo-ich et at. confirmed the Ca diffusion through calcium aluminate product as a reaction rate controlling step by measuring the evolution of CaO over time by adding CaSi wire to 20 kg of molten steel [99].

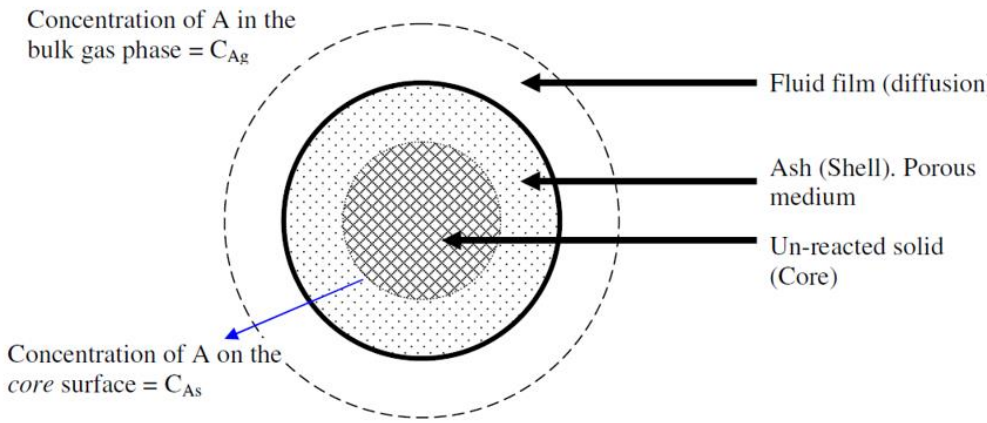


**Fig. 3-14.** Unreacted core model for simulating calcium aluminate reaction kinetics [98].

If Ca diffusion into the product layer is the reaction rate controlling step, it can be said that the total amount diffused into particles is equal to the total amout of a reactiong on the core surface and at any intermediate location. At this time, the core calucium aluminate reactant can be expressed as follows.

$$-\frac{dN_{Ca}}{dt} = D_e \frac{\partial C_{Ca}}{\partial t} 4\pi r^2 = \text{constant} \quad (3\text{-}35)$$

$D_e$ is effective diffusion coefficient and $r$ is radius of product layer. Since the reaction rate on the surface and the Ca diffusion rate from the bulk to the layer surface are much faster than the diffusion rate on the layer, the Ca concentration on the reactant surface can be called approximately zero, and the Ca concentration on the produt layer surface is equal to the Ca concentration of bulk. Accordingly, the reaction rate of Core calcium aluminate B is as follows.

$$-\frac{dN_B}{dt} = \frac{4\pi D_e C_{Ca}}{\frac{1}{r_c} - \frac{1}{R}} = \rho_B 4\pi {r_c}^2 \frac{dr_c}{dt} \quad (3\text{-}36)$$

Since $r_c$ decreases gradually as the reaction continues, When Eq. 3-36 is integrated from t = 0 to t = t and r = $r_c$ to r = $R$, the following relation between reaction time and core reactant radius can be obtained as

$$t = \frac{\rho_B R^2}{6 D_e C_{Ca}} \left(1 - 3\left(\frac{r_c}{R}\right)^2 + 2\left(\frac{r_c}{R}\right)^3\right) \quad (3\text{-}37)$$

Therefore, the reaction completion time τ where all of the core reactatnt reacts to $r_c$=0 is as follows.

$$\tau = \frac{\rho_B R^2}{6 D_e C_{Ca}} \tag{3-38}$$

$$\frac{t}{\tau} = \left(1 - 3\left(\frac{r_c}{R}\right)^2 + 2\left(\frac{r_c}{R}\right)^3\right) \tag{3-39}$$

As shown in Fig. 3-15, the volume fraction of the reacted value for time t can be defined from the volume of the reactant before the reaction and the volume of the reactant after the reaction.

$$X_B = 1 - \left(\frac{r_c}{R}\right)^3 \tag{3-40}$$

$$\frac{t}{\tau} = 1 - 3(1 - X_B)^{2/3} + 2(1 - X_B) \tag{3-41}$$

Calculate the reaction completion time τ in Eq. 3-38 and substitute the time step in the process to Eq. 3- 41 gives $X_B$ value which is the reaction ratio considering the size of the reactant and the concentration of Ca. In the case of liquid calcium aluminate, the diffusivity of Ca is significantly faster than through the of solid calcium aluminates. Lind et al. conducted experiments using CaO and Al2O3 cylinder blocks to evaluate reaction rate of the liquid calcium aluminate phase [100, 101]. The diffusion coefficient was derived through the thickness of the liquid slag calcium aluminate that evolved over time. The diffusion coefficients measured at 1550°C and 1600°C were interpolated to use $6.8\times10^{-9}$ $m^2/s$ values. The effective diffusion coefficient of Ca in the solid phase was assumed to be 1/100 of the liquid phase, $6.8\times10^{-11}$ $m^2/s$.

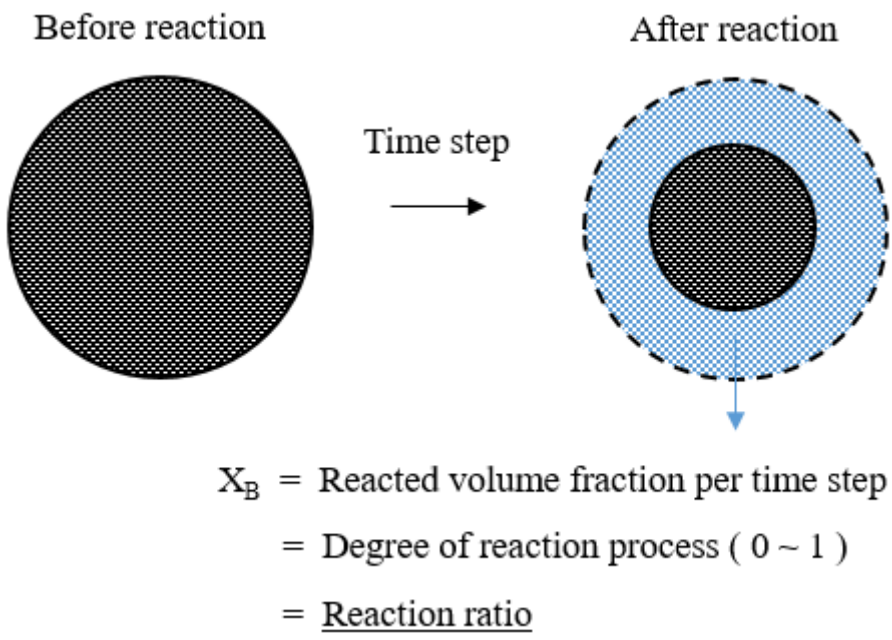


**Fig. 3-15.** Reaction ratio calculation using reacted volume fraction.

### 3.3.3 Result and discussion

Fig. 3-16 shows the results of calucium aluminate reaction with alumina generated by adding 400 ppm of Ca after primary refining by adding 300 ppm of dissolved oxygen and 500 ppm of Al. In the initial stage of Ca injection, 623.27 ppm of Al2O3 meet and react with each other. It can be observed that various allotropes are formed simultaneously with rapid consumption of Al2O3. It can be seen that the amount generated at the same time is different depending on the phase. C1A6, C1A2, C1A1, and SLAG1 gradually decompose after generation and eventually disappear. CaO is rapidly formed in the early stages, gradually decomposed, and gradually saturated at an equilibrium concentration. In the case of SLAG2, from the beginning to the end of the reaction, the amount continues to increase and the equilibrium value is reached without decreasing the concentration. It takes a little more time to homogenize all the circulation points, but eventually homogenizes at equilibrium values at all positions.

As shown in Fig. 3-17, the evolutionary behavior of each phase over time can be observed in more detail with cell averaged concentration. At the beginning of the reaction, the formation of the CaO phase is the main one, and it is expected to reach equilibrium by forming to about 350 ppm and then gradually decomposing to 140.54 ppm. The formation of SLAG1 and SLAG2, which are liquid phases, stands out next. Solid calcium aluminates such as C1A6, C1A2, and C1A1 are also formed simultaneously, but it can be seen that the amount is very small compared to other phases. The C1A6, C1A2, and C1A1 phases all tend to have a forward reaction with Ca, but the amount of formation is very small because their diffusivity is very low. Although the CaO phase is also a solid phase, it seems that a large amount can be generated, because, the SLAG1 and SLAG2 phases are

excessively generated at early stage of the reaction and they are used again for CaO generation. After the initial reaction, the unstable phases gradually decompose and disappear, and the CaO formed in excess also decomposes until its concentration reached the equilibrium value. Using the thermodynamic commercial code Factsage 6.4, calculating the equilibrium phase and the equilibrium concentration formed by 500ppm Al – 300ppm O – 400ppm Ca is expected to result in slag phase 693.92ppm and CaO 149.79ppm. Compared with the results of this study, the predicted equilibrium type is consistent. Although there is an error of around 10 ppm in the amount of the equilibrium phase, considering that the Gibbs energy data are different and the reaction involved is very complex, it is judged to be sufficient to prove the reliability of the model.

The result of calculation with 500ppm Al-300ppm O-150ppm Ca is shown in Figure 3-18. The equilibrium phases expected for this composition are C1A2 and C1A1. It can be confirmed that the equilibrium concentration was not reached for the same time, unlike when 500 ppm of Ca case. In the early and middle stage of the reaction, the rapidly formed SLAG1, SLAG2, and CaO are decomposed into C1A2 and C1A1 at a relatively high rate, but at the end of the reaction, the reaction equilibrium is reached only by the interaction between C1A2 and C1A1. The rate at which the solid phase decomposes and is produced has a very slow rate, unlike when the liquid phase is involved, so it takes a considerable long process time to reach equilibrium. Considering that the ladle operation time is around 30 minutes, it is expected that the equilibrium will not be reached until the conventional operation time. In the actual process, redoxidation may occur due to the oxygen input from the plume eye, which is not considered in the current model, and more residual Al may react after the primary deoxidation process to create more Al2O3

inclusion. Accordingly, even when the amount of Ca expected to form a liquid slag phase is introduced, a case in which the solid phase becomes a stable phase may occur as shown in Fig.3-18. The decrease in dissolved yield due to the vaporization of Ca also increases the possibility of creating this phenomenon. In addition, because the slag at the top of the ladle removes $Al_2O_3$ inclusion by floating separation, the phenomenon becomes more complicated. Therefore, in order to develop a more accurate predictive model, future studies need additional consideration for the aforementioned phenomena.

(a)

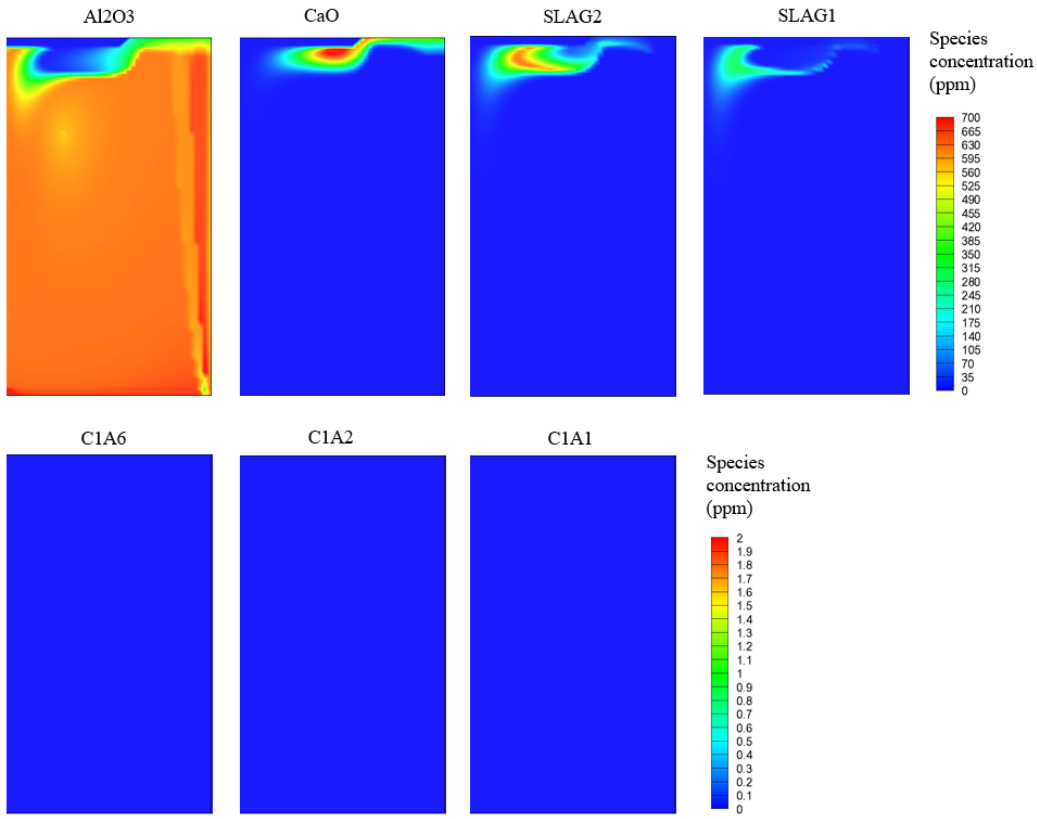
Al2O3
CaO
SLAG2
SLAG1
Species concentration (ppm)
700
665
630
595
560
525
490
455
420
385
350
315
280
245
210
175
140
105
70
35
0
C1A6
C1A2
C1A1
Species concentration (ppm)
2
1.9
1.8
1.7
1.6
1.5
1.4
1.3
1.2
1.1
1
0.9
0.8
0.7
0.6
0.5
0.4
0.3
0.2
0.1
0

(b)

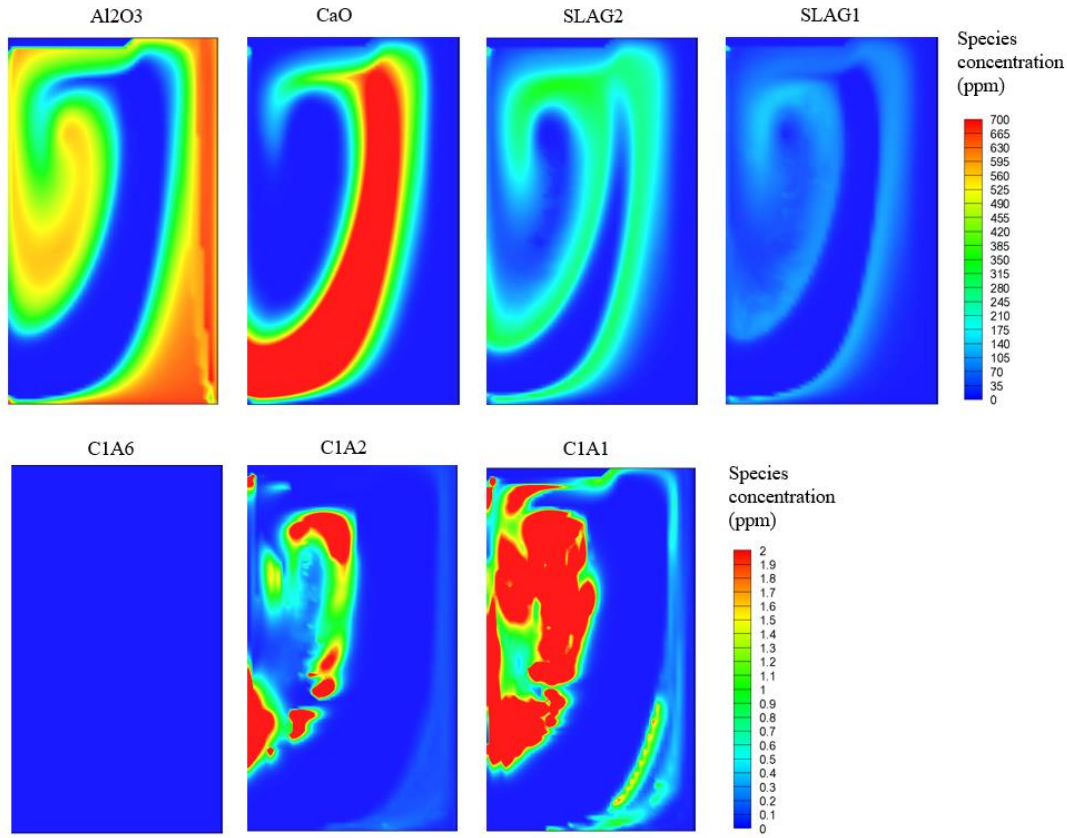
Al2O3
CaO
SLAG2
SLAG1
Species concentration (ppm)
700
665
630
595
560
525
490
455
420
385
350
315
280
245
210
175
140
105
70
35
0
C1A6
C1A2
C1A1
Species concentration (ppm)
2
1.9
1.8
1.7
1.6
1.5
1.4
1.3
1.2
1.1
1
0.9
0.8
0.7
0.6
0.5
0.4
0.3
0.2
0.1
0

(c)

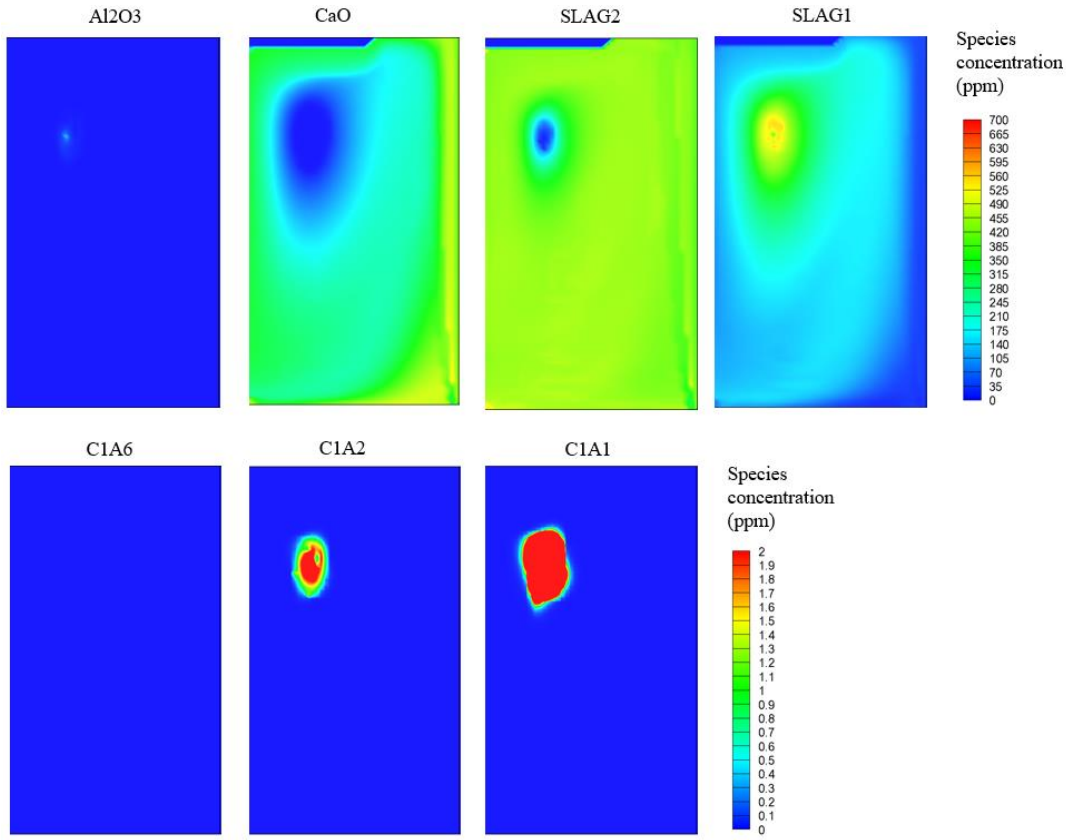
Al2O3
CaO
SLAG2
SLAG1
Species concentration (ppm)
700
665
630
595
560
525
490
455
420
385
350
315
280
245
210
175
140
105
70
35
0
C1A6
C1A2
C1A1
Species concentration (ppm)
2
1.9
1.8
1.7
1.6
1.5
1.4
1.3
1.2
1.1
1
0.9
0.8
0.7
0.6
0.5
0.4
0.3
0.2
0.1
0

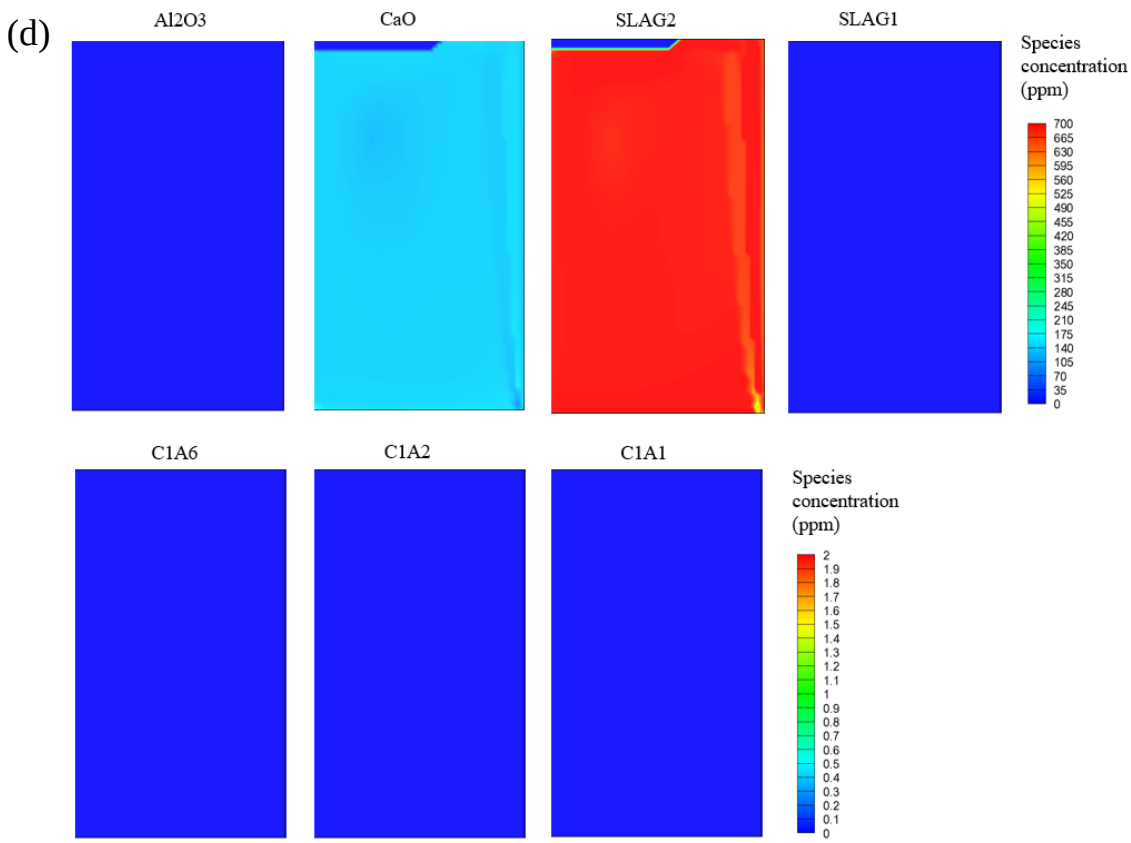


**Fig. 3-16.** Simulation result of 500ppm [Al] – 300ppm [O] – 400ppm [Ca] reaction in melt. Calcium aluminate products distribution according to the process time. (a) 2 sec after Ca injection (b) 50 sec after Ca injection (c) 200 sec after Ca injection (d) 800 sec after Ca injection

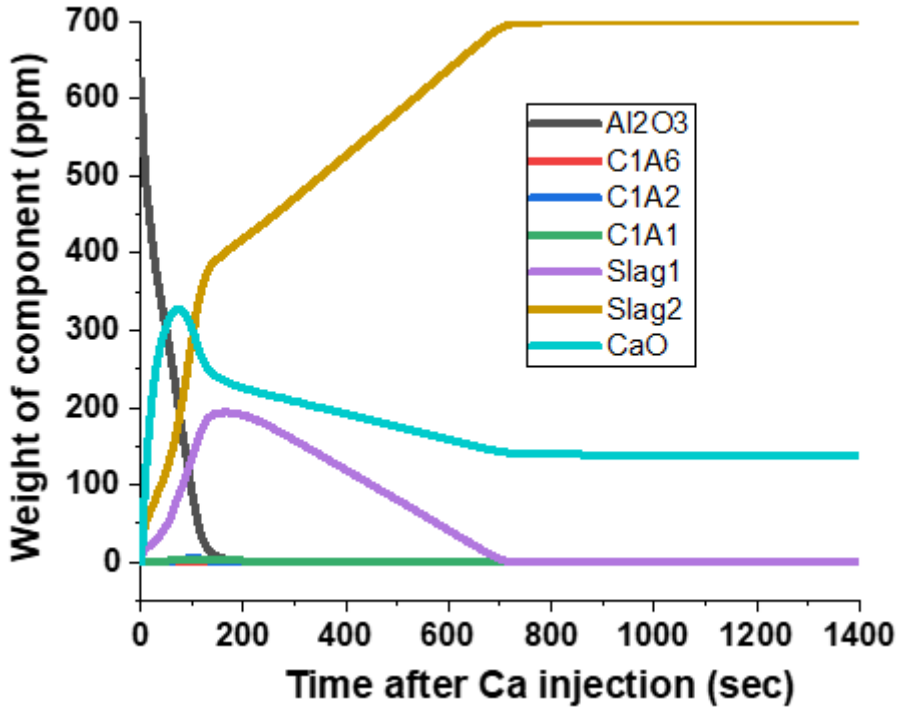


**Fig. 3-17.** 500ppm [Al] – 300ppm [O] – 400ppm [Ca] reaction result. Cell averaged concentration of the species in deoxidation reaction.

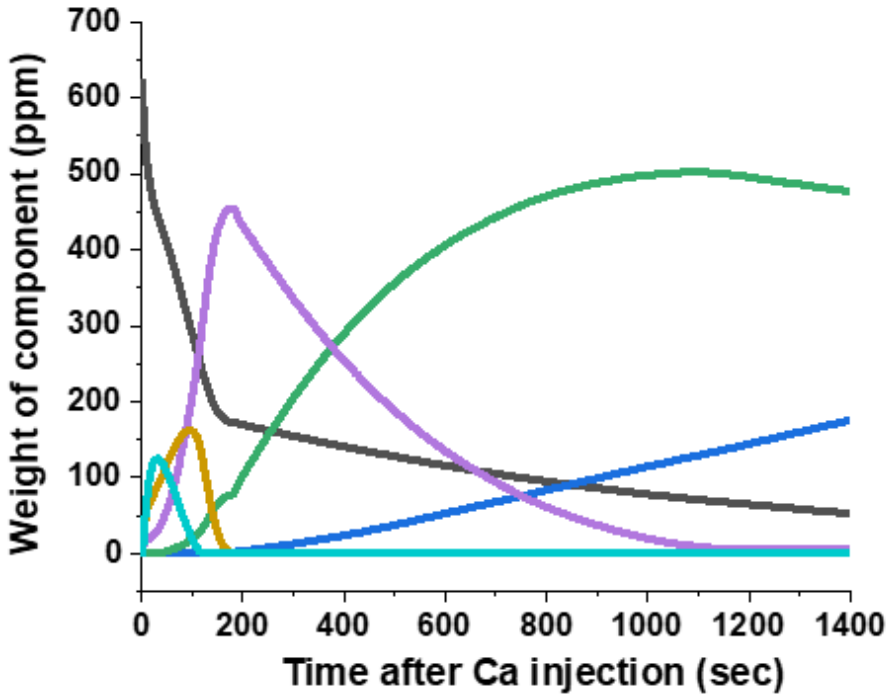


**Fig. 3-18.** 500ppm [Al] – 300ppm [O] – 150ppm [Ca] reaction result. Cell averaged concentration of the species in deoxidation reaction.

# Chapter 4. Inclusion control in continuous casting mold

## 4.1 Model for analyzing SEN port angle effect on flow stability

We performed numerical calculations using the commercial computational fluid dynamics software Fluent 15 [102] with the same conditions used in the water model experiments. As shown in Fig. 4-1 (a), a half-domain was calculated, and a grid system with 600,000 hexagonal grids was constructed for use in the calculations.

For the simulation, Mass and momentum balance equation was calculated with realizable *k*–ε model. The face of the circular tube connecting the tundish and mold interior was designated as the inlet with a constant velocity of 0.9158 m/s. *k* and ε were calculated at the inlet using Eq. (11) [103, 104]. The *I* of 0.05 indicates the intensity of turbulence, and the hydraulic diameter was 40 mm.

$$\mathrm{k} = \frac{3}{2}\left(U_{inlet}\, I\right)^2, \quad \varepsilon = C_\mu^{3/4} \frac{k^{3/2}}{0.07 D_H} \quad (C_\mu = 0.09) \tag{4-1}$$

The standard wall function was applied to the mold wall with a non-slip condition. The chamber floor was designated as an outlet with a constant gauge pressure of zero. The asymptotic calculation results produced after 20,000 iterations were taken as the initial conditions for the subsequent calculations. The transient calculations were performed with a time step of 0.01 s for 400 s. A criterion for convergence was set to $1 \times 10^{-3}$ of residual on all variables of governing equations and the calculation was iterated at each time step until the convergence criterion was met.

The discrete phase model (DPM) based on the Euler-Lagrange approach

was used to calculate the influence of the secondary phase (gas) on the primary phase (water). The two-way coupling method was used to reflect the bi-directional interaction between two phases. We set the gas bubble size uniformly to 1 mm [105, 106]. In order to simulate the continuous escape of gas particles, an escape condition was adopted at the top surface and outlet. Transient calculations of the DPM model were performed with a time step of 0.002 s. The detailed conditions are presented in Table 4-1 and 4-2.

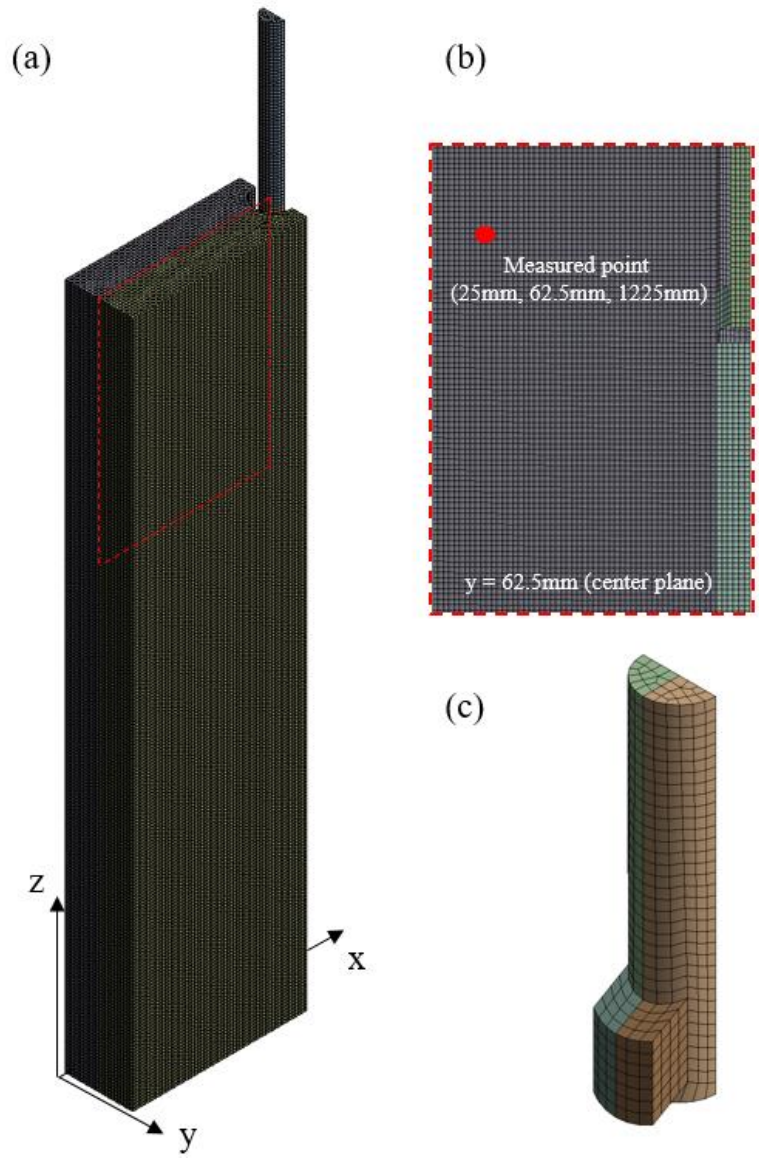


**Fig. 4-1.** Simulation domain and mesh: (a) Entire domain with upper section of the center plane (Red dash line, y=62.5mm) (b) Front view of the center plane (y=62.5mm) and measured point (25 mm, 62.5 mm, 1225 mm). (c) Submerged entry nozzle (SEN).

**Table 4-1.** Geometrical parameters.

| Parameters | Values |
|---|---|
| SEN length (mm) | 500 |
| SEN bore diameter (mm) | 40 |
| SEN submerged depth (mm) | 150 |
| SEN bottom well depth (mm) | 5 |
| Port width / height (mm) | 32.5 / 40 |
| Port thickness (mm) | 15 |
| Port angle (°) | 0, 5, 10, 15, 20, 25, 30, 35 |
| Mold height / width / thickness (m) | 1.275 / 0.65 / 0.125 |

**Table 4-2.** Material properties and process parameters.

| Parameters | Values |
|---|---|
| Fluid density ($kg/m^3$) | 998.2 |
| Fluid viscosity (kg/m·s) | $1.003 \times 10^{-3}$ |
| Nitrogen gas density ($kg/m^3$) | 1.251 |
| Nitrogen gas flow rate (SPLM) | 0, 2 |
| Nitrogen gas bubble diameter (mm) | 1 |
| Casting speed (m/min) | 0.85 |

## 4.2 Result and discussion

### 4.2.1 Velocity variation at monitoring point

Fig. 4-2(a) is the raw data of PIV measurement in the water model experiment at the measurement point (25 mm, 62.5 mm, 1225 mm). Measured velocities for a period of 400 second showed strong fluctuations. This fluctuation pattern was significantly different, in both the number and magnitude of peaks, from those obtained from the numerical simulation, as shown in Fig. 4-4. The experimental results contained high-frequency oscillations. The reason for this difference is that the k-ε turbulent model based on the Reynolds-averaged method transforms high-frequency fluctuation behaviors into the turbulent parameters k and ε; therefore, the simulation only captures the relatively long-term variations associated with the large structure. Because the high-frequency fluctuations caused by turbulent flow are not the target of the present study, the experimental data were processed with a 0.1 Hz low-pass filter [104], as shown in Fig. 4-2(b). The filtered data seem to be comparable to the data of the numerical simulation, and all subsequent experimental data were processed with a 0.1 Hz low-pass filter. Figure 4-3, 4-4 compares variations in magnitude of the velocity at the monitoring point for eight SEN port angles for the experimental and numerical simulation results. The overall trends in the experimental results (Fig. 4-3) are similar to those predicted by the numerical simulations (Fig. 4-4).

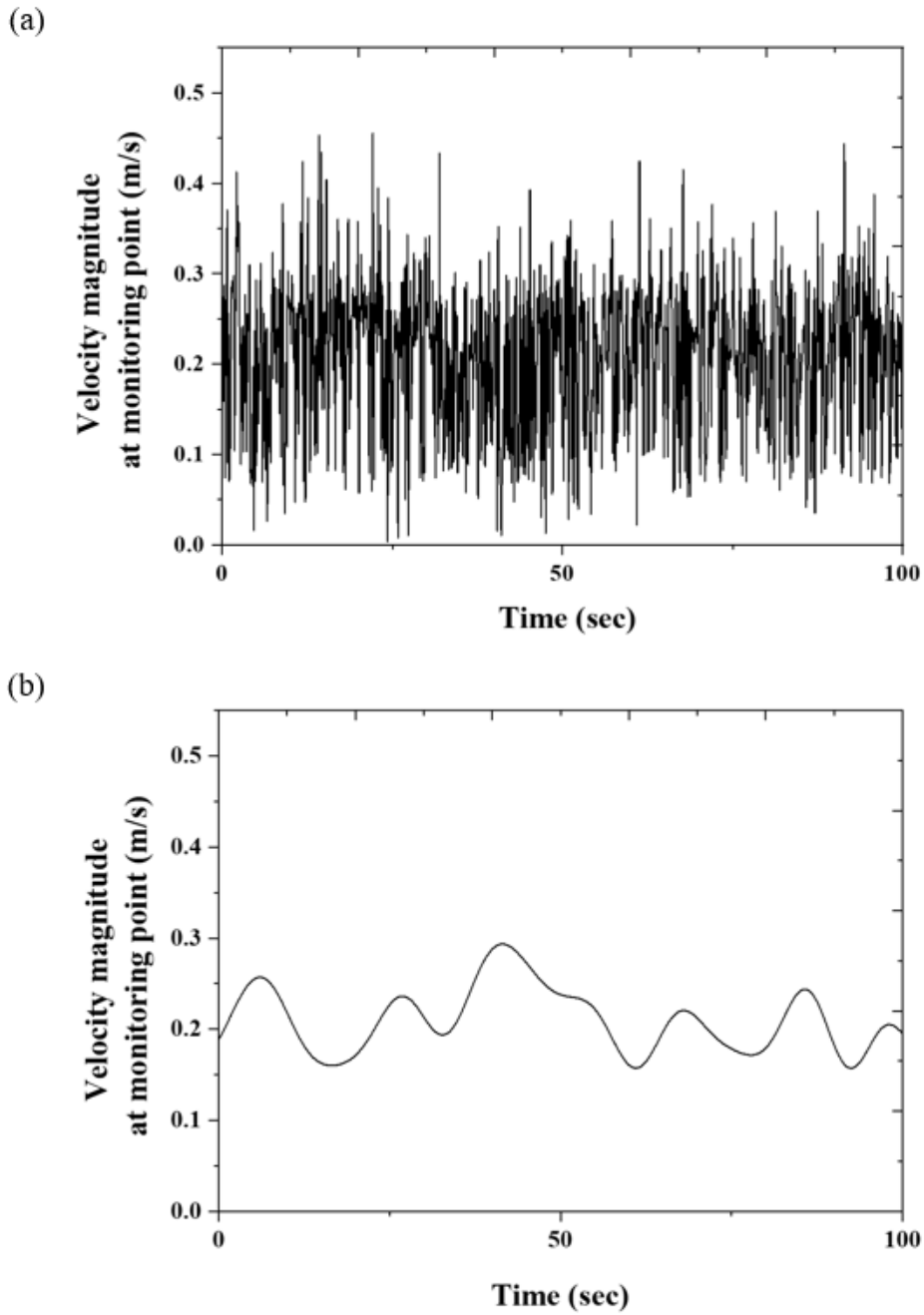


**Fig. 4-2.** Water model experiment results. Velocity variation versus time at monitoring point for port angle of 0° (up to 100 s). (a) Raw experimental result; (b) experimental 0.1 Hz low-pass filtered result.

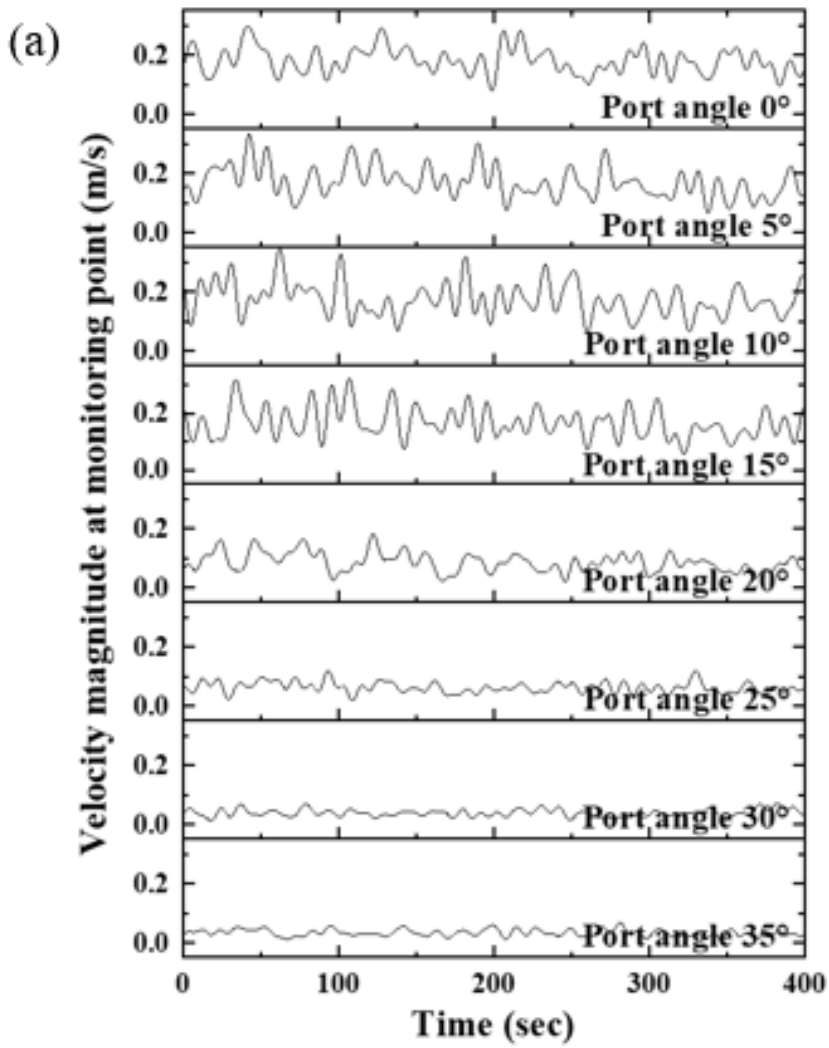


**Fig. 4-3.** Experimental results without gas injection. Velocity variation versus time at monitoring point for various port angles (up to 400 s).

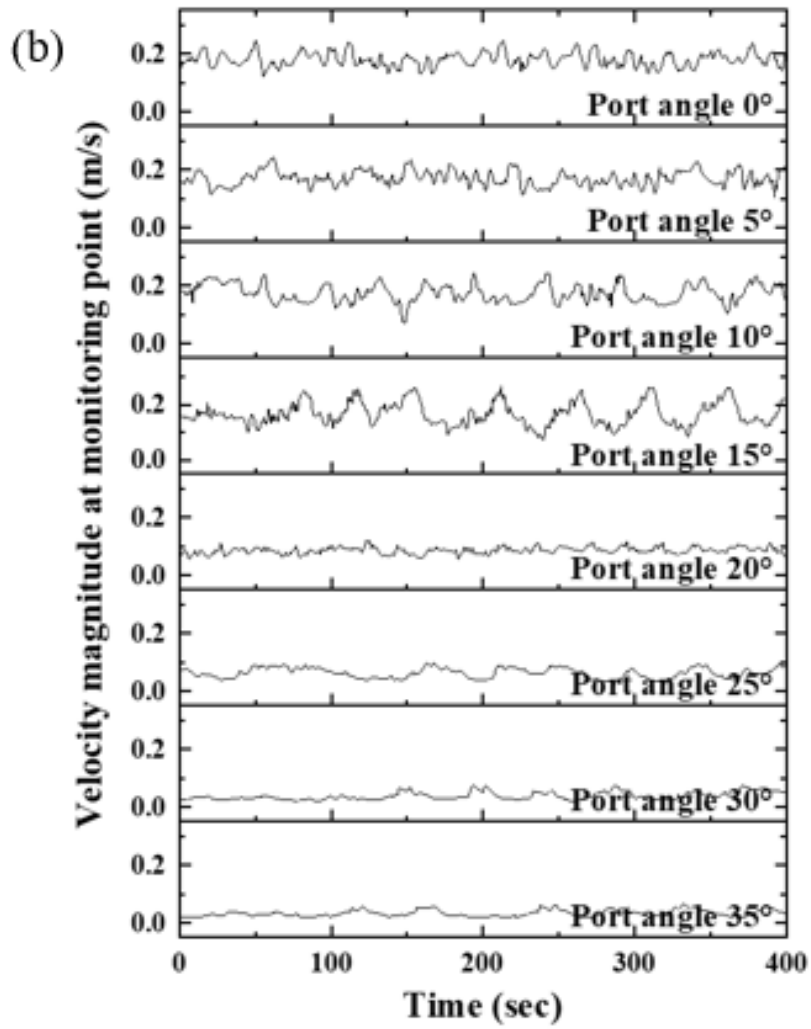


**Fig. 4-4.** Numerical results without gas injection. Velocity variation versus time at monitoring point for various port angles (up to 400 s).

As shown in Fig. 4-3 and 4-4, the velocities show different behaviors at low and high angle regions. First, the average velocity magnitudes for 0–15° port angles were larger than those for 20–35° port angles. Secondly, the fluctuation magnitudes were also different. The 0–15° port angles exhibited larger velocity fluctuations than the 20–35° ones. Based on these differences, the two velocity regimes were designated as region 1 (0–15° port angles), in which the velocity behavior is unstable, and region 2 (20–35° port angles) in which the velocity behavior is more stable.

The average velocity magnitudes and standard deviations at the monitoring points are plotted against the port angle in Fig. 4-5. The average experimental velocity magnitudes in region 1 were 0.1535–0.2105 m/s, while those in region 2 were 0.0395–0.1061 m/s. Standard deviations in regions 1 and 2 were 0.0331–0.0381 m/s and 0.0145–0.0151 m/s, respectively. The simulation results also showed the sudden transition observed in the experiments. The average velocity magnitudes in regions 1 and 2 were 0.1671–0.1805 and 0.0335–0.0861 m/s, respectively; the standard deviations were 0.0240–0.0342 and 0.0113–0.0132 m/s, respectively.

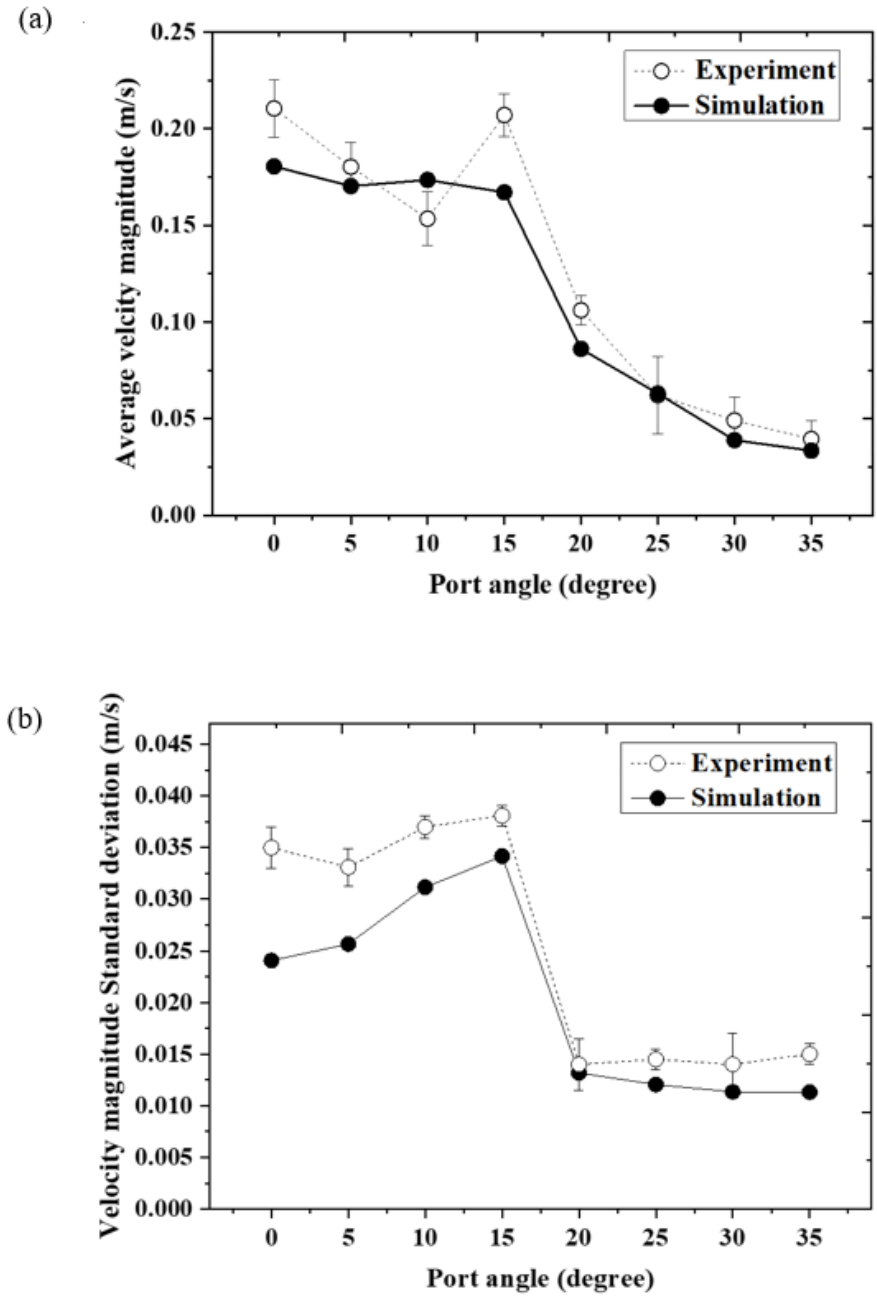


**Fig. 4-5.** (a) Average velocity magnitude at monitoring point without gas injection. (b) Velocity magnitude standard deviation at monitoring point without gas injection.

### 4.2.2 Flow pattern prediction

Figure 4-6 shows the predicted flow patterns of different port angles as a function of time. At a port angle of 15°, as shown in Fig. 4-6(a), the vertical swinging of the water jet injected through the SEN outlet appears with large velocity changes in the upper circulation zone. When flow was directed towards the upper side, as shown in the first and third contours of Fig. 4-6(a), majority of the fluid injected from the SEN moved up to the free surface. Meanwhile, when flow was directed towards the lower side, as shown in the second contours of Fig. 4-6(a), only a small amount of the fluid moved up to the free surface. The repetition of this process made the flow phenomena unstable over time and caused the continuously fluctuating behavior. In contrast, in the case of a jet at 35°, shown in Fig. 4-6(b), the water jet was stably directed downward, and the vertical oscillation of the jet was very small. From the results of experiments and calculations, the fluctuations of the flow seem to be determined by the flow of the jet discharged from the nozzle, as shown in Fig. 4-6. Accordingly, the movement of the jet was analyzed in more detail.

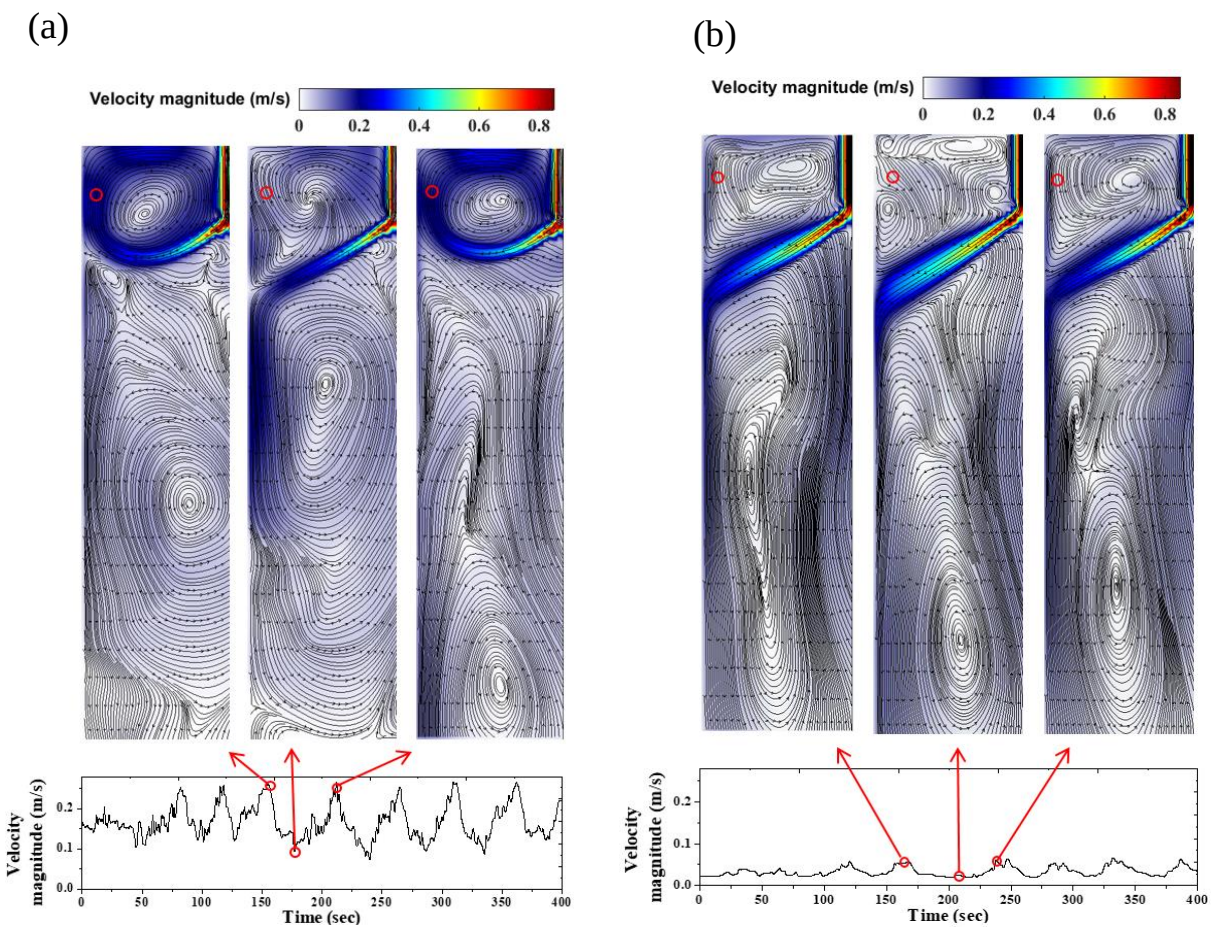


**Fig. 4-6.** Predicted velocity magnitude versus time curves at the monitoring point without gas injection. Snapshot images of the velocity distribution on the center plane. The streamlines with small arrows in each panel represent the velocity components of the fluid. The red open circles of each contour indicate the monitoring point. Port angle of (a) 15° and (b) 35°.

### 4.2.3 Jet angle analysis

Fig. 4-7 shows the predicted time-averaged velocity magnitude contours with vectors of the upper area of the mold over the 400 seconds for the 15° port angle (region 1) and the 35° port angle (region 2). The main flow direction of the water changes continuously over time with vertical swinging of at port angle 15°, as shown in Fig. 4-6(a); however, the time-averaged velocity distribution shows that the flow of the injected water was nearly perpendicular to the wall as it approached the wall opposite of the SEN port (narrow face). On the other hand, at 20, 25, and 35°, which show relatively stable flow patterns, the water jet from the SEN, as it approached narrow face, flowed in a downward direction. The main flow direction does not change even if there exists a slight angular deviation. Therefore, the angle at which the water approaches the wall seems to affect the stability of the flow.

In order to quantitatively analyze the relationship between the oscillations of the jet and the velocity variation in the mold's upper circulation zone, we calculated velocity profiles along a vertical line located 200 mm from the wall ($1/6^{th}$ of the way across the mold), as shown in Fig. 4-8(a). Then, using Eq. 4-2, the jet angle was calculated at the point where the velocity magnitude had its maximum value.

$$\theta = -\tan^{-1}\frac{V_z}{V_x} \tag{4-2}$$

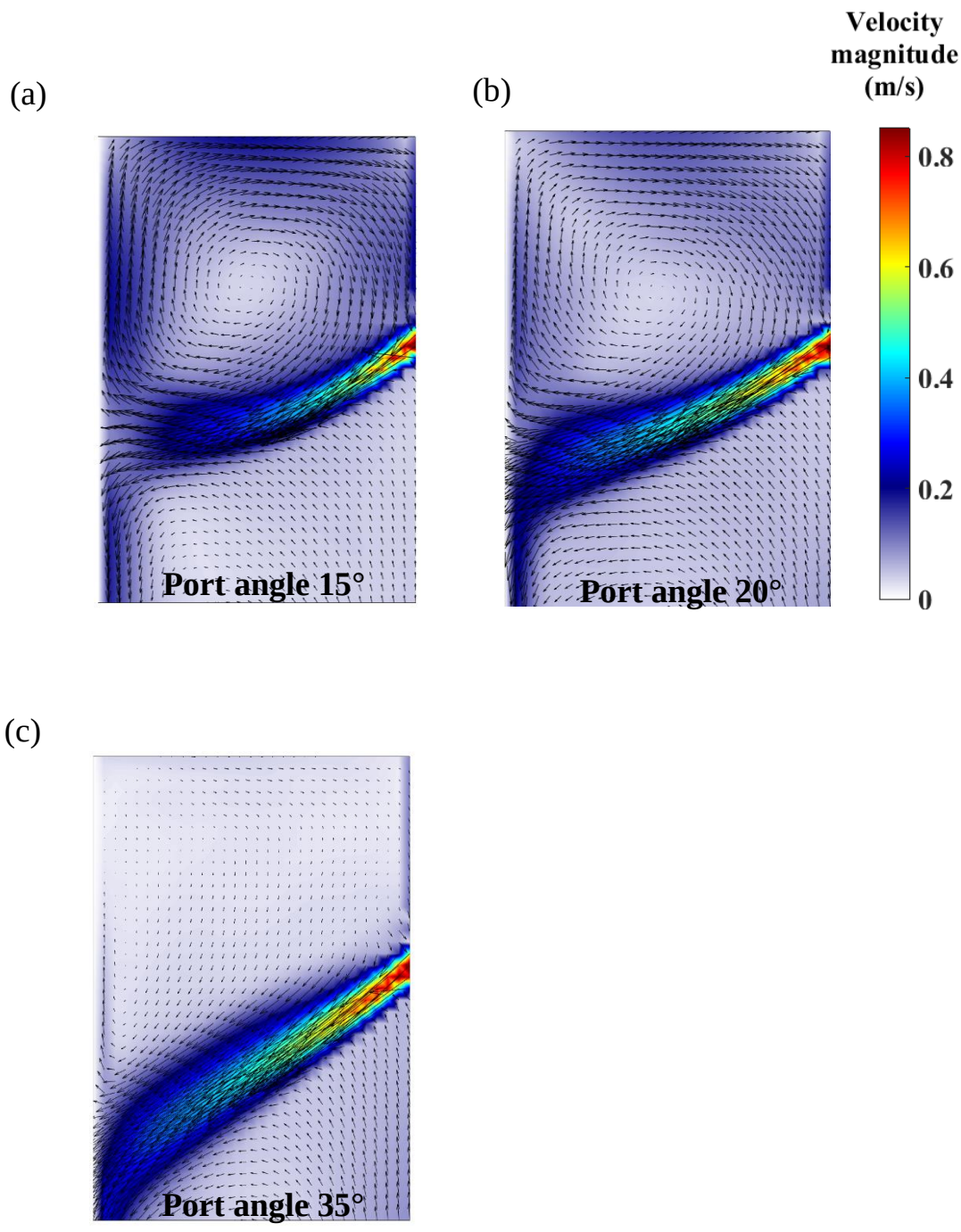


**Fig. 4-7.** Predicted time-averaged velocity plots in the upper region of the mold over 400 s with SEN port angles of (a) 15°, (b) 20°, and (c) 35°.

The changes in the jet angle over time are plotted in Fig. 4-8(b). The trends in the variation of the jet angle were similar to the flow behavior shown in Fig. 4-4 and 4-5. The average values were high, and fluctuations were severe in the unstable flow region. In contrast, the average values were low, and fluctuations were smaller in the stable flow region. The predicted time averaged jet angle value in regions 1 and 2 ranged from −2.48 to 9.71° and −19.86 to −31.95°, respectively (Fig. 4-9). A sudden drop was noticed when the port angle changed from 15 to 20°, as observed in the previous speed analysis. Only a 5° increment in the SEN port angle resulted in a fully downward jet, which was nearly −20°, and this led to stable flow.

It has been reported that high-angle SEN ports generate stable flow on the surface because the jet streams penetrate the mold more deeply, and their linear relationship was studied [56, 60-64]. However, previous studies did not capture these abrupt transition phenomena. The two regions showed significant differences in the magnitude of the jet angle variation. The jet angle oscillated between −41.78 and 41.30° in region 1 and between −36.70 and −11.31° in region 2. Moreover, region 1 and region 2 showed a clear difference in the sign of the peak values of the jet angle during the oscillation. In case of region 1 showing unstable flow characteristics, minimum value was negative and maximum value was positive, while in region 2 which showed stable flow characteristic, both minimum and maximum values were negative.

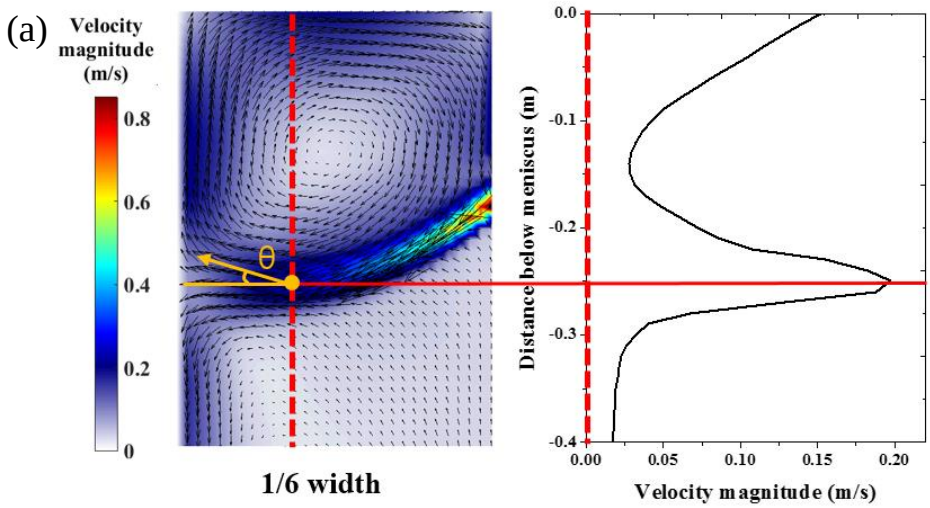


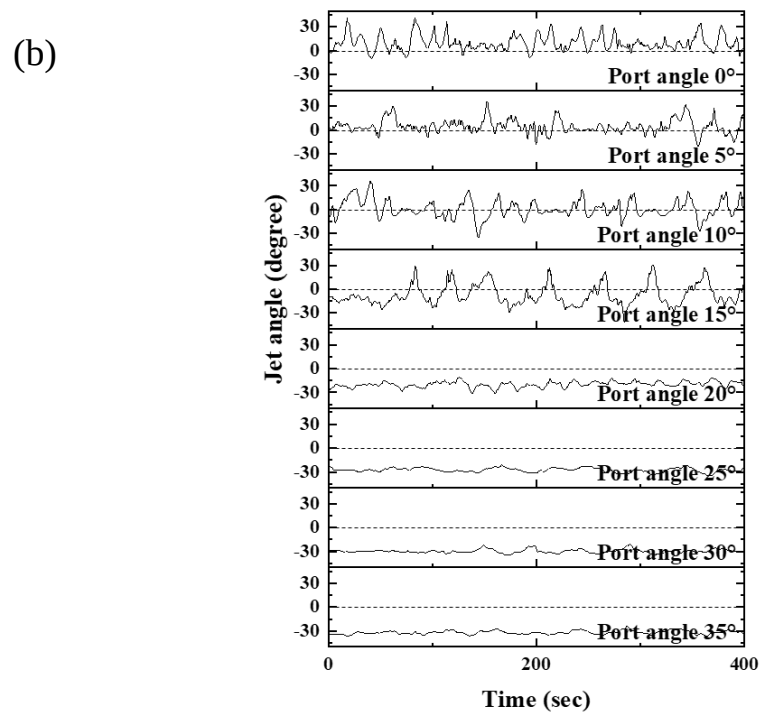


**Fig. 4-8.** Predicted jet angle variation without gas injection. (a) Jet angle definition. (b) Jet angle variation versus time. Dashed line denotes a jet angle of 0°.

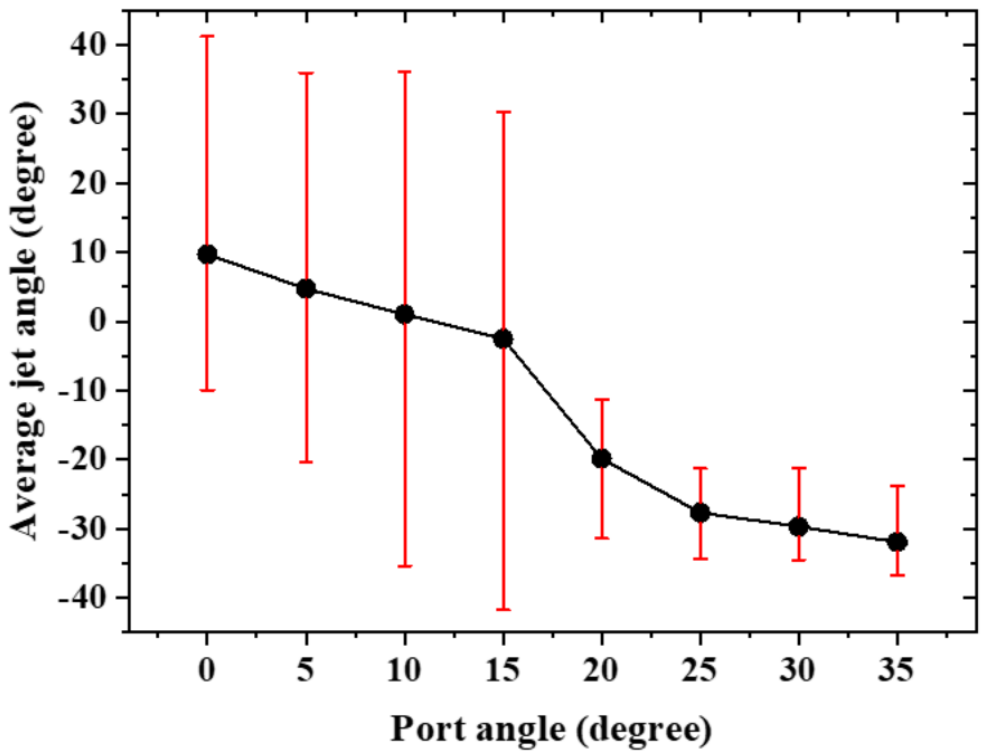


**Fig. 4-9.** Predicted time-averaged jet angle versus port angle. Red bar indicates the jet oscillation range with maximum and minimum values.

Comparing the differences between the 15 and 20° port angles at the boundary between flow stability and instability, the jet oscillated in the range of −41.78 to 30.312° for the 15° port angle and −31.43 to −11.31° for the 20° port angle. For the 15° port angle, the jet angle exceeded 0° periodically during oscillation. After the oscillating jet exceeded 0°, the main flow of the fluid was directed upward, so that a majority of the water entering the mold flows above the input jet. We observed that the jet angle increased steeply to the positive maximum value soon after the jet angle exceeded 0° and then descended steeply to a negative minimum value, as shown in Fig. 4-8(b). This behavior was repeated continuously. For the 20° port angle, the jet also oscillated, but the maximum values remained negative. This means that at no time was the jet directed upwards. In region 1, the effects of the large rise and fall of the jet cancel out each other so that the time-averaged jet angle value shows a significant deviation from the minimum and maximum values; whereas in region 2, the jet direction remained downward, and the variation was small. Based on the jet angle analysis results, whether the jet has a positive jet angle during oscillation is a critical condition that divides stability and instability.

Fast Fourier transform (FFT) analysis of the results for flow at 15° and 35° was performed to quantitatively analyze the relationship between jet angle variation and velocity variation in the upper recirculation zone. The FFT analysis results are shown in Fig. 4-10. The experimentally determined data contained relatively many peaks. Unlike the experimental results, the oscillation peak of the simulation result was clear. From the highest-intensity peak, the variation cycle period could be predicted. Among these peaks, those indicating an oscillation frequency of roughly 0.02 Hz were the most prominent in both the experimental and simulated velocity data. The jet angle and oscillation frequency obtained via simulation were in almost

complete agreement with the velocity variation frequency for both ports. Hence, the jet repeatedly rose and fell with a period of roughly 50 s, and the corresponding velocity in the upper mold region varied with a period of 50 s. As shown earlier, the degree of oscillation at 35° was not large, but minor oscillations exist. The main frequency of oscillation was also approximately 0.02 Hz, as shown in Fig. 4-10(b).

Time series analysis was performed to clarify the causal relationship between predicted jet movement and speed. The results are shown in Fig. 4-11. As shown in the figure, the rise and fall of the jet preceded the rise and fall of its velocity. Soon after the jet started to rise, the flow speed in the top of the mold increased, and right after the jet began to lower, the flow speed in the top of the mold decreased. Based on this time series analysis result, we can conclude that the jet fluctuation is the main determinant of the velocity variations and stability in the upper area of the mold. In order to examine the influence of jet fluctuations on flow for the entire upper area of the mold, rather than only for the monitoring point, we calculated the velocity standard deviation contours for the 15 and 35° ports. The results are shown in Fig. 4-12. The vertical oscillations of the jet from the 15° port generally resulted in a higher value of the standard deviation of the velocity than those from the 35° port, both near the wall in the upper mold area and for the overall upper circulation zone.

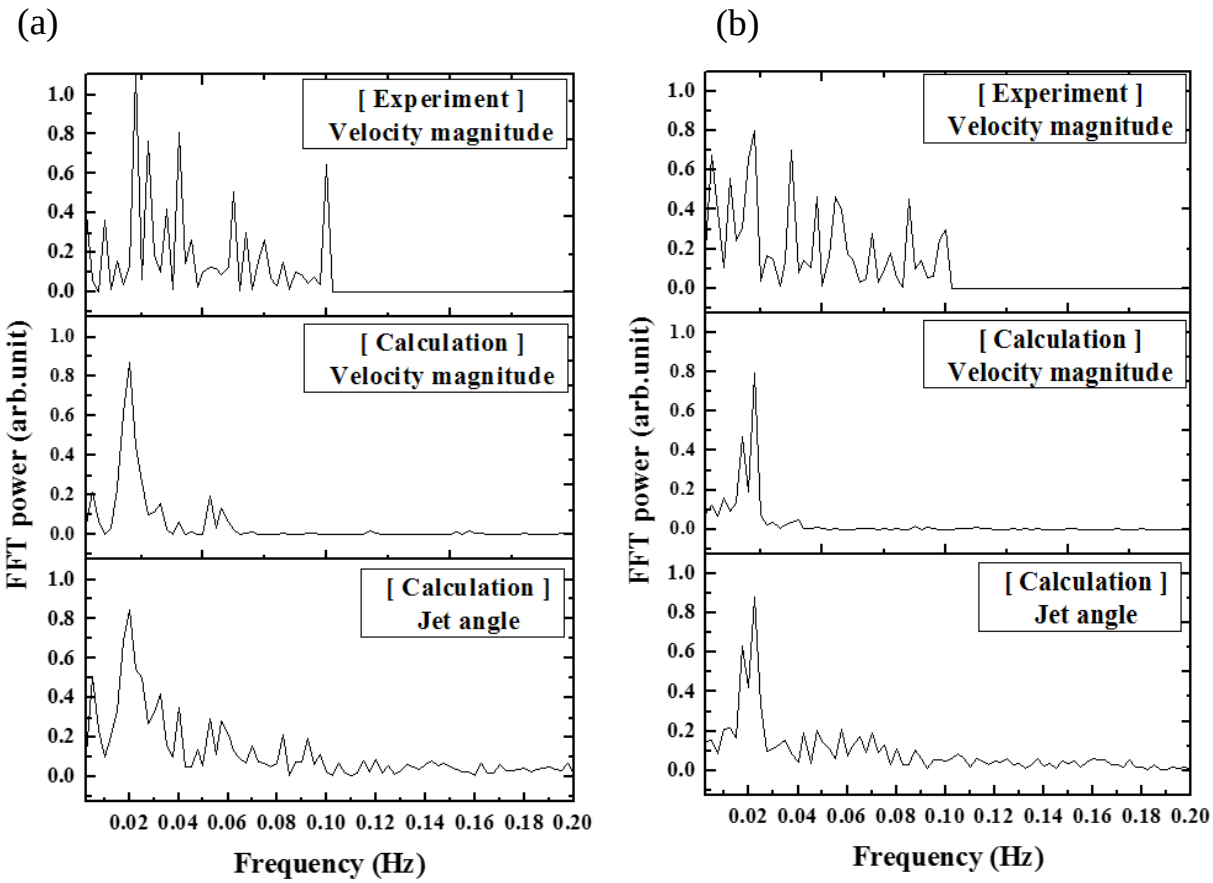


**Fig. 4-10.** Fast Fourier transform (FFT) of velocity fluctuations in Fig. 4 and jet angle fluctuation in Fig. 12 for port angles of (a) 15° and (b) 35°.

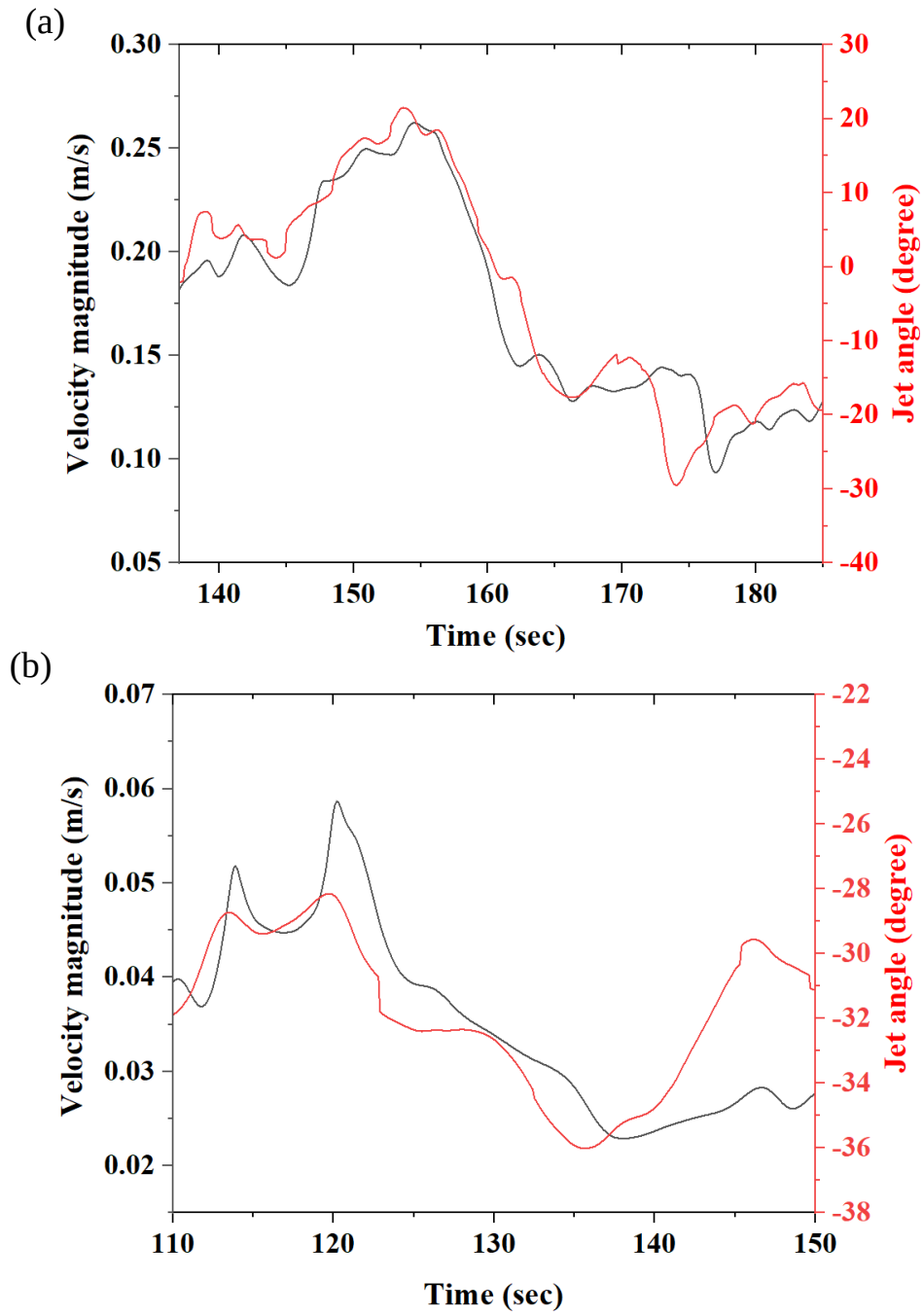


**Fig. 4-11.** Time series analysis of the predicted velocity magnitude and jet angle variation for port angles of (a) 15° and (b) 35°.

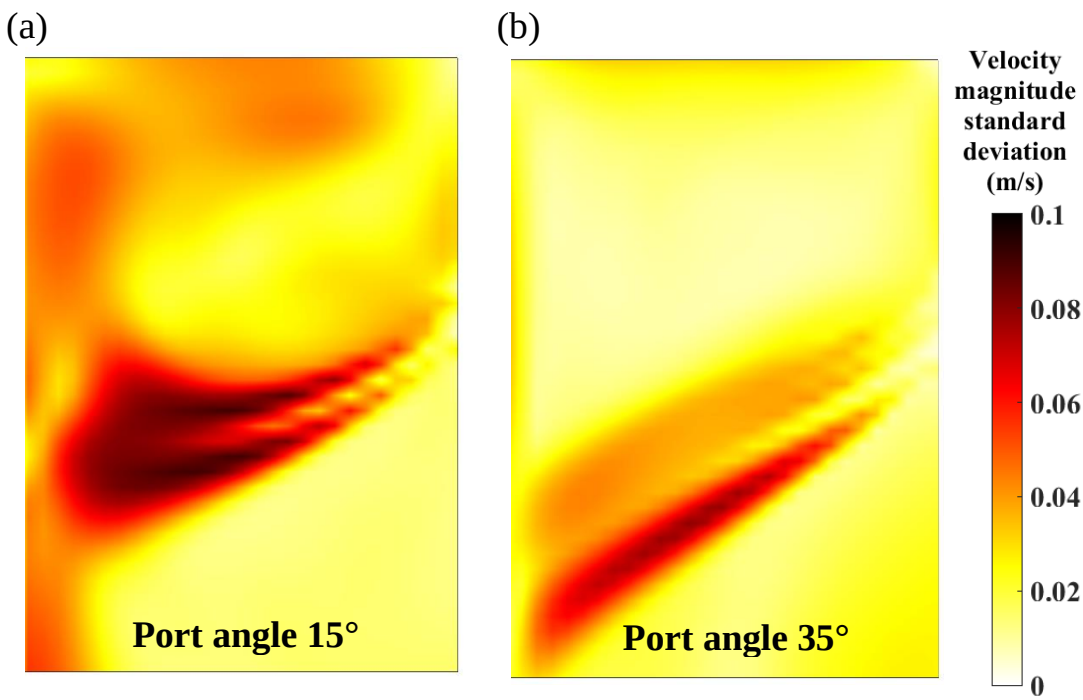


**Fig. 4-12.** Predicted velocity magnitude standard deviation contours of water in the upper region of the mold for flow without gas injection condition for port angles of (a) 15° and (b) 35°.

### 4.2.4 Effect of gas injection

As mentioned earlier, this unstable flow can induce significant slag entrapment and uneven shell growth. Considering the remarkable change in flow patterns, analyzing the jet angle behavior is very meaningful, and setting up a stable jet is essential for the conventional slab continuous-casting process.

The flow stability criterion may change depending on the process conditions or the geometric conditions of the mold and SEN. We performed PIV experiment and calculated fluid flow behavior when 2 L/min of nitrogen gas was injected (other conditions were unchanged). Figure 4-13 shows the magnitudes of the time averaged velocities and the values of standard deviation at the monitoring point from the PIV measurements of the experiment and from the simulation. For 0–15° port angles, the average and standard deviation of the velocity magnitude was significantly larger than that for the 25–35° angles. The most contrasting result with the previous case was the behavior of the 20° port angle. The time-averaged velocity magnitude for the 20° port angle without gas flow was 0.0861 m/s, but this was increased to 0.1842 m/s when gas was injected. The standard deviation of the velocity magnitude also increased from 0.0132 m/s to 0.0226 m/s. The range of the unstable region, in terms of the SEN port angle, was extended to 20° with the injection of nitrogen gas.

When gas is injected, there are remarkable changes in the flow pattern. In the unstable flow region, The jet oscillates vertically at the port angle in the unstable flow region with no gas flowing. However, when gas injected, jet toward wall is obtuse and an upward water jet is developed. The vertical fluctuations detected in no-gas conditions are no longer detected, and only the degree of upward bending change (fig. 4-14(a)). A velocity increase that corresponds to the rise of the jet is

found in both cases, but a comparison of flow patterns when the velocity magnitude ebbs shows that there is distinct difference. With no gas flows, the jet of water proceeds downwards after reaching the wall, leading to a relatively large velocity reduction. In contrast, when gas is injected, the jet remains at least an obtuse angle at its lowest point, so the amount of velocity reduction is small. Therefore, the degree of velocity magnitude deviation in the unstable flow region (0 – 15 degrees) decreases marginally as gas injected. In the stable flow region, injecting gas causes the previously straight jet to point downward less and form a slightly wavy shape due to the influence of buoyancy (Fig. 4-14(b)). However, the additional buoyancy is not enough to cause the water jet to focus on the upper circulation zone. Therefore, there are only minor differences with the velocity magnitude standard deviation produced without gas flow.

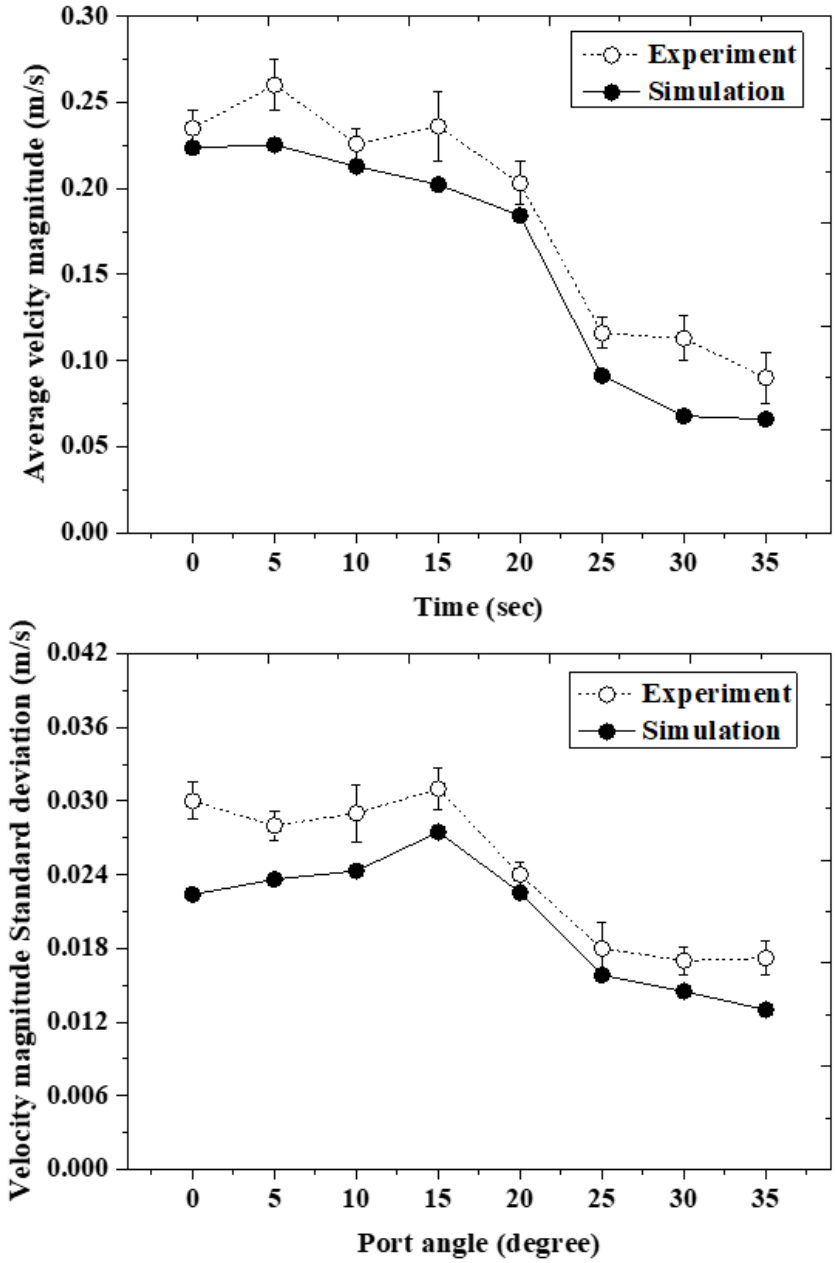


**Fig. 4-13.** (a) Average velocity magnitude at monitoring point with gas injection. (b) Velocity magnitude standard deviation at monitoring point with gas injection.

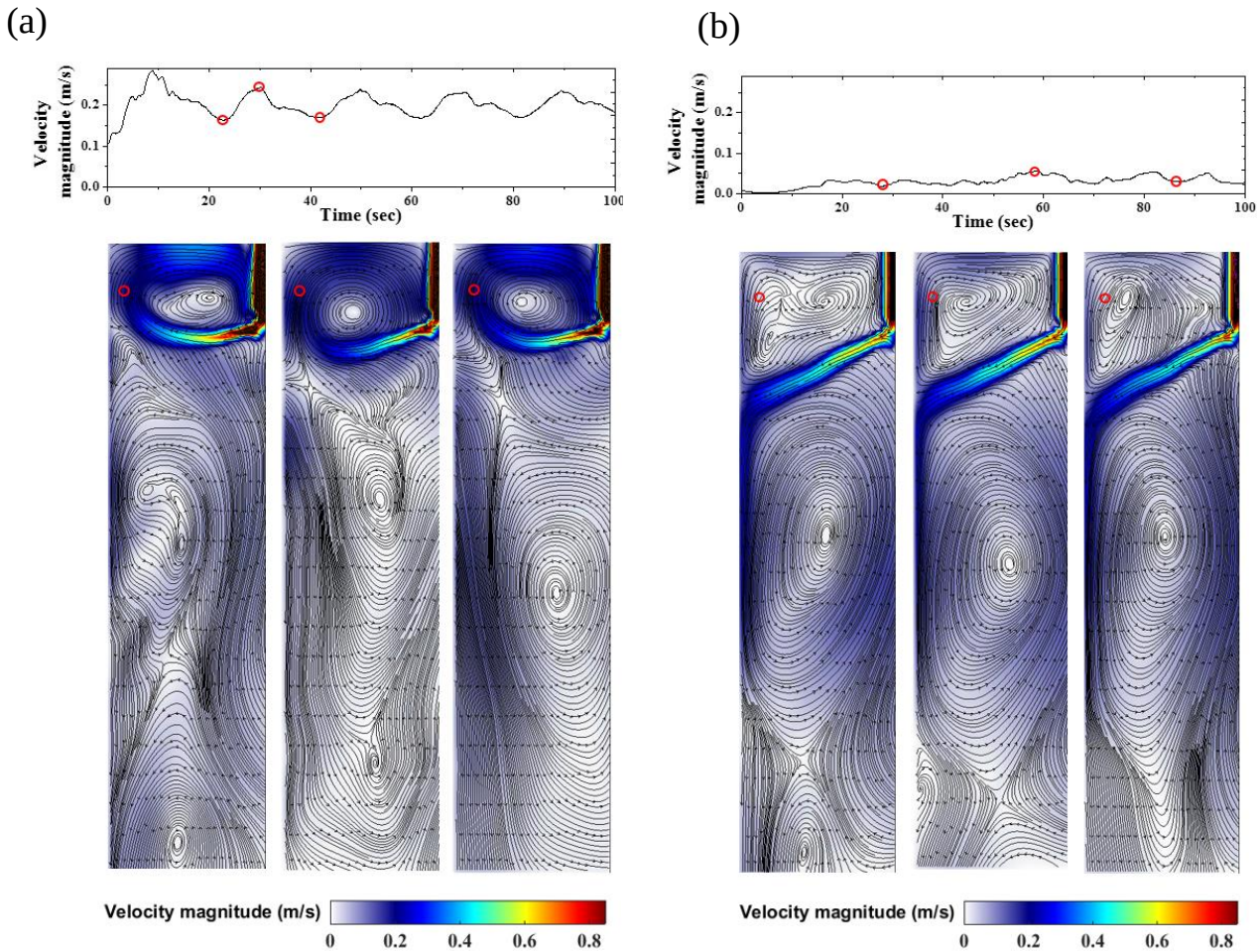


**Fig. 4-14.** Velocity magnitude versus time curves at the monitoring point with gas injection. Snapshot images of velocity distribution on the symmetry plane. The streamlines with small arrows on each figure represent the velocity components of the fluid. The red open circles of each contour indicate the monitoring point. (a) Port 15 (b) Port 35

To find the cause of the change in criteria, the jet angle variations at each port angle were analyzed. Predicted velocity profiles as a function of gas injection are plotted in Fig. 4-15. Comparing Fig. 4-7 and 4-15, the direction of the jet from the SEN moved upward as the gas was injected. The reason for this change is that the gases in the water provided a lifting force to the water because of the buoyancy force. The flow pattern for the 20° port angle with gas (Fig. 4-15(b)) was similar to that which was seen for the 15° port angle without gas (Fig. 4-7(a)). The time-averaged jet angle increased from −19.86 to −1.48° for the 20° port angle when the gas was injected. This is similar to the time-averaged jet angle −2.48° of the 15° port angle without gas injection. For a port angle of 25° or more, a periodic change in the jet direction was not observed, and since the jet was stably discharged downward, it had a low average speed (0.0661–0.0913 m/s) and a low speed standard deviation (0.0129–0.0158 m/s). It maintained a stable flow regardless of gas injection. This indicates an extension in the stability criteria in terms of the SEN port angle.

Fig. 4-16 shows predicted variations in the jet angle at the monitoring point over a period of 100 s with nitrogen gas injection. Large fluctuations were still observed for 0 to 15° port angles. In the case of the 20° port angle, unlike the previous case where only small fluctuations were present (Fig. 4-8), a periodic change in the direction of the main flow was observed. In the absence of gas injection, the jet oscillated from −31.43 to −11.31°, while it ranged from −17.00 to 23.40° with gas injection. The jet was raised by buoyancy to reach positive angles during oscillation, and thus, the main flow was directed into the upper circulation zone. On the other hand, at a port angle of 25°, as the gas was injected, the oscillation range shifted upward, with the minimum increasing from −34.39 to −26.99° and the maximum increasing from −21.30 to −6.02°; however, the jet angle at the maximum peak did

not exceed 0°, even if the jet rose during oscillations.

Whether the jet has a positive jet angle during oscillation is a major criterion for determining the stability of the flow. Since the injected gas can lift the jet upward by buoyancy, it can cause a previously downward directed jet to have a jet angle of more than 0°. Therefore, gas injection could cause instability in higher angle SEN ports.

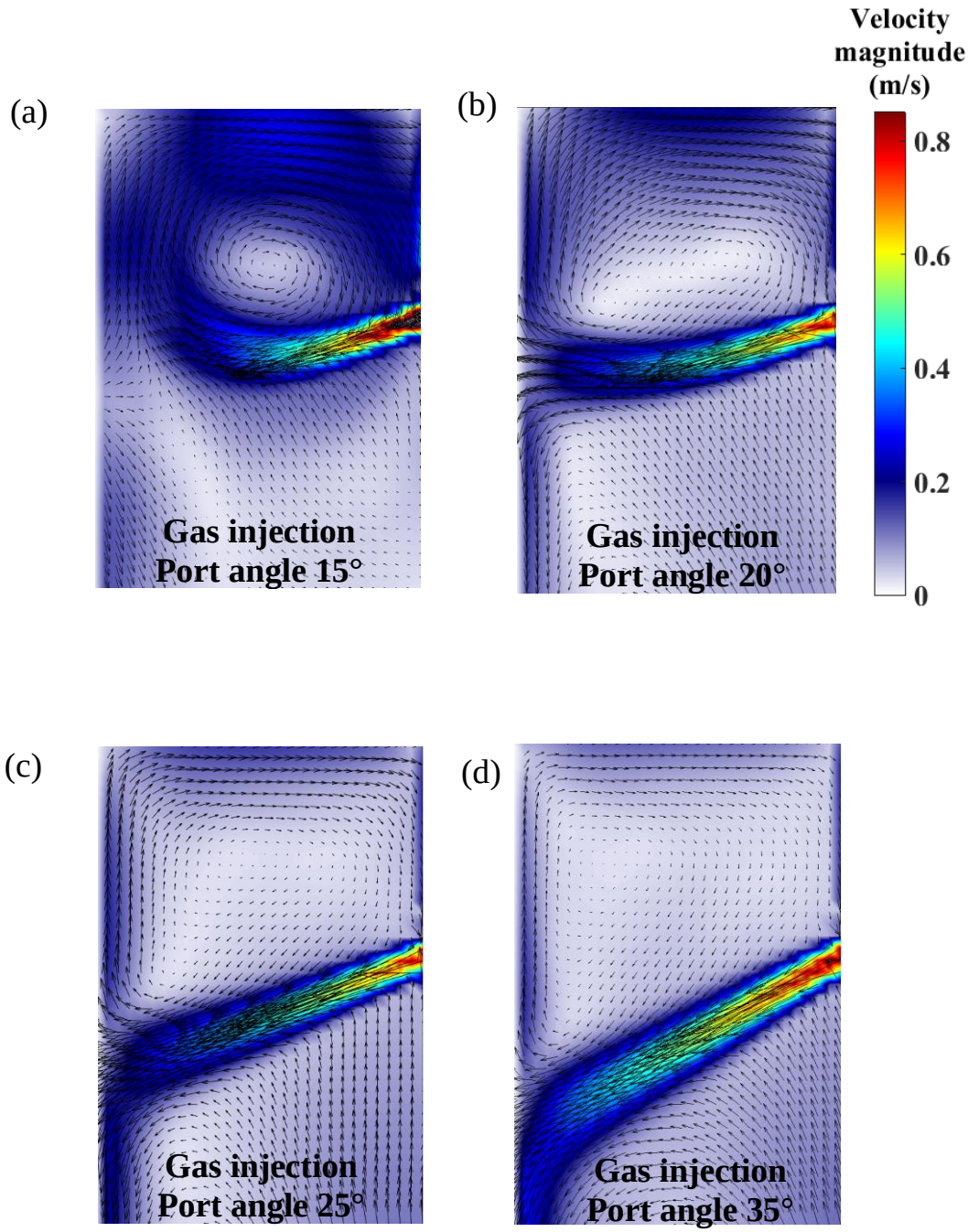


**Fig. 4-15.** Predicted time-averaged velocity plots in the upper region of the mold with gas injection. SEN port angles of (a) 15°, (b) 20°, (c) 25°, and (d) 35°.

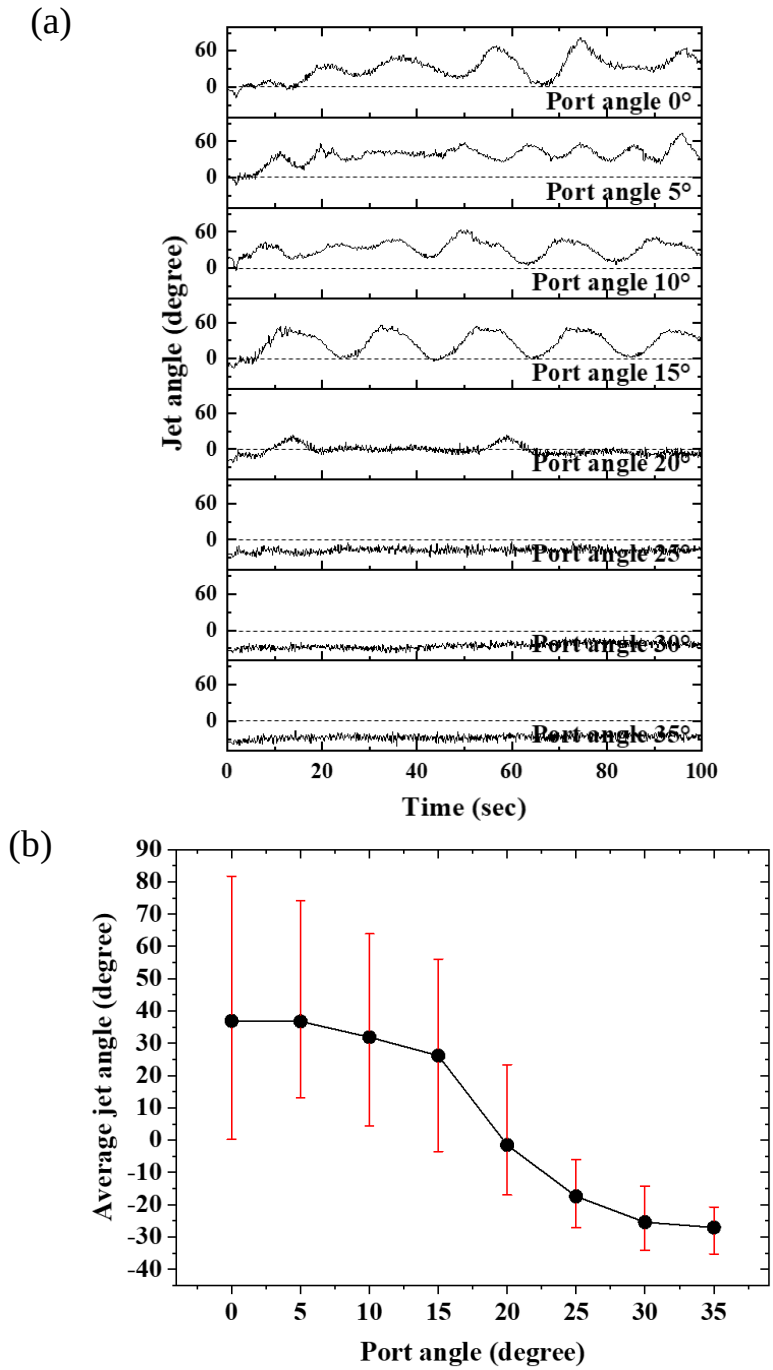


**Fig. 4-16.** Predicted jet angle variation with gas injection. (a) Jet angle variation versus time. Dashed line denotes a jet angle of 0°. (b) Time-averaged jet angle versus port angle. Red bar indicates the jet oscillation range with maximum and minimum values.

# Chapter 5. Conclusion

**I**n the chapter 3, we studied the behavior of oxygen refining in the ladle furnace, a secondary refining device in the steel production process, accompanying inclusion formation, and calcium aluminate production reaction by additional deoxidation. In the previous studies, flow inside the ladle, primary deoxidation reaction, and secondary deoxidation were conducted individually but these various phenomena were not observed at once. In order to solve the problems of the previous research, we developed a global model that can predict both fluid flow and chemical reaction.

To simulate the three phases of molten steel-Ar gas-slag, the quasi single phase model and drift flux model were used to reflect the interaction force between gas and melt, and a model for slag deformation was developed. The replacement experiment was conducted through a water model that is 1/8 of the actual ladle size, and the reliability of the model was verified through comparison with the area of the plume eye formed at the top of the ladle. Three phase flow result was used to simulate the reaction with oxygen dissolved in the melt and injected Al. The reaction equilibrium results were compared using the thermodynamic commercial code Factsage 6.4, and it was confirmed that very little error occurred.

Finally, Ca was added to the alumina produced in the primary deoxidation reaction step to simulate additional deoxidation. Using the quasi chemical thermodynamic model, the Gibbs energy of slag having different values according to the composition was obtained. A total of 21 calcium aluminate reactions were constructed, and an unreacted core model was applied to simulate the reaction kinetic. Equilibrium calculation results were also compared with Factsage 6.4 to verify

reliability. By simulating the process to reach equilibrium according to the Ca input composition, it was confirmed that when the slag phase is stable, the equilibrium is reached at a very high speed, and when the solid calcium aluminate is in the stable phase, the equilibrium is not reached during the conventional operating time of ladle furnace because of its slow reaction rate.

In the chapter 4, we used water model experiments and numerical simulations to investigate velocity variations in the upper circulation zone as a function of the SEN port angle of continuous casting mold. The experimental and simulated results showed good agreements. We proposed flow stability criteria for conventional slab molds as a function of the SEN port angle. Moreover, we quantitatively analyzed the jet movement, which is the cause of flow instability with large magnitude.

For SEN port angles in the 0–15° range, flow velocities in the upper circulation zone showed unstable behavior and strongly oscillated. On the other hand, when the port angle became higher than 20° the flow velocity decreased and magnitude of oscillation also sharply decreased. In other words the flow in this condition showed stable behavior. The experiments and numerical simulation showed that a main factor for determining the stability of upper circulating flow is the angle between the jet and the mold wall. When the jet angle remains downward direction during the oscillation, the flow behavior was kept stable. On the other hand, when the jet angles had upward direction even in a small portion of whole oscillations, the flow became unstable.

When 2 L/min of nitrogen gas is injected, the jet is lifted upward by buoyancy force of gas. Because of that force, jet angles of all port angles changed to more upper direction compared to those of no gas condition. Due to the gas effects,

the angle of jet injected by nozzle of 20° port angle partly had upward directions during oscillation. And jet angle of higher than 25° port angle remained downward direction during oscillation even in the gas injection. Because of that, the fluid flow behavior for 20° port angle showed strong fluctuations. So, gas injection increases the unstable region of port angle to 20°. The boundary of the stable region could be changed according to process conditions, but it is considered that fluid flow is stable if the jet angle maintains the downward direction. In the present study, we proposed not only flow stability criteria as a function of SEN port angle, but also an analytic method for determining instability criteria with the amount of instability which cause inclusion entrapment.

We expect that the developed model and methodology from this study could also be applied to determine additional process conditions and device designs for inclusion control.

# References

1. Kiessling, R. and Lange, N., Non-Metallic Inclusions in Steel, Parts I-IV, The Metals Soc., London, 1978.

2. Lindborg, U., A collision model for the growth and separation of deoxidation products. Trans. Metall. Soc. AIME, 1968. 242: p. 94.

3. ENDE, M.-A.V., Formation and Morphology of non-Metallic Inclusions in Aluminium Killed Steels, in Department of Materials Science. 2010, Katholieke Universiteit Leuven:Belgium. p. 261.

4. Jin, Y., Z. Liu, and R. Takata, Nucleation and Growth of Alumina Inclusion in Early Stages of Deoxidation: Numerical Modeling. ISIJ international, 2010. 50(3): p. 371-379.

5. Turkdogan, E.T., in Proc. Int. Symp. on Chemical Metallurgy of Iron and Steel, Iron and Steel Inst.,

London, 1973, p. 153; also Proc. 5th Int. Iron and Steel Cong., Washington D.C., 1986, p. 767.

6. Q. He, "Observation of vortex formation in the mould of a continuous slab caster", ISIJ Int., 33, 343 (1993).

7. Colpaert H. Metallography of steels: interpretation of structure and the effects of processing, updated and translated by Costa e Silva A. Materials Park, OH: ASM International; 2018.

8. Batista RP, Martins AA, Costa e Silva A. The effects of deoxidation practice on the quality of thin foil low-carbon steel. J Min Metall Sect B

Metall 2017;53(3B):357–63.

9. EEIMVR-UFF, Volta Redonda. The effects of non-metallic inclusions on properties relevant to the performance of steel in structural and mechanical applications. (2019). pp. 2408-2422

10. Murakami Y. Metal fatigue: effects of small defects and nonmetallic inclusions. Kidlington, England: Elsevier Science; 2002.

11. Bojko, M., & Čarnogurská, M. (2006). Modelling of stirring liquid bath by gaseous phase in real converter with bottom blowing.

12. Dutta S.K., Chokshi Y.B. (2020) Secondary Steelmaking. In: Basic Concepts of Iron and Steel Making. Springer, Singapore

13. N. Birks, G. H. Meier and F. S. Pettit, Introduction to theHigh Temperature Oxidation of Metals, Cambridge Univer-sity Press, Cambridge, 2nd edn, 2006.

14. K. Krishnapisharody, N.B. Ballal, P.K. Sinha, M.K. Sardar, and K.N. Jha: ISIJ Int., 1999, vol. 39, pp. 419–25.

15. R. Gonza´ lez-Bernal, G. Solorio-Diaz, A. Ramos-Banderas, E. Torres-Alonso, C.A. Herna´ ndez-Bocanegra, and R. Zenit: Steel Res. Int., 2017, vol. 89, art. no. 1700281.

16. J. Mandal, S. Patil, M. Madan, and D. Mazumdar: Metall. Mater. Trans. B, 2005, vol. 36B, pp. 479–87.

17. N. Mazumdar, A. Mahadevan, M. Madan, and D. Mazumdar: ISIJ Int., 2005, vol. 45, pp. 1940–42.

18. S.P. Patil, D. Satish, M. Peranandhanathan, and D. Mazumdar:

ISIJ Int., 2010, vol. 50, pp. 1117–24.

19. A.M. Amaro-Villeda, M.A. Ramirez-Argaez, and A.N. Conejo:

ISIJ Int., 2014, vol. 54, pp. 1–8.

20. H.Y. Tang, X.C. Guo, G.H. Wu, and Y. Wang: ISIJ Int., 2016,

vol. 56, pp. 2161–70.

21. Z.Q. Liu, L.M. Li, and B.K. Li: ISIJ Int., 2017, vol. 57, pp. 1971–

79.

22. A.S. Go´ mez, A.N. Conejo, and R. Zenit: J. Appl. Fluid Mech.,

2018, vol. 11, pp. 11–20.

23. A.H. Castillejos and J.K. Brimacombe: Metall. Trans. B, 1987, vol. 18B,

pp. 649−58.

24. A.H. Castillejos and J.K. Brimacombe: Metall. Trans. B, 1987, vol. 18B,

pp. 659−71.

25. S.T. Johansen, D.G.C. Robertson, K. Woje, and T.A. Engh: Metall.

Trans. B, 1988, vol. 19B, pp. 745−54.

26. S. Taniguchi, S. Kawaguchi, and A. Kikuchi: Appl. Math.Modell., 2002,

vol. 26, pp. 249−62.

27. P.E. Anagbo and J.K. Brimacombe: Metall. Trans. B, 1990,vol. 21B, pp.

637−48.

28. L.M. Li, Z.Q. Liu, B.K. Li, H. Matsuura, and F. Tsukihashi: ISIJ Int.,

2015, vol. 55, pp. 1337−46.

29. Y. Sahai and R.I.L. Guthrie: Metall. Trans. B, 1982, vol. 13B, pp. 125–27.

30. D. Mazumdar: Metall. Trans. B, 1989, vol. 20B, pp. 967–69.

31. Y. Sahai and R.I.L. Guthrie: Metall. Trans. B, 1982, vol. 13B, pp. 203–11.

32. D. Mazumdar and R.I.L. Guthrie: Metall. Trans. B, 1985, vol. 16B, pp. 83–90.

33. D. Mazumdar, R.I.L. Guthrie, and Y. Sahai: Appl. Math.Modell., 1993, vol. 17, pp. 255–62.

34. M.B. Goldschmit and A.H.C. Owen: Ironmak. Steelmak., 2001, vol. 28, pp. 337–41.

35. S. Ganguly and S. Chakraborty: ISIJ Int., 2004, vol. 44, pp. 537–46.

36. S. Ganguly and S. Chakraborty: Ironmak. Steelmak., 2008, vol. 35, pp. 524–30.

37. J. Aoki, L. Zhang, and B.G. Thomas: 3rd Int. Congr. on Science& Technology of Steelmaking, Warrendale, PA, 2005, pp. 319–32.

38. R. Singh, D. Mazumdar, and A.K. Ray: ISIJ Int., 2008, vol. 48, pp. 1033–35.

39. L.M. Li, B.K. Li, and Z.Q. Liu: ISIJ Int., 2017, vol. 57, pp. 1–10.

40. L.M. Li, Z.Q. Liu, M.X. Cao, and B.K. Li: JOM, 2015, vol. 67, pp. 1459–67.

41. L.T. Wang, Q.Y. Zhang, S.H. Peng, and Z.B. Li: ISIJ Int., 2005, vol. 45, pp. 331–37.

42. L.T. Wang, S.H. Peng, Q.Y. Zhang, and Z.B. Li: Steel Res. Int., 2006, vol. 77, pp. 25–31.

43. D.Q. Geng, H. Lei, and J.C. He: Int. J. Miner. Metall. Mater., 2010, vol. 17, pp. 709–14.

44. F.D. Maldonado-Parra, M.A. Ramirez-Arga´ ez, A.N. Conejo, and C. Gonza´ lez: ISIJ Int., 2011, vol. 51, pp. 1110–18.

45. A. Huang, H.Z. Gu, M.J. Zhang, N. Wang, T. Wang, and Y. Zou: Metall. Mater. Trans. B, 2013, vol. 44B, pp. 744–49.

46. Liu, Y., Ersson, M., Liu, H., Jönsson, P. G., & Gan, Y. (2019). A review of physical and numerical approaches for the study of gas stirring in ladle metallurgy. *Metallurgical and Materials Transactions B*, *50*(1), 555-577.

47. 96. W.T. Lou and M.Y. Zhu: Metall. Mater. Trans. B, 2013, vol. 44B, pp. 1251–63.

48. W.T. Lou and M.Y. Zhu: Metall. Mater. Trans. B, 2014, vol. 45B, pp. 1706–22.

49. W.T. Lou and M.Y. Zhu: ISIJ Int., 2015, vol. 55, pp. 961–69.

50. Y. Miki and S. Takeuchi, ISIJ Int. 43, 1548 (2003).

51. B. G. Thomas, Iron Steel Technol. 3, 7 (2006).

52. J. Knoepke, M. Hubbard, J. Kelly, R. Kittridge, J. Lucas, Steelmaking

Conference Proceedings, ISS, Warrendale, PA, 381 (1994).

53. D. Gupta and A. K. Lahiri, Metall. Mater. Trans. B 27, 757 (1996).

54. A. Ramos-Banderas, R. Sánchez-Pérez, L. Demedices-García, J. Palafox-Ramos, M. Díaz-Cruz, R. D. Morales, Metall. Mater. Trans. B 35, 449 (2004).

55. X. Huang, B. G. Thomas, F. M. Najjar, Metall. Trans. B 23, 339 (1992).

56. L. Zhang, S. Yang, K. Cai, J. Li, X. Wan, B.G. Thomas, Metall. Mater. Trans. B 38, 63 (2007).

57. N. Bessho, R. Yoda, H. Yamasaki, T. Fujii, T. Nozaki, S. Takatori, ISIJ Int. 31, 40 (1991).

58. S.-M. Cho, S.-H. Kim, and B. G. Thomas, ISIJ Int. 54, 845 (2014).

59. B. G. Thomas, L. J. Mika, F. M. Najjar, Metall. Trans. B 21, 387 (1990).

60. J. W. Evans, D. Xu, W. K. Jones, Met. Mater. 4, 1111 (1998).

61. D. F. Wu and S. S. Cheng, Acta Metall. Sin-Engl. 21, 341 (2008).

62. A. Sen, B. Prasad, J. K. Sahu, J. N. Tiwari, IOP Conf. Ser.: Mater. Sci. Eng. 75, 012006 (2015).

63. M. Alam, M. Manzoor, M. I. H. Siddiqui, Int. Rob. Auto. J. 4, 14 (2018).

64. W. V. Gabriel, J. J. M. Peixoto, C. A. Silva, C. A. Silva, I. A. Silva, V. Seshadri, J. Mater. Process. Technol. 245, 232 (2016).

65. Q. Yuan, B. G. Thomas, S. P. Vanka, Metall. Mater. Trans. B 35, 685 (2004).

66. R. Singh, B. G. Thomas, S. P. Vanka, Metall. Mater. Trans. B 45, 1098 (2014).

67. B. K. Li, Z. Q. Liu, F. S. Qi, F. Wang, G. D. Xu, Acta Metall. Sin. 48, 23 (2012).

68. R. Chaudhary, B. G. Thomas, S. P. Vanka. Metall. Mater. Trans. B 43, 532 (2012).

69. Z. Liu, B. Li, M. Jiang, Metall. Mater. Trans. B 45, 675 (2014).

70. S. M. Cho, B. G. Thomas, S. H. Kim, Metall. Mater. Trans. B 47, 3080 (2016).

71. Z. Q. Liu, B. K. Li, M. F. Jiang, L. Zhang, G. D. Xu, Acta Metall. Sin. 49, 513 (2013).

72. Thielicke, W., & Stamhuis, E, Journal of Open Research Software, 2 (2014).

73. Patankar, S. (2018). *Numerical heat transfer and fluid flow*. Taylor & Francis.

74. https://www.comsol.com/blogs/fem-vs-fvm/

75. *CFD-ACE+ v.2011.0 Modules Manual*.

76. ANSYS Inc. ANSYS Fluent Version 15.0 User's Guide (2014).

77. S. M. Cho, B. G. Thomas and S.-H. Kim, ISIJ Int. 58, 1443 (2018).

78. Zhu MY, Cai ZZ, Yu HQ, J. Iron. Steel Res. Int. 20, 6 (2013).

79. D. Kang and R. K. Strand, Energ. Buildings, 62, 196 (2013).

80. M. Iguchi, H. Kawabata, K. Nakajima and Z.-I. Morita, *Metall. Trans. B* 26, 67 (1995).

81. V. G. Levich and D. B. Spalding, Physicochemical Hydrodynamics, P.451, Prentice-Hall Englewood Cliffs, NJ(1962).

82. G. B. Wallis, One-dimensional Two-phase Flow, P.89, McGraw-Hill NewYork(1969).

83. C. Wagner, S. Mellgren and J. H. Westbrook, Thermodynamics of Alloys, Addison-Wesley Press Cambridge, MA(1952).

84. L. Zhang and B. G. Thomas, ISIJ int. 43, 271 (2003).

85. I.-H. Jung, S. A. Decterov and A. D. Pelton, Metall. Trans. B 35, 493 (2004).

86. M. W. Chase, JANAF Thermochemical Tables, by Chase, MW Washington, DC:American Chemical Society; New York: American Institute of Physics for the National Bureau of Standards, c1986.. United States. National Bureau of Standards. 1 (1986).

87. L. V. Gurvich and I. Veyts, Thermodynamic Properties of Individual Substances:Elements and Compounds, CRC Press(1990).

88. I. Barin, F. Sauert, E. Schultze-Rhonhof and W. S. Sheng,Thermochemical Data of Pure Substances, VCH Weinheim(1993).

89. H. E. Barner and R. V. Scheuerman, Handbook of Thermochemical Data for Compounds and Aqueous Species, Wiley New York(1978).

90. www.Factsage.com : Database

91. C. W. Bale and A. Pelton, Metall. Trans. B 14, 77 (1983).

92. R. G. Berman and T. H. Brown, Contributions to Mineralogy and Petrology 89,168 (1985).

93. P. Wu and A. D. Pelton, Journal of Alloys and Compounds 179, 259 (1992).

94. Pelton, Arthur D., and Milton Blander. "Thermodynamic analysis of ordered liquid solutions by a modified quasichemical approach—application to silicate slags." Metallurgical Transactions B 17.4 (1986): 805-815.

95. Hallstedl, Bengt. "Assessment of the CaO-Al2O3 System." Journal of the American ceramic society 73.1 (1990): 15-23.

96. Eriksson, Gunnar, and Arthur D. Pelton. "Critical evaluation and optimization of the thermodynamic properties and phase diagrams of the CaO-Al2O3, Al2O3-SiO2, and CaO-Al2O3-SiO2 systems." Metallurgical Transactions B 24.5 (1993): 807-816.

97. Pelton, A. D., et al. "The modified quasichemical model I—binary solutions." Metallurgical and Materials Transactions B 31.4 (2000): 651-659

98. Levenspiel, Octave. "Chemical reaction engineering." Industrial & engineering chemistry research 38.11 (1999): 4140-4143.

99. Ito, Yo-ichi, et al. "Kinetics of shape control of alumina inclusions with calcium treatment in line pipe steel for sour service." ISIJ international 36.Suppl (1996): S148-S150.

100. Lind, Minna. "Mechanism and kinetics of transformation of alumina inclusions in steel by calcium treatment." (2006).

101. Lind, Minna, and Lauri Holappa. "Transformation of alumina inclusions by calcium treatment." Metallurgical and materials transactions B 41.2 (2010): 359-366.

102. ANSYS Inc. ANSYS Fluent Version 15.0 User's Guide (2014).

103. H. Versteeg, W. Malalasekera, An Introduction to Computational Fluid Dynamics: The Finite Volume Method, Prentice Hall (2007).

104. J. Y. Lee, Y. T. Kim, K. W. Yi, Met. Mater. Int. 21, 295 (2015).

105. S. M. Cho, B. G. Thomas and S.-H. Kim, ISIJ Int. 58, 1443 (2018).

106. Zhu MY, Cai ZZ, Yu HQ, J. Iron. Steel Res. Int. 20, 6 (2013).

# 초 록

래들에서의 정련은 철강생산 단계에서 형성되는 내인성 개재물을 제어할 수 있는 마지막 단계이므로 탈산 과정에서 생성되는 inclusion을 모사하는 것은 매우 중요하다. 특히, 부상분리의 용이성을 위해 추가적으로 투입되는 칼슘은 많은 동소체가 존재하고 관여하는 반응의 개수가 매우 많아 그 반응을 구현하기 매우 복잡하다. 이를 모사하기 위해서는 앞단의 용강–아르곤 가스–슬래그로 이루어진 다상 유동을 구현해야 하며 알루미늄 투입으로 이루어지는 일차탈산에 의한 알루미나 개재물 모사가 선행되어야 한다.

용강–아르곤 가스–슬래그로 이루어진 세가지 상의 유체유동을 모사하기 위해 quasi single phase model과 drift flux모델을 이용해 가스와 용강간의 힘을 계산하고 슬래그 변형에 대한 모델을 개발하여 유체해석 모델과 결합하였다. 실제 ladle size의 1/8인 수모델을 통해 대체실험을 진행하였고 래들 상단부에서 형성되는 plume eye의 면적과 비교를 통해 모델에 대한 신뢰성을 검증하였다. 유동해석 결과를 이용해 알루미늄과 칼슘과 같은 탈산제 투입에 따른 화학종 이송방정식을 풀고 1차 탈산반응, 2차 탈산반응을 모사할 수 있는 화학반응 모델을 개발하였다. 열역학과 속도론을 접목한 계산을 통해 매시간 마다 래들 내부의 모든 위치에서 일어나는 화학반응의 결과를 추적할 수 있었고 평형으로 도달하기 까지의 공정을 예측하였다. 칼슘의 투입량이 적어 고상의 칼슘알루미네이트가 평형상이 되는 경우, 평형에 도달하기까지 매우 오랜시간이 걸려 기존한 래들의 조업시간 동안 평형에 도달하지 못함을 확인하였다.

몰드 내부에서의 유체유동은 슬래그나 몰드플럭스의 혼입을 야기할 수 있고 이는 외인성 개재물이 발생하는 주요 원인이 될 수 있기 때문에 이를 제어하는 것은 매우 중요하다. 연속 주조 몰드 내부에서의 유체 흐름은 침지 노즐

의 각도와 매우 밀접한 관련이 있다. 유체 유동은 특정 노즐의 각도보다 작으면 불안정하여 포트 출구 근처뿐만 아니라 몰드 전반부에서 유체 제트의 진동에 의한 반복적인 와류 형성이 유발된다. 하지만, 특정 노즐의 각도보다 커지게 되면 유체유동이 매우 안정한 양상을 보인다. 전산모사와 수모델 실험을 통해 이러한 현상에 대한 연구를 진행하였다. 이때, 침지 노즐의 각도를 달리하여 유체 유동을 분석하였고 침지 노즐과 유속의 변화에 대한 보다 정량적인 관계를 파악하였다. 침지 노즐이 0–15° 인 구간에서는, 몰드 상단부의 영역에서 유속이 매우 불안정하게 진동함을 확인하였다. 20° 이상의 침지 노즐에서는 형성되는 유속값이 매우 작고 진동 또한 매우 작아 안정한 양상을 보였다. 가스가 투입되면 기존에 안정한 영역이었던 0–15° 구간이 0–20°도로 증가함을 확인하였다. 침지 노즐에 따라 형성되는 제트 각도와 표면 유동간의 관계를 정량적으로 분석하고 안정한 몰드 상단부에 안정한 유동이 형성될 수 있는 보다 일반적인 조건을 제시하였다.

본 연구에서는 개재물과 깊은 관련이 있는 래들에서 일어나는 복잡한 화학반응과 연속 주조 몰드 내부에서의 유동패턴에 대해 보다 심도깊은 이해를 제공한다.

주요단어 : 래들, 연속 주조 몰드, 열역학, 속도론, 개재물, 유체 유동, 전산 모사

학 번: 2014-21456